# Investigations of a novel small animal PET scanner with depth of interaction using GATE and a newly developed data rebinning application

Lakshal Perera
University of Wollongong

# INVESTIGATIONS OF A NOVEL SMALL ANIMAL PET SCANNER WITH DEPTH OF INTERACTION USING GATE AND A NEWLY DEVELOPED DATA REBINNING APPLICATION

by

Lakshal Perera BE, BSc, MSc

A Thesis submitted in fulfilment of the
requirements for the Doctor of Philosophy Degree
at the Centre for Medical Radiation Physics, School of Engineering Physics,
University of Wollongong

2009

Thesis supervisors:
Dr Michael Lerch and Prof Anatoly Rosenfeld

CERTIFICATION

I, Lakshal Perera BE, BSc, MSc, declare that this thesis, submitted in fulfilment of the requirements for the award of Doctor of Philosophy, in the Centre for Medical Radiation Physics, School of Engineering Physics, University of Wollongong, is wholly my own work unless otherwise referenced or acknowledged. The document has not been submitted for qualifications at any other academic institution.

---

Lakshal Perera BE, BSc, MSc

January 15, 2009

## ACKNOWLEDGEMENTS

A tertiary education and PhD are not tasks one completes without a multitude of support from all areas of life. My support has come from numerous sources and I am eternally thankful to these people for helping me get to this point.

Thanks to my main supervisor Dr Michael Lerch for not only his guidance, common sense and time while also managing a thousand other things, but friendship as well. I extend thanks also to my co-supervisor Prof Anatoly Rosenfeld, for providing financial support for this study as well as faciliting my attendance at a number of conferences, one in particular at a time of great difficulty in the project, enabling progress. I also thank Dr George Takacs for his continuing interest in my project as well as the numerous fruitful discussions on education, environmental policy and most recently, guitar technique.

I also thank all of my fellow students at the Centre for Medical Radiation Physics and the School of Engineering Physics: Ame, Big-O, Deanħo, Elpho, Field Marshall Kelly, Heids, Iwano, K-Dizzle, Mole, Sandcastle, Scuba, Sum and T-Bone, for making these three and a half years feel like some of the most enjoyable years of my life. The sense of fraternity and team dynamic that the students at the CMRP have is something all other academic centres should aspire to.

I would like to thank the University of Wollongong and the Australian Government for their financial support in the form of an Australian Postgraduate Award.

To Wencke Lehnert, my gratitude for assisting with experimental verification at The Brain and Mind Institute at the University of Sydney.

Thanks to Dean Cutajar and Brad Oborn for their hard work on the CMRP High Performance Computing Cluster; without your contribution to making this facility a reality, I'd still be running simulations right now.

Thanks to Andy, Lauren and Vaughan for their daily dose of caffeine and witty banter which fuelled my work each morning.

I offer thanks to all of my friends outside of the CMRP, for their repeated jibes for me to "get a real job"; you've actually convinced me that I probably should! Further thanks to Becky, Austin, Marisa, Chris M and Virginia for their continued interest and encouragement for me to get my thesis completed.

My parents Sarath and Swarna, came to Australia in 1977 with $250 in their pockets wanting to be able to provide the best education for their children. I hope that this is what they had in mind for me and that I've made them proud . I am forever grateful for their support and love during my life and my studies. Further thanks to my sister Ru for pretending to be interested in my project whenever I discussed it around her! Extended thanks to my dad for reading, re-reading and re-re-reading this thesis as well as offering intelligent advice on content, structure and grammar. Further gratitude to Vivienne Higginbotham for doing a great job with picking up all of those little spelling and grammatical things us badley speeling scintists missed!

I finally thank my ever-patient and loving girlfriend Sophie for sticking by me, years after I promised I was going to be finished.

## ABSTRACT

Current Positron Emission Tomography (PET) detectors suffer degradation in the spatial resolution at the edges of the field of view. This occurs as a result of the lack of depth of interaction (DOI) information which causes uncertainty in deducing the Lines of Response (LOR) between coincident events. The Centre for Medical Radiation Physics at the University of Wollongong has developed a novel detector module for use in small animal PET which will provide depth of interaction information while retaining the sensitivity of current scanners. This will result in superior imaging together with the ability to locate smaller lesions. This work focuses on preliminary investigations of the suitability of replacing the bulky scintillator crystals and photomultiplier tubes of traditional PET detector modules with compact LYSO scintillator crystals individually coupled to Si photodetectors.

Preliminary simulations focused on optimising the detector module were performed using the GATE Monte Carlo package. Data from the simulations was processed using a newly developed sinogram binning application. This application is flexible and able to adapt to numerous detector geometries based on user input. Depth of interaction information is automatically considered when binning the sinogram. Comparison of data from Monte Carlo studies processed with the sinogram binning application and experiments using a microPET Small Animal PET scanner are presented to illustrate the suitability of the sinogram binning application for future Monte Carlo PET data processing.

The spatial resolution results which are provided indicate this detector module is capable of providing superior performance to monolithic scintillator crystal detector modules. Furthermore, notable advances can be made towards a significant reduction of the radial elongation artefact at the edges of field of view. Other parameters

which are important to the process of quantifying the performance of a small animal PET scanner are also presented including optimisation of energy windows, the crystal size and detector configuration.

## TABLE OF CONTENTS

## LIST OF FIGURES

# CHAPTER 1

# INTRODUCTION

## 1.1 Statement of the Problem

Recent advances in medical imaging technologies have provided the platform for increasingly successful diagnosis and treatment of cancer and cancer related illnesses. Modalities such as Computed Tomography (CT), Magnetic Resonance Imaging (MRI) and Ultrasound provide anatomical information, while newer technology such as Positron Emission Tomography (PET) gives functional information. The latest revolution in medical imaging involves the registration of different modalities such as CT/PET and MRI/PET to provide both anatomical and functional information. CT and MRI technologies have undergone intensive development over the years and have reached a point where their performance is extremely optimised. PET, on the other hand, is a relatively recent innovation and still faces a number of significant limitations.

While PET is an extremely useful medical imaging tool, its performance and efficacy are limited significantly by poor spatial resolution. The resolution at the centre of the field of view (FOV) is significantly poor compared to the anatomical imaging modalities, and further degrades towards the edges of FOV due to a phenomenon known as the radial elongation artefact. The spatial resolution is highly dependent on the scanner and the individual parameters of the acquisition however PET shows a resolution within the range of 3-8 mm while CT offers a significantly more impressive resolution of 1-2 mm. In order to retain high sensitivity, the crystals used in PET studies must be of a suitable length. Although this is the case, the radial elongation artefact arises as a result of the detector's inability to measure the depth

of interaction (DOI) within that crystal element. According to traditional scanner design, a significant compromise is required between detector sensitivity and spatial resolution at the edge of FOV. Current PET scanner designs offer DOI information utilising varied techniques and provides improved performance compared to older technologies and processes.

## 1.2 Research Objectives and Methodologies

The aim of the work presented in this thesis is to develop a method of simulating and processing the data from a new PET detector module for use in small animal PET developed by the Centre for Medical Radiation Physics (CMRP). This detector module is capable of providing extended depth of interaction information while retaining the sensitivity of traditional small animal scanners. Preliminary investigations into the spatial resolution performance of the proposed detector module, as well as determining the optimal geometric properties of the module are undertaken.

The benefit provided by DOI information is clearly known from previous studies, however all have relied on the use of bulky photomultiplier tubes (PMTs), whereas the proposed module utilises miniaturised silicon photodetectors. In order to quantify the improvement in the performance gained by this module, Monte Carlo simulations were carried out.

The bulk of the content in this thesis focuses on the Monte Carlo data processing algorithm and the application which was developed specifically for this study. The data processing application generates a sinogram from the list mode output data of the Monte Carlo simulation and is highly flexible, able to adapt to the geometry of the scanner using input from the user. The application can incorporate DOI information with the ability of "oversampling" the data, enabling the extraction of as much information as possible from the Monte Carlo study.

### 1.3 Outline of the Thesis

Chapter 2 contains a thorough literature review of PET, as well as PET scanners, their limitations and current technology which enables DOI information to be obtained from PET detectors.

The novel detector module is introduced in Chapter 3, along with the Monte Carlo simulation platform GATE. A detailed description of GATE and its operation, in the context of this study, is presented.

Chapter 4 focuses on the novel data processing algorithm, known as the sinogram binning application, developed to process the Monte Carlo data. The methodology of the sinogram binning application is discussed in detail including all of the features available within it.

Experimental verification of the sinogram binning application using a MicroPET Focus 220 Small Animal PET scanner is presented in Chapter 5. This will validate the application's use in Chapter 6 which contains the analysis of Monte Carlo simulation data processed by the sinogram binning application. This chapter contains a range of studies focusing on measuring the characteristics of the novel detector module including spatial resolution, sensitivity and susceptibility to scatter. The effect of obtaining DOI information is also considered in detail.

Chapter 7 provides recommendations for future developments within this study and conclusions on the work presented in this thesis.

# CHAPTER 2

# PET BACKGROUND

## 2.1 Introduction to Medical Imaging

Medical imaging is an important tool in clinical medical science with applications in detection and treatment of many conditions. It enables observation of internal structure and in some cases, function in order to reveal, diagnose or investigate diseases. In the specific area of cancer treatment, medical imaging is one of the major diagnostic tools utilised in the detection of cancer, with multiple modalities available for different applications.

Most medical imaging techniques rely on the absorption of a signal (radiation or sound) within the subject, with detection of the remaining signal providing information about the internal structure of that subject. The manner in which the signal interacts with structures often depends on the composition of that structure, hence the output signal is affected by the medium being imaged. For example, in traditional projection x-ray radiography, bones absorb a greater proportion of the x-rays than tissue and muscle, therefore the signal recording device (analogue or digital) records less transmitted signal of relevance to the areas with absorption.

This chapter provides an outline of currently existing medical imaging modalities with specific focus on Positron Emission Tomography (PET) and its limitations. The depth of interaction error in PET is discussed as are current techniques of reducing this error and the detector modules used. This chapter also presents background information pertinent to the undertaking of Monte Carlo simulations for the characterisation and optimisation of the proposed detector module within this study.

## 2.2 Interaction of Photons in Matter

The interaction between photons and matter are fundamental to medical imaging techniques. The interactions depend significantly on the energy of the photon and the medium through which they propagate. There are three main processes by which radiation interacts with atoms.

### 2.2.1 Photoelectric Effect

The photoelectric effect is the dominant interaction process at low energies. If an incident photon strikes an electron with an energy greater than the work function, the electron can be ejected. The energy of the electron is related to the energy of the incident photon and the work function of the material that electron was bound to. As an electron from a higher energy level drops down into the hole left by the liberated electron, a photon is released with an energy equal to the difference between the electron's two states. The photoelectric effect is the dominant process in the "photopeak" observed in the energy spectrum of dose deposition in the scintillator crystal of a PET study.

### 2.2.2 The Compton Effect

The Compton Effect gives rise to Compton scattering (aslo known as incoherent scattering), a process whereby photons partially transfer energy to electrons in a material. As the photon transfers energy to the electron (making the electron "recoil"), a new photon of lower energy is emitted with a longer wavelength. Equation 2.1 illustrates the new wavelength ($\lambda'$) with respect to the original wavelength ($\lambda$), the angle by which the photon has been scattered ($\theta$), $m_e$ representing the mass of the electron, $h$ being the Planck Constant and $c$ the speed of light.

$$\lambda' - \lambda = \frac{h}{m_e c}(1 - \cos\theta) \tag{2.1}$$

A Compton scattering conserves momentum and, if the resulting photon has sufficient energy, it can continue Compton scattering repeatedly until its energy is sufficiently low to have a photoelectric absorption. Compton scatter is detrimental to imaging studies, especially PET as scattered photons create "noise" within the final reconstructed image.

### 2.2.3 Pair Production

Pair production is the creation of an electron and positron pair from a high energy photon. The high energy photon interacts with the atomic nucleus with the created electron and positron conserving the momentum and energy of the incident photon. This process is prevalent only when the incident photon has an energy greater than 1022 keV, the rest mass of the electron and positron it creates. If the photon has energy greater than 1022 keV, the electron-positron pair is given kinetic energy as well.

## 2.3 Anatomical Imaging: x-ray, CT, MRI, Ultrasound

Anatomical imaging provides physical and structural information about the subject being imaged. Different types of structures can be differentiated, however the ability to separate histologically similar organs depends significantly on the modality being used. Common anatomical imaging techniques are described in the following sections.

### 2.3.1 X-ray Radiography

X-ray radiography (also known as x-rays) is the oldest and most commonly used medical imaging technique. Low energy x-rays are emitted and allowed to propagate through the patient with detectors (analogue or digital) measuring the radiation on the other side of the patient with 2D image being produced. Dense structures such as bones absorb the x-rays and hence the detector does not record

a signal within the "shadow" caused by the structure. X-ray radiography is utilised heavily when the structures of interest have electron densities much higher than their surroundings such as the case of imaging bones. X-ray radiography does not provide any functional information.

### 2.3.2 Computed Tomography

Computed Tomography (CT) utilises x-rays as well but numerous x-ray images are taken from multiple projection angles. The multiple projections can be combined to provide an accurate 2D map of a thin slice of the subject being imaged. Multiple slices can be acquired by moving the patient through the field of view, enabling a 3D image to be established. CT uses x-rays of different energies compared to traditional radiographic imaging therefore imaging of soft tissue is possible. However, a notable difference between the electron density of the tissues is still required to produce a useful image. As with x-ray radiography, CT does not provide significant functional information, mostly the gross tissue and bone structure within the body. However, functional information such as blood flow and perfusion can be gained in instances using contrast agents.

### 2.3.3 Magnetic Resonance Imaging

When the electron densities of tissues are similar and differentiation is required, another technique known as Magnetic Resonance Imaging is utilised. A Magnetic Resonance Imaging (MRI) scanner utilises powerful magnets to polarise hydrogen nuclei within the subject. Hydrogen nuclei are abundant in all tissue due to the water content within the body. As the polarised hydrogen nuclei return to their unexcited states, they emit characteristic radio wavelength signals which can be detected by the MRI scanner. The detected signal is reconstructed to produce 2D slices of the imaged subject and, as with CT, the patient is placed within the scanner to acquire a 3D image. Due to the large variations in the water composition

of tissue types, MRI is an extremely useful tool in the imaging of soft tissue. Another advantage of MRI is that it does not utilise any form of ionising radiation, a significant advantage when attempting to minimise the risk of cancer formation. MRI provides some functional information in the form of differentiating areas of high blood perfusion. A more commonly used method becoming popular in meural imaging is known as functional MRI (fMRI). It is a highly specialised method of measuring the haemodynamic repsonse as a result of neural activity in the brain or spinal cord.

### 2.3.4 Ultrasound

Ultrasound, as the name suggests, utilises very high frequency sound waves and their reflective properties to create images. The ultrasound head is placed on the subject to be imaged and the reflected waves are detected by the same head, providing a 2D map of the reflection/absorption along the path the waves propagate. One of the significant advantages of ultrasound is that it provides real time information, whereas other techniques such as CT and MRI require image acquisition and reconstruction time. At present, ultrasound only provides functional information in the form of the Liver Functional Test.

## 2.4 Functional Imaging: gamma camera, Single Photon Emission Computed Tomography (SPECT) and Positron Emission Tomography (PET)

The processes described in Section 2.3 refer to anatomical imaging which has limited ability to identify different types of tissue. This becomes increasingly problematic when the focus of the imaging is to locate millimetre scale cancers or metastases as the scanner simply cannot differentiate between healthy tissue and small cancerous tissue.

Gamma camera imaging, Single Photon Emission Computed Tomography (SPECT)

and Positron Emission Tomography (PET) are techniques which utilise the biological differences between cancerous cells and healthy cells, displaying function as opposed to structure. A detailed explanation of PET is provided in Section 2.5.

### 2.4.1 Gamma Camera Imaging

Gamma camera imaging is different to the anatomical imaging techniques as the source of the radiation is from within the patient. The patient is injected with a pharmaceutical labelled with a radioactive isotope which is taken up within the body. The radioisotope emits the radiation detected by the gamma camera providing a 2D map of the uptake within the body.

### 2.4.2 SPECT

SPECT utilises the same techniques as gamma camera imaging, but it acquires data from multiple angles enabling a 3D data set to be obtained. A single planar detector module is utilised as the imaging plate and multiple modules can be placed in the ring around the subject to increase detector sensitivity hence reducing acquisition times.

## 2.5 Positron Emission Tomography

### 2.5.1 Introduction

Positron Emission Tomography (PET) is a functional process imaging modality which can provide a 3D image of the subject being scanned. The solution containing a positron emitting radioisotope which is chemically bound to a metabolically active molecule is injected into the patient. The metabolically active molecule is taken up within the body and greater concentrations are found in the target tissues towards which the ligand shows the greater affinity. In the case of detecting cancer, the metabolically active molecule selected must show the greatest affinty to tissues with aggressive growth as cancerous cells replicate much faster than healthy tissue.

David Kuhl and Roy Edwards proposed the concept of emission and transmission tomography in the 1950s with Michel Ter-Pogossian, Michael E. Phelps et al. at the Washington University School of Medicine, developing tomographic imaging devices shortly after [12] [13]. In the 1970s, Tatsuo Ido at the Brookhaven National Laboratory described the synthesis of fluorodeoxyglucose (FDG), a substance which shows an affinity for sites of glucose consumption. As malignant cancerous tumours grow quickly, they utilise greater quantities of glucose than most healthy tissue, thus demonstrating a higher uptake of FDG. If the deoxyglucose is bound to the fluorine positron emitter, the tumour sites have higher uptake of the fluorine which can then be observed using a PET study.

### 2.5.2 Positron Emission

Positron emission is a form of beta decay, sometimes referred to as a beta plus decay ($\beta+$). In positron emission, the isotope has an abundance of protons which results in the some of the protons being converted to neutrons and positrons via the weak nuclear force. The positron is then emitted with electron neutrino. A decay of a commonly used positron emitter fluorine-18 can be described by:

$$^{18}_{9}F \rightarrow \ ^{18}_{8}O + \ e^{+} + \overline{\nu}_{e} + 1.656 \ MeV$$

A positron emitted by $^{18}_{9}F$ has a maximum kinetic energy equal to 1.656 MeV and these free positrons proceed to lose their kinetic energy through a series of collisions with atoms in the body. The modal positron emission energy and the mean range of the positrons in water from some commonly used PET isotopes is shown in Table 2.1

Once the positron has an energy low enough to bind with a free electron in the body, an annihilation occurs between the particle and the anti-particle producing two 511 keV annihilation $\gamma$ photons travelling $180^{o}$ apart from each other. In this

Table 2.1: Modal Positron Energy and Mean Range in water [14]

| **Isotope** | **$E_{mode}$(MeV)** | **Mean Range (mm)** |
|---|---|---|
| Na-22 | 0.216 | <0.6 |
| F-18 | 0.250 | 0.6 |
| C-11 | 0.386 | 1.1 |
| N-13 | 0.492 | 1.5 |
| O-15 | 0.735 | 2.5 |
| Ga-68 | 0.836 | 2.9 |
| I-124 | 0.686(11%) | ≈3 |
| | 0.974(12%) | |
| Rb-82 | 1.524 | 5.9 |

reaction, charge, momentum and angular momentum are conserved. The position of the annihilation is different to the location of that positron's emission, the magnitude of the distance being related to the kinetic energy of the emitted positron.

### 2.5.3 PET Imaging

PET imaging is different to most other imaging techniques as the source of the radiation is from within the subject. The radioisotope is injected into the subject with a greater concentration of positrons found in areas of higher uptake. Subsequently, there are a greater number of annihilation photons originating from these areas. The photons that travel out of the body propagate in all directions and if travelling in the direction of the detector rings, can interact in the scintillator crystal with "coincident" events recorded. Coincident events are two interactions which occur within a specified time window. The system detects that interactions which occur within this window are a result of a single annihilation. The two photons measured may in fact not be from a single annihilation, however the system has no way of differentiating this and accepts the data. The computer processing system then draws a Line of Response (LOR) between the two events which represents the line along which the annihilation was most probable. A detailed analysis of how LORs are stored from a PET study is discussed in Section 2.11.2.

Over long acquisition times, the LORs overlayed illustrate the areas of highest uptake and image reconstruction shows a 2D map of the areas of greatest concentration, and hence the greatest probability of the presence of the target tissue. Multiple slices can be acquired along the axial direction enabling a 3D reconstruction of the subject to be created.

## 2.6 PET Scanners

### 2.6.1 Introduction

As illustrated in Figure 2.1, a PET scanner consists of a large ring containing numerous modules which contain scintillator crystals and acquisition electronics coupled to data processing computers. The patient is placed at the centre of the ring and the emitted photons from the subject are detected by the scintillator crystals and processed by the electronics and computers to reconstruct a 3D image of that subject. A critical analysis of each component of the imaging process in the context of the work presented in this thesis is provided in the following subsections.

### 2.6.2 Scintillator Crystal

The scintillator crystal is key to the detection efficiency of PET scanners. Photons which interact through a photoelectric absorption or Compton scattering within the scintillator crystal excite the electrons within the scintillator. As an electron decays back to its ground state it creates a small flash of light. The visible wavelength photon interacts within the photodetector and the flash of light is converted into an electrical signal. Gamma photons are too energetic to interact directly with the photodetector requiring this conversion of the gamma into a visible wavelength photon.

Scintillators are most commonly defined by their light output (typically specified by photons per MeV of incoming gamma radiation), the light decay time (a measure of the length of the flash of light) and effective atomic number, all important

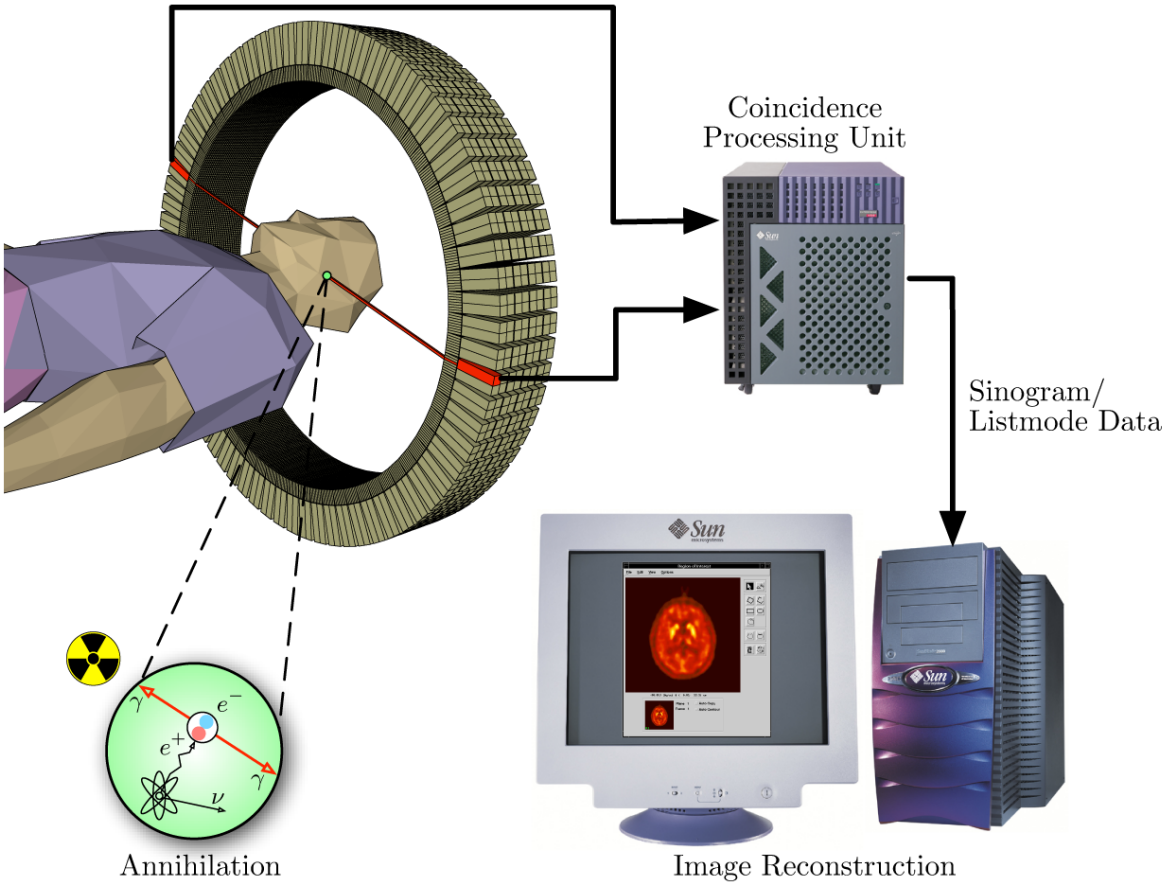


Figure 2.1: Schema of a typical PET acquisition system [1]

parameters when considering their application.

Some common scintillators used in PET scanners together with their properties are shown in Table 2.2 [15]. The light output given in this table is normalised to the output of the commonly used NaI scintillator.

Table 2.2: Scintillator properties [15] [16]

| | NaI | BGO | LSO | YSO | LYSO |
|---|---|---|---|---|---|
| **Decay Time(ns)** | 230 | 300 | 40 | 70 | 42 |
| **Relative Light Output** | 100 | 15 | 75 | 120 | 75 |
| **Effective Z** | 51 | 74 | 66 | 34 | 65 |
| **Photon mean free path at 511 keV (mm)** | 30 | 11 | 12 | 26 | 12 |
| **Max emission wavelength (nm)** | 410 | 480 | 420 | 420 | 425 |

An ideal scintillator has a relatively fast decay time, high light output and high effective atomic number (Z) ensuring high count rates and efficiency.

A newly developed scintillator is cerium doped lutetium yttrium oxyorthosilicate (LYSO) and has parameters extremely suitable for application in PET studies. It is extremely similar in its properties to LSO and has an effective atomic number of 65, a density of 7.1 g/cm$^3$, and the photon mean free path is 12 mm at 511 keV. It is a relatively fast scintillator with a decay time of 42 ns and has a light yield that is similar to LSO as well [16].

### 2.6.3 Photodetectors

The conversion of the flash of light into an electrical signal is undertaken by the photodetectors which are optically coupled to the scintillator crystals. Numerous devices have been used for this application in detector electronics [17] with a summary of commonly used photodetectors given below.

#### 2.6.3.1 Photomultiplier Tubes

Photomultiplier Tubes (PMTs) utilise a cascaded series of dynodes, each at a slightly higher potential than the previous. The visible wavelength photons from the scintillator photoelectrically absorb within the photocathode window of the PMT, ejecting an electron. This photoelectron escapes from the photocathode and is accelerated towards the next dynode by the strong electric field and when that electron interacts with the dynode, more electrons are released. Each of these new electrons travels to the next dynode where each creates even more electrons. This multiplication process continues until the last dynode where there is a sufficient number of electrons to create a discernible current pulse for the electronic processing system to detect.

PMTs have a relatively fast response and very high gain making them ideal for studies with high count rates. The major disadvantage of PMTs is that they take up a large volume meaning one-to-one coupling between a small scintillator and detector is not possible as required in this study. Furthermore, they require very high voltages for operation and are susceptible to magnetic fields preventing the development of hybrid PET/MRI systems using PMTs. Determination of the DOI using PMTs requires intelligent light encoding techniques or signal amplitude based caclulations to predict the DOI as outlined in Section 2.9.

### 2.6.4 Position Sensitive PMTs

Position Sensitive PMTs (PS-PMTs) are identical in operation to traditional PMTs, however, they employ a two dimensional array of small anodes on the front face of the PMT. The position is calculated using Anger logic (discussed further in Section 2.8). The two dimensional anode array ensures positional information can be obtained from the crystal while also retaining the other advantages of PMTs discussed in the previous subsection. Nevertheless, PS-PMTs are still relatively

large and are unsuitable for one-to-one coupling with scintillator crystals

#### 2.6.4.1 Silicon *p-n* and *p-i-n* Photodiodes

Silicon Photodiodes (Si-PDs) are semiconductor devices that are sensitive to the light produced by the scinintillator crystals. They have a reverse bias voltage applied across them which increases their sensitivity. As an optical photon from the scintillator interacts in the semiconductor material, an electron is excited, making that electron mobile and creating a positively charged hole. If the interaction occurs within the photodiode's depletion layer, the electron and hole charge carriers are moved by the electric field, producing a photocurrent.

*p-n* and *p-i-n* photodiodes are suitable for use in a large number of applications as they are inexpensive and very small. They can also be placed in arrays, an extremely useful feature when considering one-to-one coupling between scintillators and photodetectors as proposed in this study. The significant disadvantage with PDs is that for each incident photon, there is only one electron and hole produced requiring further amplification for use in a detector system. The amplification stage requires further electronic complexity and can create noise in the electronic signal making analysis of the pulse challenging for other stages within the electronics.

#### 2.6.4.2 Avalanche Photodiodes

Avalanche Photodiodes (APDs) utilise *p-i-n* diode structures which are operated at higher reverse bias voltages than traditional PDs. As a photon strikes the depletion layer of the APD, charge carriers are created which are then accelerated by the electric field. As each carrier gains energy, secondary carriers are created which then generate other electron-hole pairs. The multiplication factor of APDs is highly dependent on the bias voltage.

#### 2.6.4.3 Silicon Photomultipliers

Silicon Photomultipliers (SiPMs) are semiconductor devices made up of an array of APDs on a silicon substrate. Each APD is extremely small, with sizes varying from 20 to 100 $\mu$m meaning an extremely high number can be placed on a small area, upto 1000 per square millimeter. A gain of $10^6$ can be achieved as a result of the high gain of the APD and the sheer number of APDs in a small area. SiPMs operate independently from magnetic fields and their small size and high output enable one-to-one coupling with scintillators.

### 2.6.5 Detector Electronics

The electrical signal pulses produced by the photodetectors are passed through processing circuitry before being used to record the interactions. The pulse height from the photodetectors is assumed to be proportional to the energy that was deposited in the interaction with each pulse then passed through a differential discriminator. The differential discriminator is made up of a lower level discriminator (LLD) and an upper level discriminator (ULD) to reject the pulses that are outside the required energy and timing range. This effectively creates an energy window which accepts depositions between only specified energies. By setting a low LLD greater sensitivity can be achieved as higher numbers of pulses are accepted, however, these pulses can be a result of noise and scatter. Therefore, it is important to set an LLD value which maximises the sensitivity while also rejecting noise and scatter.

The pulses from the photodetectors are also passed through a constant fraction discriminator (CFD) which creates a digital pulse when the electronic pulse reaches a certain amplitude. These digital pulses are used in the coincidence circuitry to determine coincidences. A coincidence corresponds to any two interactions which are measured within a "coincidence window", often in the order of nanoseconds.

## 2.7 Limitations of PET

CT and MRI are imaging modalities which have been used in clinical practice over a long period of time, hence there exists a large volume of research leading to optimisation of the technology. PET, on the other hand, is a relatively new technology, with significant limitations which require addressing in order to ensure advancement in its performance. A number of the most significant limitations are outlined below in the following subsections.

### 2.7.1 Depth of Interaction Errors and the Radial Elongation Artefact

The ability to detect the depth of interaction within the crystal is perhaps the most important factor which needs consideration when attempting to maximise the spatial resolution of the system (especially in small animal imagers). Most systems cannot determine the exact position within the detector crystal at which the gamma interaction has taken place. As a result, the system determines an arbitrary point within the crystal for which it will assume the interaction has taken place (often the centre). For LORs joining two off-centre detector modules, there can be significant errors in the DOI as illustrated by Figure 2.2. The solid line with arrows indicates the path of 2 unscattered photons. These photons both pass through some scintillator crystals before they interact with another crystal. The system has no method of determining the exact position of interaction within the crystal and hence assumes all interactions take place at a fixed depth in the crystals. The dashed line shows the system determined LOR; there is a noticeable difference between the position of this line and the actual LOR. The effect of these radial elongation artefacts increase as the angle between the propagation direction of the photon and the front surface of the detector module moves away from the normal. Employing DOI information allows the interaction depth to be known more accurately, hence the reduction in the radial elongation artefact.

Figure 2.3 shows a reconstruction of a number of point sources with the radial

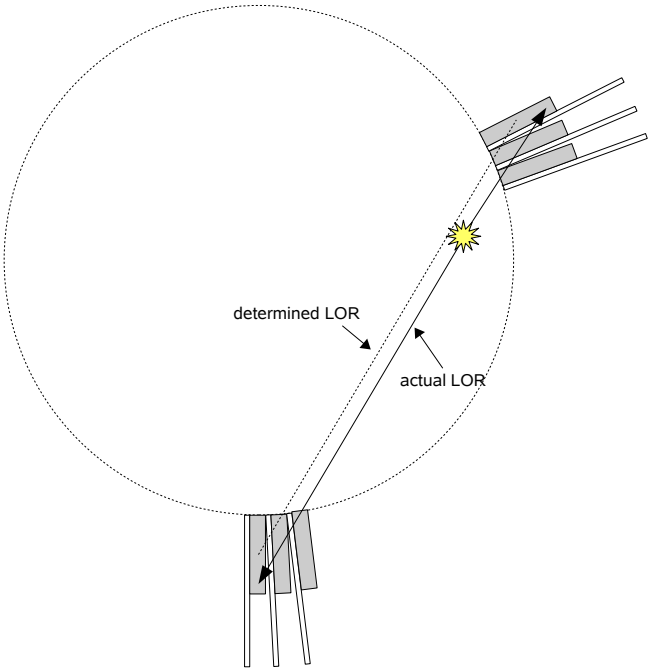


Figure 2.2: The Depth of Interaction Error illustrating the difference between the determined LOR and the actual LOR

elongation artefact becoming more observable towards the edge of field of view (FOV). The left most point in the reconstructed image is at the centre of FOV.

### 2.7.2 Scattering

The path that photons take is highly dependent on their energy and the medium in which they propagate as described in Section 2.2. The photon attenuation coefficient ($\mu$) is a measure of the amount of attenuation observed for photons in a material. The intensity of the measured number of photons ($I$) with respect to the initial intensity ($I_0$), attenuation coefficient and path length ($x$) is expressed by Equation 2.2.

$$I = I_0 e^{-\mu x} \tag{2.2}$$

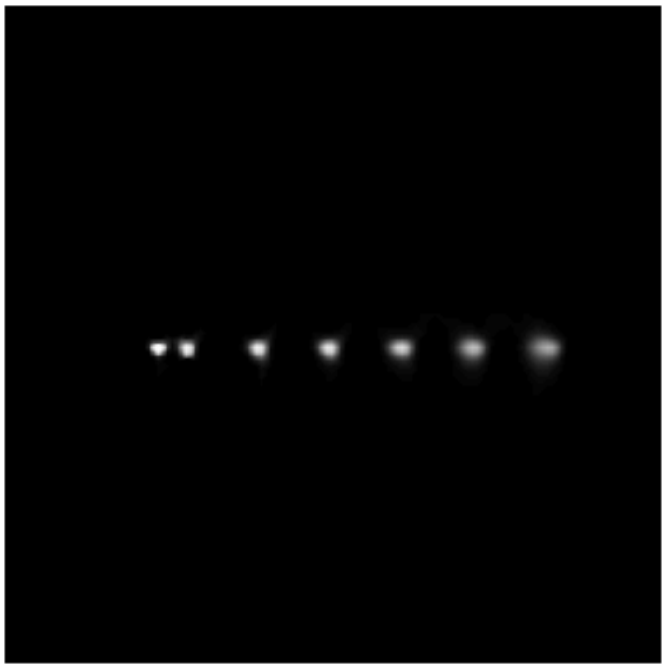

Figure 2.3: The radial elongation artefact seen across the FOV in a reconstruction of point sources. The left most point is at the centre of the FOV and the distance between the leftmost and adjacent source is 10mm. Each adjacent source is then placed a further 20mm apart with the outermost source at 110mm from the centre of FOV. Note the elongation of the point sources as they are moved further away from the centre of FOV.

The attenuation coefficient can be split into components as a result of the different interaction type for a photon (photoelectric effect, Compton scattering and pair production). Figure 2.4 shows the attenuation coefficients for photons travelling in water (a suitable medium when simulating the human body which is 70% water). It shows the contribution of photoelectric effect, the Compton effect (incoherent scattering) and pair production as well as the total attenuation coefficient.

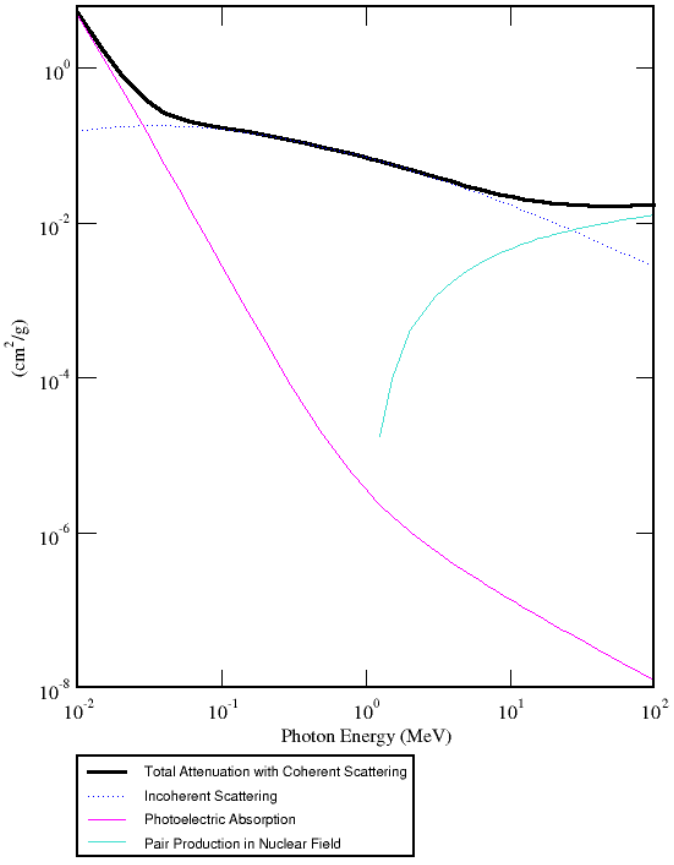


Figure 2.4: Photon attenuation coefficients in water [2]

At low energy, the dominant interaction process is the photoelectric effect, however as the energy increases, the Compton scatter contribution increases. At energies

above 1022 keV ($2m_0c^2$), pair production becomes the dominant process. As annihilation photons from PET are emitted with an energy of 511 keV, the Compton effect becomes the most significant effect.

A number of effects reduce the accuracy of the acquired image as a result of recording incorrect LORs. These are scattered, random and multiple coincidences as illustrated in Figure 2.5.

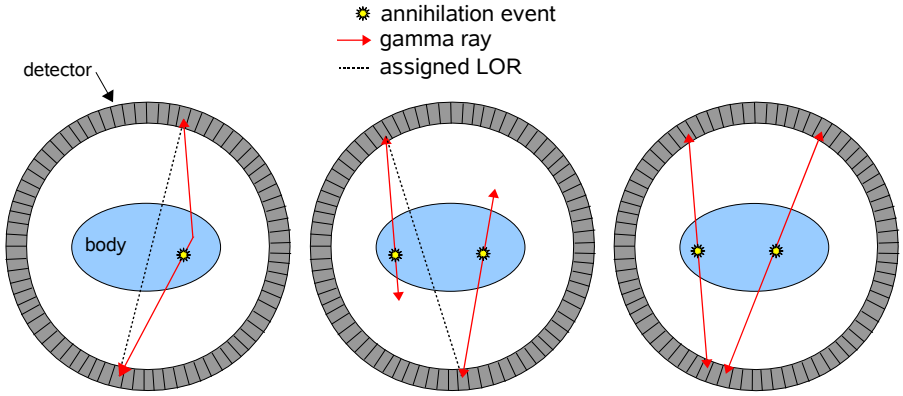


Figure 2.5: Scattered, Random and Multiple Coincidences which may be recorded by the PET scanner

A scattered coincidence is caused by one of the annihilation photons scattering within the body while the other photon remains unscattered. A random coincidence occurs when one photon from each of 2 separate annihilations is absorbed within the body (or misses the detectors without interacting) and the remaining 2 photons from different annihilations create a coincidence. A multiple coincidence refers to 2 or more annihilation events both interacting in the detector within the specified coincidence window. These incorrect LORs have a detrimental effect on the quality of the image by creating "noise" within the reconstructed image, making lesion detection a greater challenge.

A simple method of reducing the scatter contribution is by using a collimator which reduces scattered photons as shown in Figure 2.6. A collimator is a large lead grid which is placed near the front face of the scintillator crystal, reducing the

angle of acceptance of photons originating from the source. The collimator can also incorrectly reject unscattered photons if their direction is not within the acceptance angle. The use of collimators result in what is known as "2D PET" which has decreased sensitivity but less scatter, whereas "3D PET" does not use a collimator and results in better sensitivity but greater susceptibility to scatter [18].

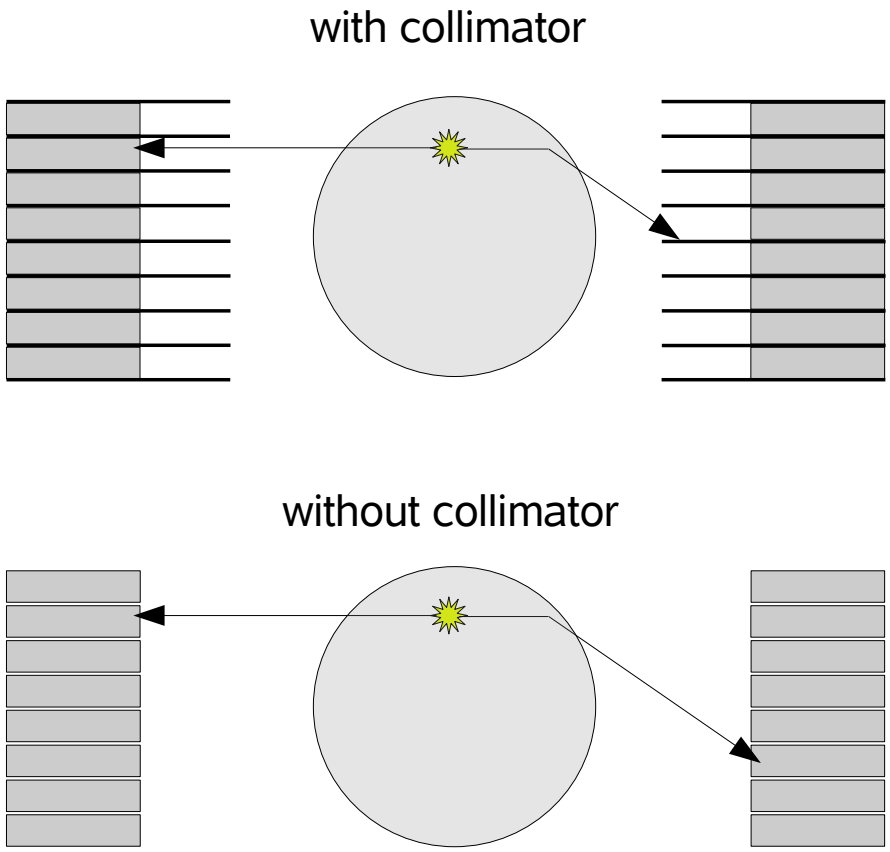


Figure 2.6: Photon acceptance in detectors with and without a collimator. The sensitivity of the scanner significantly decreases when a collimator is used as the acceptance angle of the photons is reduced

### 2.7.3 Positron Range

The position of the positron annihilation is different to the position of emission from the uptake as shown in Figure 2.7. The positrons emitted by an isotope have

kinetic energy which is lost through collisions with atoms in the body and the positron only annihilates once its kinetic energy is zero (or almost zero in some instances).

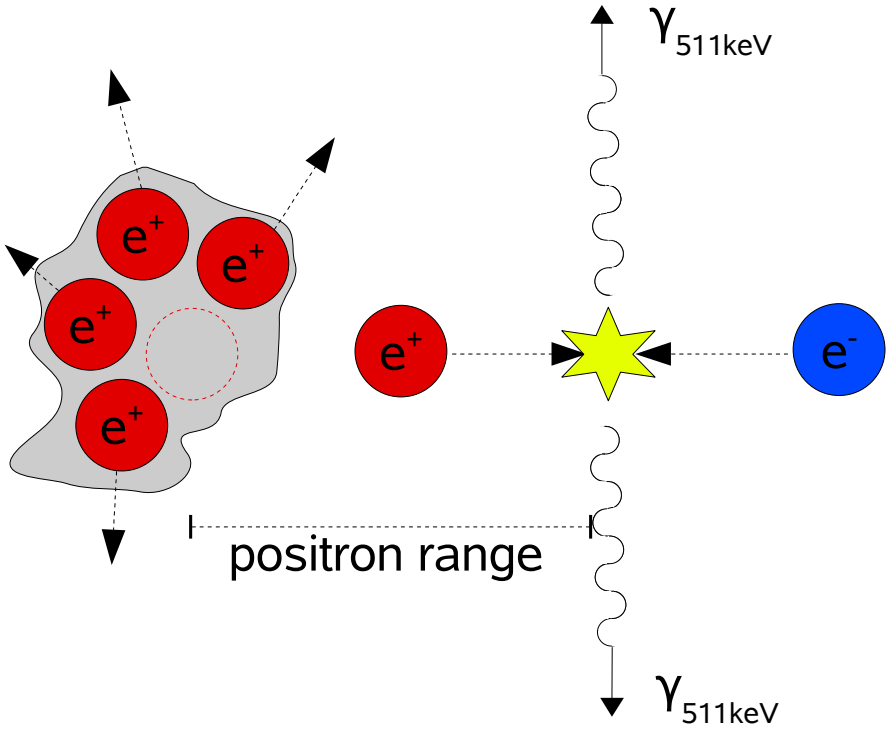


Figure 2.7: The distance travelled by the positron before annihilation known as the positron range

The effect of the positron range varies depending on the isotope selected, with high energy positron emitters naturally having the greatest positron range. Table 2.1 previously presented the positron energy and range for a number of commonly used positron emitters [19].

The positron range contributes to the fundamental limit of resolution within a PET scanner and no improvement of detector technology within the scintillator or electronics can provide resolution smaller than the positron range. The positron range can be reduced slightly by magnetic fields [20] [21] and has been a focal point in the development of PET/MRI scanners.

The relationship between the positron range and the spatial resolution can be expressed

In F-18 studies, the resolution limit for small animal PET investigations is currently below 1 mm, however the blurring due to the positron range results in a decrease in the resolution of between 0.1 and 0.2 mm full width half maximum (FWHM), with a mean range between 0.3 and 0.4 mm [22] [21].

#### 2.7.3.1 Annihilation Photon Non-Colinearity

The net momentum in a positron/electron annihilation, like in all mechanical interactions, is conserved. Annihilation photons are considered to travel at $180^o$ to each other, however this is not always the case. Figure 2.8 illustrates two conditions of positron annihilation. Annihilation photons only travel at $180^o$ to each other when the momentum before the annihilation is zero; that is, the positron has zero residual kinetic energy after emission. If the positron combines with an electron and annihilates while it still has residual kinetic energy, the net momentum before the annihilation is not zero and hence the net momentum after annihilation cannot be zero.

The photon non-colinearity affects the resolution of the scanner, contributing a gaussian blur of approximately 0.3 mm for a 15cm diameter scanner [22]. More generally, the blurring effect of the non-colinearity ($\Delta_{nc}$) can be expressed approximately as:

$$\Delta_{nc} = 0.0022 \times D \tag{2.3}$$

where D is the diameter of the scanner expressed in millimeters [23].

### 2.7.4 Low Sensitivity

PET studies have very low sensitivity and often take in the order of tens of minutes as the detectors cover a very small solid angle in the $4\pi$ geometry. It

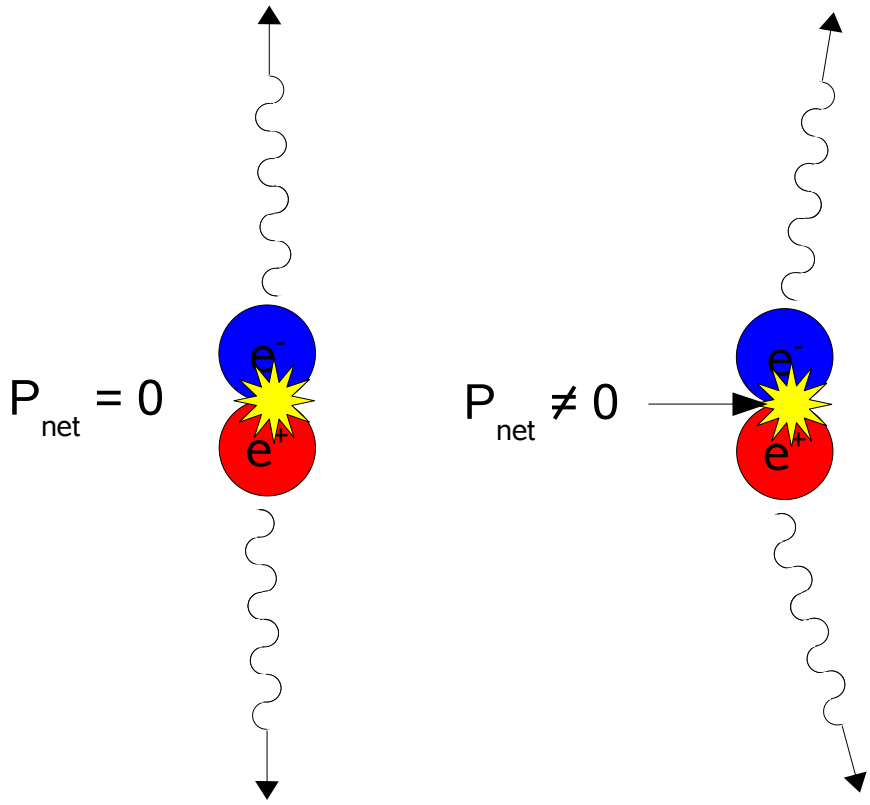


Figure 2.8: The photon non-colinearity effect. The left image shows the net momentum ($P_{net}$) afer annihilation being zero while the right image shows $P_{net}$ after annihilation not being zero

is, therefore, very important for all photons entering the scintillator crystals to be detected. Annihilation photons with energy 511 keV have an attenuation coefficient of 0.83 $cm^{-1}$ in LYSO resulting in approximately 87% of normally incident photons being absorbed within 2.4 cm of crystal (as the detector module in this thesis proposes). Increasing the crystal depth provides improved sensitivity at the expense of increased radial elongation.

## 2.8 Current PET Scanner Design

The original design for PET systems relied on a single photomultiplier tube (PMT) for each scintillator crystal [24] [25] [26]. A large number of commercial PET scanners now use a modular detector design with a monolithic block of scintillator

crystal coupled to 4 PMTs of which a specific example is introduced in [27]. The light produced from the gamma ray interaction in the crystal is detected by all 4 PMTs and the location of interaction in the axial and tangential directions is determined by the relative response of each of the PMTs using Anger logic [28]. The magnitude of the voltage signal in each PMT determines how the light from the interaction is shared between the PMTs, with the PMT signal ratios used to locate the x and y coordinates of the interaction according to Equation 2.4.

$$x = \frac{A+B}{A+B+C+D}; \quad y = \frac{A+C}{A+B+C+D} \tag{2.4}$$

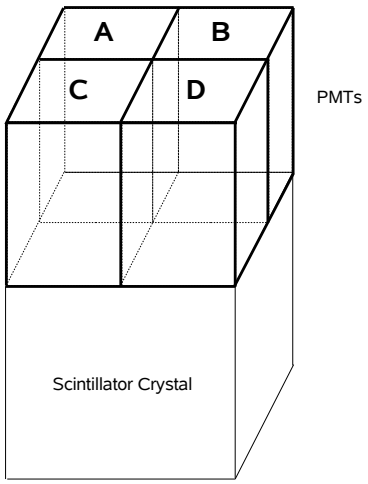


Figure 2.9: Position of PMTs used for Anger logic calculations

The traditional Anger logic method can become problematic due to variances in PMT operation resulting in non-symmetrical light isocontour plots around each block.

The spatial resolution of PET systems can be improved by placing small saw cut grooves to separate the crystal into many quasi-discrete elements. The crystals used by Casey et al. [27] are $30 \times 4 \times 4$ mm$^3$ (surface edges of crystal are 4 mm and depth is 30 mm). The saw cut grooves ensure light produced in a given element

remains in the correct tangential and axial positions when it reaches the photomultiplier tubes. In order to further improve spatial resolution, smaller crystal elements can be used, however the large size of existing PMTs make this infeasible. Furthermore, if large numbers of crystals are required, there must be numerous PMTs with the resulting increased electronic channel density making the systems costly and challenging to maintain.

Reducing the size of these crystal elements improves spatial resolution but does not provide any depth of interaction information. The limitations of this approach include:

- the fundamental limit on the size of the detector module due to the size of the photomultiplier tubes
- the size of the crystal element due to the thickness of the saw cut
- the amount of dead space in the block which increases as crystal elements become smaller leading to reduced detection efficiency when using long thin crystals, offsetting the improvement in spatial resolution [29].

The size of the photomultiplier tube is a significant factor as it is often 10 cm or longer, some with cross sectional areas of approximately 10 $cm^2$. Smaller PMTs have been developed with much smaller cross sectional areas however remain significantly larger than other newer solid state detector devices.

## 2.9 Depth of Interaction

As stated in Section 2.7.1, the DOI is an important feature that can be used to minimise the radial elongation artefact.

Numerous techniques have been developed to determine the depth of interaction including:

- phoswich detectors using multiple scintillators with unique light decay properties [15] [30] [31]

- dual layer detectors with layers offset by half the crystal pitch [3] [32]
- the ratio of light determined by photodetectors placed at either end of the crystal [33] [4]
- multiple offset layer detectors using a novel light sharing method [5]
- multiple layers coupled to individual detectors [6].

PMTs have been the most convenient and best method of collecting light from the scintillator crystal and converting it to an electrical signal. They offer exceptional gain, fast response time and a high signal-to-noise ratio and hence are utilised in many designs for DOI detectors. While these techniques are innovative and demonstrate an improvement in the measurement of the DOI, the detector modules remain bulky due to the large size of the PMTs, with a miniaturised and cheaper solution required.

### 2.9.1 Phoswich Detectors

Phoswich (**phos**phor sand**wich**) detectors utilise multiple layers of different scintillator material, each layer having unique light decay properties. The light pulse shape when analysed will distinguish the layer from which the scintillation event occurred. Figure 2.10 illustrates a 2-layer phoswich and the light pulses from photon detections in each layer. The top bismuth orthogermanate (BGO) layer demonstrates a slower response while the lower lutetium oxyorthosilicate (LSO) has a much faster response.

When designing phoswich detectors, it is important to select two scintillators of which the light decay properties are significantly different for easy identification of the pulse type (and hence the location). Detectors utilising both fast and high light output scintillators yttrium oxyorthosilicate (YSO) and LSO have been investigated in [15]. Some commonly used scintillators and their properties were listed in Table 2.2. In order to have efficient and correct identification of the pulse type, accurate

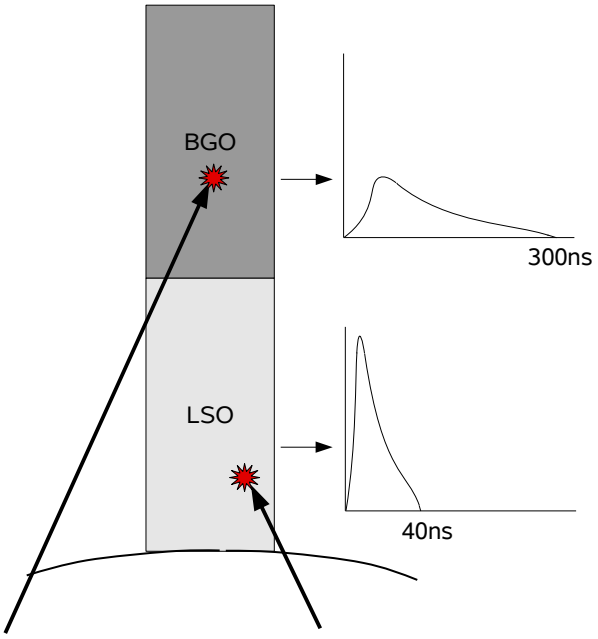


Figure 2.10: A 2-layer phoswich with a layer of LSO and BGO showing typical light output for scintillations within each layer

timing resolution must be available within the detector electronics, another level of complexity within the design.

Another compromise that must be made is the light output (quantum efficiency) of the scintillator. Bismuth orthogermanate (BGO) has a high effective Z meaning a greater probability of photon interaction, but it also has a relatively low light output. Therefore, any advantage gained by having a high Z scintillator may be reduced by having a low light output.

### 2.9.2 Offset Crystal Layers

A novel solution proposed by Liu et al. [3] and Zhang et al. [32] is to use a light sharing technique and a newer type of PMT, a position sensitive PMT (PS-PMT) [34] [35]. PS-PMTs have the ability to localise the position in the tangential and axial directions more accurately than a traditional PMT hence can provide superior resolution.

The light sharing technique is the tool that can be used to provide the depth of

interaction information. The implementation of Liu et al. uses two layers of crystals (each layer is approximately 10 mm long) that are constructed in arrays. The lower layer has one extra element in both directions and the top layer is placed on top of the upper array with a shift of half the element pitch in both directions as shown in Figure 2.11. When a photon is absorbed in the top layer of scintillator, the light from that scintillation travels downwards and is shared in 4 elements of the lower block. The centroid of the measured light output distribution is placed at the centre of the 4 blocks from which the light travelled to the PS-PMT. If an interaction occurs in the lower layer, the centroid of the light output distribution is determined to be half a crystal element away from the centroid for photons interacting in the upper layer. The DOI of the interaction can be determined by matching the output of the PS-PMT with a position map. The version of Zhang et al. relies on a similar light sharing technique with offset crystals within the two layers. However, it employs a 2 $\times$ 2 array of PS-PMTs for more accurate positioning at the back end of the scintillator to provide improved accuracy in the position map resulting in improved DOI calculation.

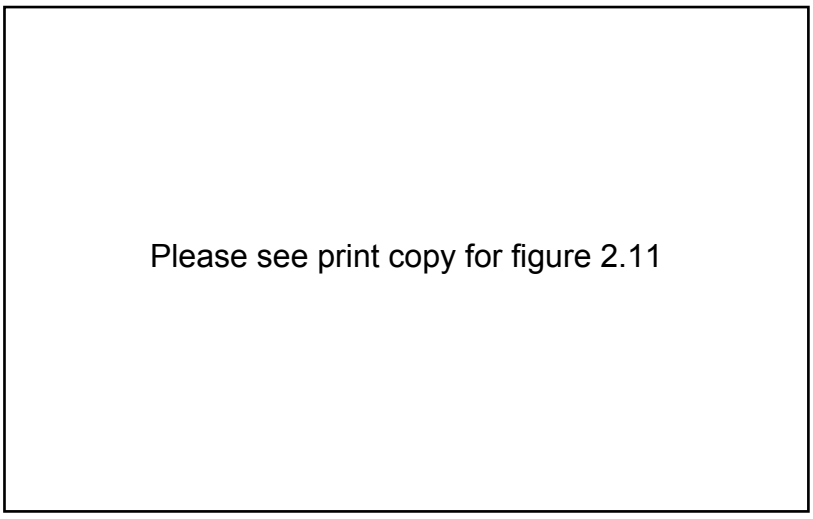


Figure 2.11: The detector module proposed by Liu et al. [3]

### 2.9.3 Multiple Detectors at Both Ends of Detector

A number of publications [33] [4] outline the development of detectors which have detectors at both ends of the scintillator crystal. These modules use both PMTs and silicon PDs with one placed at either end of the scintillator. The scintillator is segmented into small, long elements (3 mm $\times$ 3 mm $\times$ 30 mm) and placed in an array. Early generation designs for this module had 2 $\times$ 2 arrays whereas newer designs contain 8 $\times$ 8 arrays. A PD is placed on top of each crystal element to enable 1-to-1 coupling. A schematic of the proposed detector in a typical acquisition is shown in Figure 2.12.

The PMT provides excellent timing resolution and energy discrimination while the 1-to-1 coupling of PDs to the crystal allow crystal identification and the DOI. The energy deposited is determined by the summation of the PMT and PD signals while the depth of interaction is given by the ratio between the PD signal and the summed PD and PMT signals.

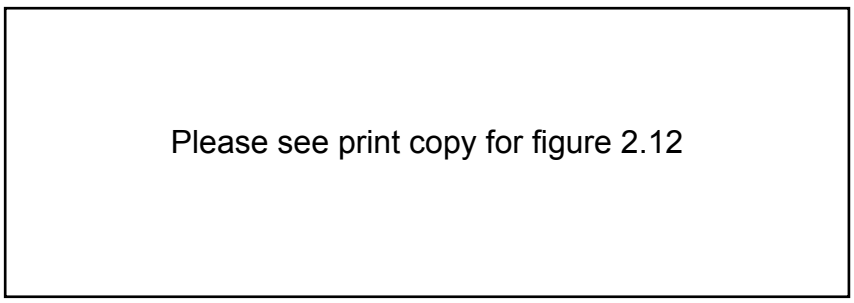


Figure 2.12: The detector module proposed by Huber et al. [4]

### 2.9.4 Multiple Offset Layers Using a Novel Light Sharing Method

Murayama et al. [5] have proposed a detector with a depth encoding scheme. The detector consists of multiple layers of rectangular scintillator blocks optically coupled at the bottom layer to 4 PMTs or PS-PMTs.

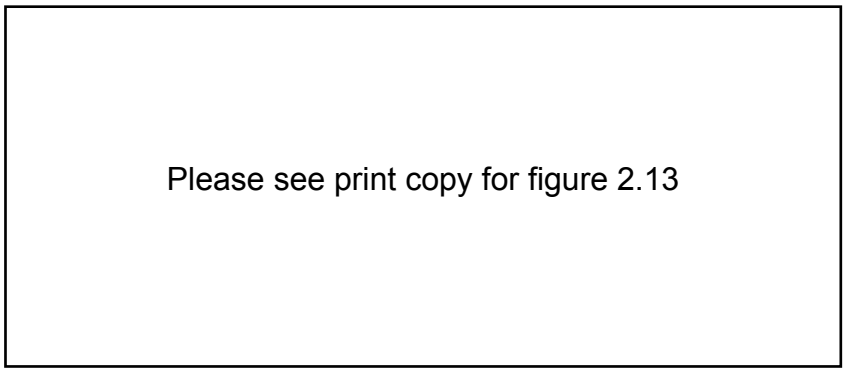


Figure 2.13: The detector module proposed by Murayama et al. [5]

Each layer of scintillator consists of a 2 × 2 array with each layer also containing unique light sharing channels. Crystals within a layer are separated by air gaps or various coupling compounds and separated from specified elements by refractive materials (each layer with a unique separator). This ensures that pulse peaks are observed at different positions at the PMTs as shown in Figure 2.14.

The output of each PMT is added to determine the energy deposited and is also used for energy discrimination. The tangential and axial position of the interaction is determined using Anger logic and the DOI is measured by matching the light output position to the known pulse peak positions from the different crystals had the energy deposition occurred there.

Another proposed model with a novel light sharing encoding scheme has been developed by Tsuda et al. [6]. The jPET-RD is a 4 layered small animal PET scanner. The four layers of LYSO are packed in 12 × 12 arrays placed on a 256

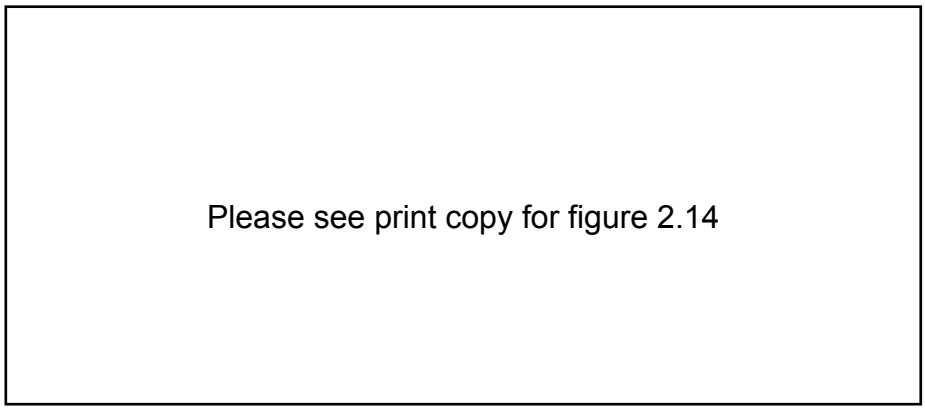


Figure 2.14: The location of the PMT signals for the detector module proposed by Murayama et al. [5]

channel flat panel position sensitive PMT (FP-PMT). Each layer of crystal contains reflectors and air gaps and is placed offset to the surrounding layers as illustrated in Figure 2.15. This creates unique light propagation paths for light created in each layer resulting in the FP-PMT receiving unique pulses of light for each layer, shown in Figure 2.16.

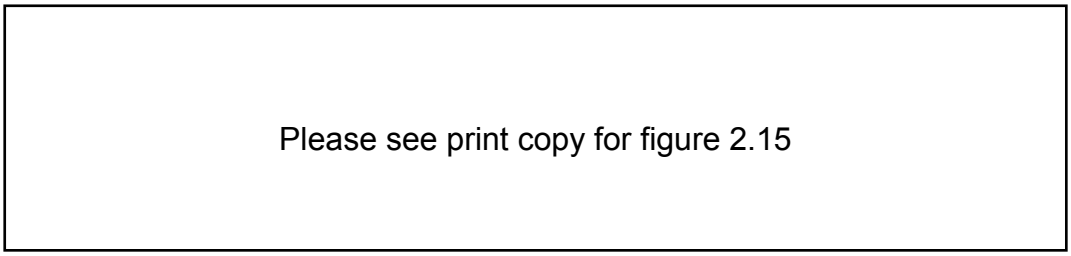


Figure 2.15: A four layer DOI detector consisting of 4 layers of a 6 $\times$ 6 array of LYSO and a PS-PMT as proposed by Tsuda et al. [6]

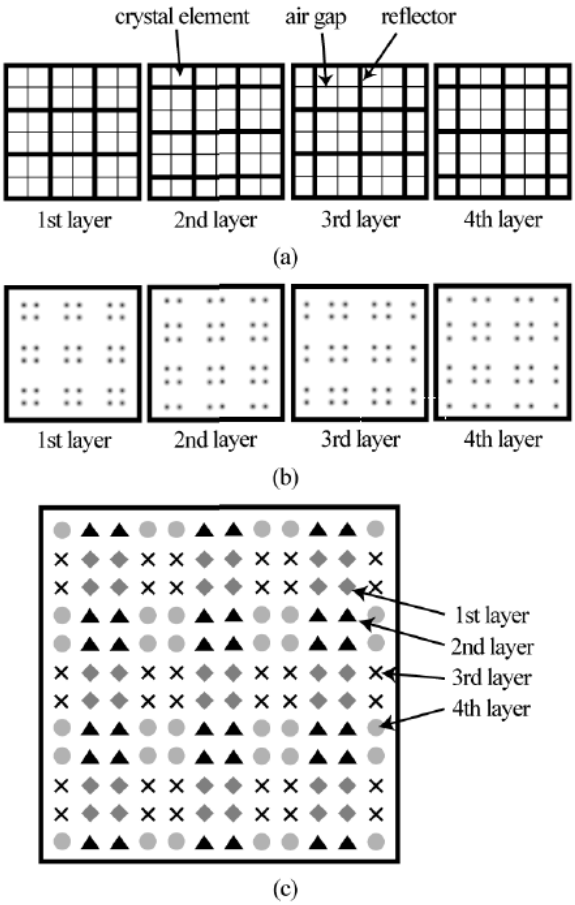


Figure 2.16: (a) The reflector and air gap arrangement; (b) The position histogram recorded by the FP-PMT for pulses recorded in each level of the detector module; (c) Each circle, triangle, cross and diamond correspond to the peak of the pulses received from the 1st, 2nd, 3rd and 4th layers respectively [6]

## 2.10 Monte Carlo Simulations

### 2.10.1 Introduction

Monte Carlo studies are computational algorithms which rely on probabilistic sampling in order to determine approximate solutions to problems. These types of studies are heavily used in physical sciences and mathematical applications, often requiring high powered computers. Initially, a simulation is provided with a fixed input with probability distributions acting on the input producing a statistically accurate output. Monte Carlo studies are used to theoretically predict real life behaviour when designing or developing new technology or when it is impractical

to statistically verify results.

The propagation of a photon of electromagnetic radiation through matter is a probabilistic event, the final path of the photon following the laws of quantum mechanics which make analytical solutions to radiation transport highly challenging and time consuming. Furthermore, studies involving radiation often require significantly large data sets in order to acquire statistically acceptable results with small error limits. If a single photon within a study is to be considered, the results provided would prove to be redundant due to the probability distribution of various events which can occur. If a larger study involving several million or billion photons is considered, an overall picture of the actual study is provided. As interactions between radiation and matter are based largely on probability functions, Monte Carlo simulations become an invaluable tool in particle transport studies, especially in the design and optimisation of detectors for all radiation applications.

### 2.10.2 Geant4

Geant4 (**GE**ometry **AN**d **T**racking) has almost become the standard for Monte Carlo simulations in physics applications including high energy physics, space research and medical physics [36]. It provides comprehensive modelling of most physical processes for nearly all families of particles.

Geant4 utilises Object Oriented Coding in C++, one of the first Monte Carlo packages to utilise this feature. Different elements of the program are contained in separate files, generally independent of each other. Features are available in Geant4 to handle geometry, tracking, detector response, visualisation and the user interface.

The data output of Geant4 can be customised for numerous applications, including internal energy histogramming but requires additional data analysis packages to be installed.

### 2.10.3 GATE

Geant4 provides the means for the GATE package to undertake particle transport. GATE is the **G**eant4 **A**pplication for **T**omographic **E**mission and is a specific sub-application for use in PET and SPECT studies. It replaces the C++ coding required in Geant4 with a much simpler scripting language. Individual input files contain information about each element of the simulation including: the geometry of the scanner, the sources, the phantom, method of data acquisition, the data output and various other physical parameters.

## 2.11 PET Data Storage

PET acquisitions often take in the order of tens of minutes, with high count rates recorded for this period of time. This results in extremely large data sets which must be managed efficiently. Two methods of storing the data are sinograms and list mode data.

### 2.11.1 List Mode Data

List mode data stores information about each coincidence, including a timestamp, the position and energy deposited. This data set is extremely large, typically in the range of tens of gigabytes, however it allows the flexibility of further offline processing. Certain reconstruction techniques allow real time reconstruction of list mode data as well [37] [38], a useful feature in dynamic studies.

### 2.11.2 Sinograms

Tomographic imaging relies on imaging the subject from a number of different angles with the sinogram being an efficient way to store the subsequent information. A sinogram is a matrix which contains data related to the number of counts across the FOV for a given angle of view (known as a projection angle). Figure 2.17 shows a phantom placed at the centre of FOV with 2 areas of high uptake. Also shown are

three projection angles and the counts detected across the FOV for that angle. The number of counts for any given position across the FOV determines the magnitude of the pixel value (0 = white, maximum = black) in the sinogram for that position and the angle of the projection. An item at the centre of FOV would trace out a straight path down the centre of the sinogram, whereas off centre items trace out a path which looks like half of a sine wave, hence the name sinogram.

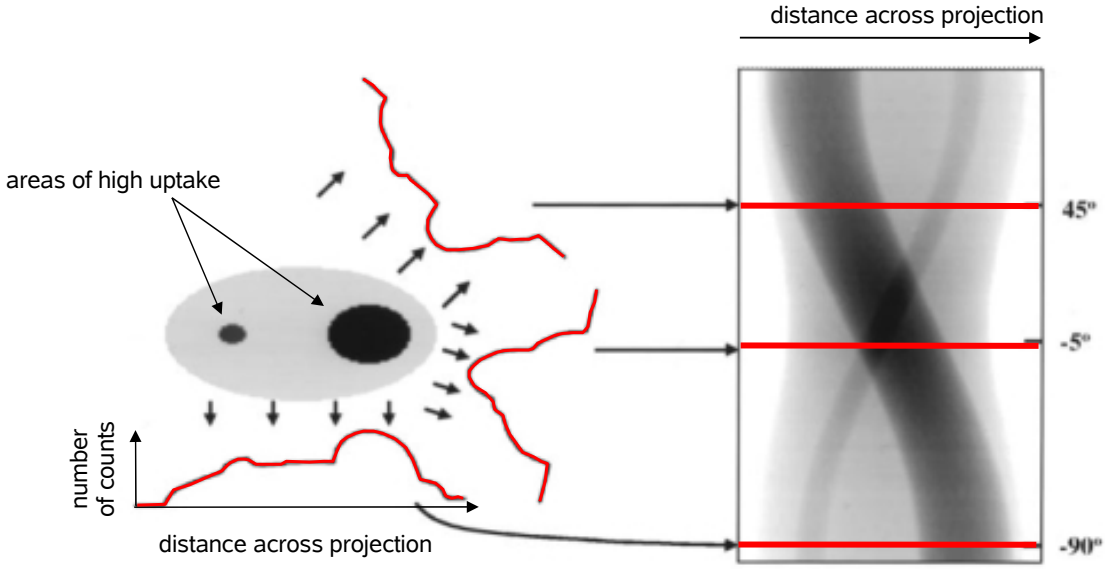


Figure 2.17: A sinogram and the projection data used to determine the values of the sinogram elements in 3 rows [7]

The sinogram is not inherently a useful item for objectively measuring the performance of the scanner but merely an efficient and suitable method for storing the data. Sinograms store only spatial information, rejecting other important parameters such as timing data and energy depositions. This prevents future re-analysis of data, a feature which list mode data allows.

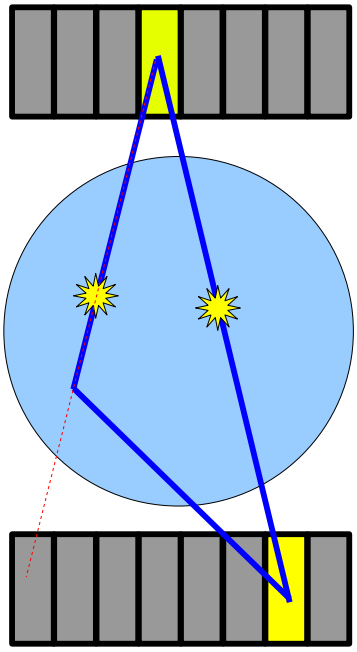

Figure 2.18: Scatter in the axial direction showing how two separate annihilations can result in the same LOR being recorded by the scanner

### 2.11.3 Axial Binning

Annihilation photon pairs are isotropically distributed meaning that each $\gamma$ photon does not necessarily interact within the same axial ring. Coincidences containing two interactions in axially separated positions may arise naturally due to this isotropic distribution. As within the transaxial plane, scatter is a significant issue in the determination of correct LORs in the axial plane. An example illustrating identical LORs arising from 2 separate annihilations is illustrated by Figure 2.18.

Determination of the LOR in the transaxial plane is relatively straightforward as discussed in Section 2.11.2, however, more advanced approaches must be used for axial binning. Single Slice Rebinning (SSRB) [39] is one of the simplest of axial binning techniques. A given oblique LOR is assumed to have an origin from a parallel plane at the midpoint of the axial points of interaction for the two gamma photons. The axial bin represented by this central point is the slice into which the LOR is placed. The process of reconstructing the 3D object is simplified by

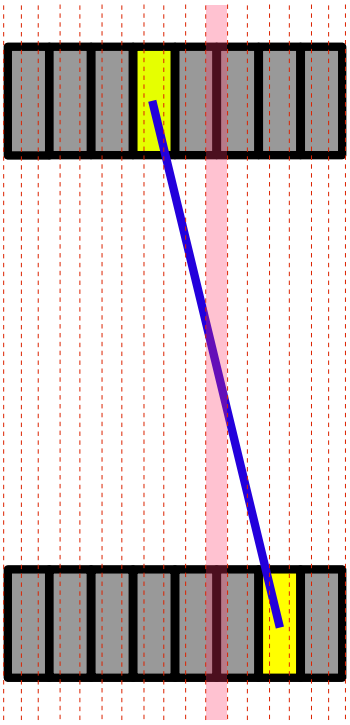

Figure 2.19: The Single Slice Rebinning algorithm. The red slice is determined to be the slice into with the LOR is placed.

considering the object to consist of a number of these parallel 2D slices. The number of slices can be determined by the user depending on the axial resolution and the desired statistical accuracy (ie. number of counts measured in that slice). Figure 2.19 shows a cross section of an 8 ring detector ring outlining the SSRB technique. The yellow volumes are the detectors in which the coincidence is measured while the red dashed lines represent the slices within the 3D image and the highlighted red area shows the slice that the LOR is placed into.

The advantage of SSRB process is its simplicity in implementation and low computational intensity. A full 3D reconstruction with $n$ slices with each taking $t$ seconds to reconstruct requires $nt$ seconds. Furthermore, DOI in the axial direction provides increased accuracy in the determination of the axial slice when acquiring data in 3D mode. A major disadvantage of of the SSRB method is that blurring

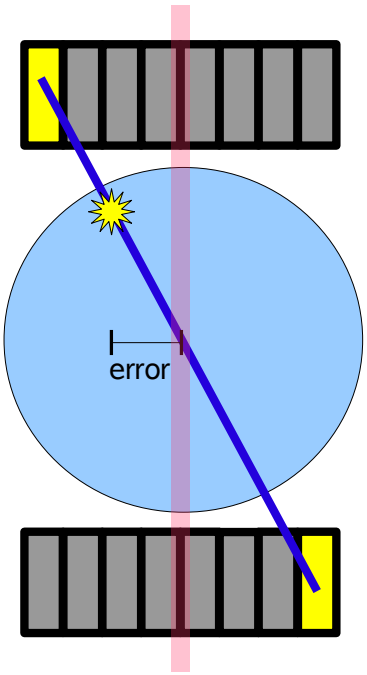


Figure 2.20: Single Slice Rebinning Error

occurs if the actual origin of the LOR is distal from the axial centre of the scanner [40] as shown in Figure 2.20. The annihilation point is axially in a different position to the position determined by the SSRB algorithm. The blurring becomes a significant problem if the subject being imaged has distributed activity over a large area of the FOV.

Collimation using a large lead grid over the detector modules can reduce the effect of scattering within 2D PET studies. In instances where it may be important to acquire 3D PET data, an electronic method of scatter reduction is required. A solution to this problem is by setting a maximum "ring span" or the maximum ring difference across which coincidences can be allowed. That is, if the detector electronics receive two coincidence signals from detector modules outside the specified ring span, the two counts are rejected. This process reduces scatter significantly [18] while also rejecting real data as well hence a reduction in the sensitivity.

For a single data set, there can often be a large number of sinograms. These

sinograms can represent different slices in the axial direction as well as recording information from different "segments". LORs between detectors in the same axial position are known as "direct LORs" and are placed in segment 0. LORs that occur between axially separated rings are known as "oblique LORs" and are placed into different segments. A simple method of visualising which sinogram an LOR is placed into is known as a "Michelogram", a 2D array with N elements in both directions where N is the number of axial rings. Consider the following three LORs shown in Figure 2.21. The LOR represented by the red line is a direct LOR in ring 1, therefore it is placed into the sinogram represented by the element (1,1) in the Michelogram. Similarly, the LOR represented by the blue line is an oblique LOR between ring 5 and ring 2, therefore is placed into the sinogram represented by element (5,2) of the Michelogram. The same logic applies to the final green LOR.

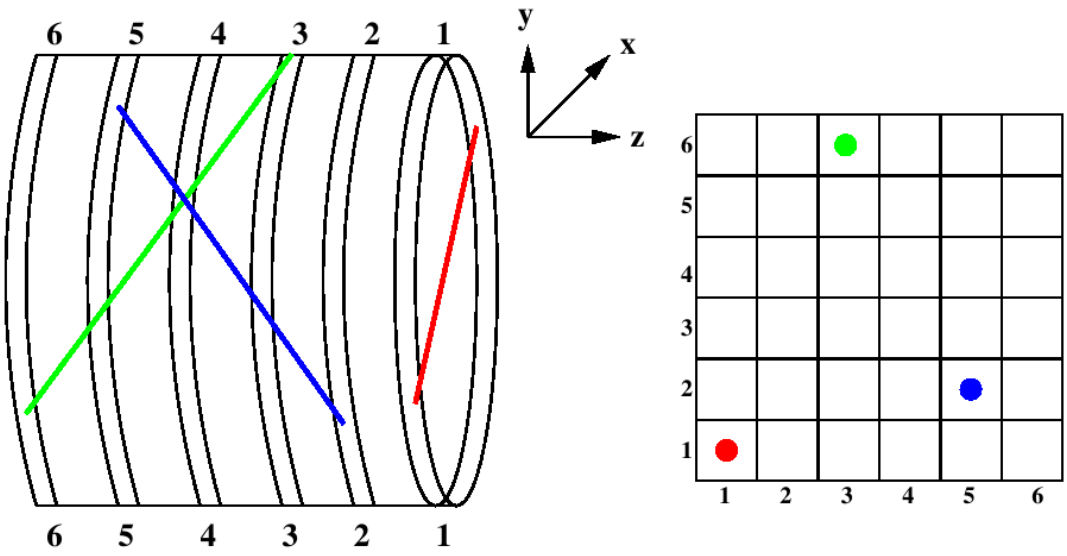


Figure 2.21: Three LORs and the Michelogram illustrating the sinogram into which each LOR will be placed into. [8]

The method used for axial binning within this study is a more crude process where 3D PET data is recorded while not utilising the concept of the Michelogram. Instead, N sinograms are used where N represents the number of detector rings.

The axial centre position of LOR is determined and regardless of whether the LOR is a direct or oblique one, it is placed directly into the sinogram representing that slice.

Numerous other techniques exist for axial binning, including methods for reducing prohibitively large data sets which can be acquired. Consideration of their implementation for this study is covered in Chapter 7.

## 2.12 Image Reconstruction

The goal of all medical imaging studies is to reconstruct an accurate image of the subject being studied. This process is simple in studies that result in 2D images such as x-ray films and gamma camera studies as the total number of counts across a given 2D detection plane are measured and counted. In 3D studies, the process of reconstructing the data is more challenging as numerous sets of data from various projection angles exist and are stored in the form of sinograms. Reconstruction from sinograms is common practice, using both backprojection and iterative techniques. Reconstructions in all of the studies undertaken in this thesis were initially undertaken using an OSEM (Ordered Subsets Expectation Maximisation) [41], an iterative technique written in IDL [42] by Jan Chan from an algorithm developed by Steve Meikle [43].

A committee representing all of the major PET scanner manufacturers has developed the NEMA (National Electrical Manufacturers Association) Standard NU2-2001. This standard defines all of the parameters required when undertaking tests on PET scanners, as well as the requirements for image reconstruction. NEMA does not specify the requirements for quantifying a small animal PET scanner however the methods utilised on full body sized scanners can be amended and modified suitably in order to use with small animal scanners.

As the iterative reconstruction techniques are highly dependent on their input parameters such as the number of subsets and iterations, filtered backprojection

using an unapodized filter (a ramp filter with a cutoff at Nyquist frequency) is the method suggested by NEMA in order to investigate the spatial resolution of PET scanners. As the significant proposed benefit of the novel detector presented in this study is an improvement in spatial resolution, the same method of image reconstruction is used in this instance. Regardless, in certain cases superior reconstruction results can be gained with the use of iterative techniques.

### 2.12.1 Filtered Backprojection

The Inverse Radon Transform, also known as backprojection, utilises the data acquisitions from multiple images in order to reconstruct a 3D map. Backprojection projects the data back over the FOV to create a map of overlaying lines. For each angle of the detector, a set of projection data is acquired with the area where the greatest number of lines overlap indicating approximately from where the original signal was emitted. Figure 2.22 shows the data acquired for 4 sources at the centre of FOV from 8 angles (profiles of the measured counts for the 8 angular positions are shown). A basic reconstruction is shown in Figure 2.23 where the 4 sources can be roughly determined at the centre of FOV. Naturally, real studies have a greater number of projection angles and hence better resolution.

Backprojection is not an ideal reconstruction technique as it can leave undesirable streak artefacts in the reconstructed image as seen in Figure 2.24. In order to reduce the image flaws, certain processing techniques can be utilised, namely filtering. Filtering occurs in the spatial or frequency domain and can be used to selectively remove undesirable elements within the reconstructed image. In the quantification of PET scanners, a ramp filter with a cutoff at the Nyquist frequency (highest frequency component present) is recommended [44]. This ensures identical image reconstructions resulting in a fair comparison between the performance of different types of scanners.

Figure 2.25 shows: (a) a phantom; (b) a reconstruction without filtering; (c) the

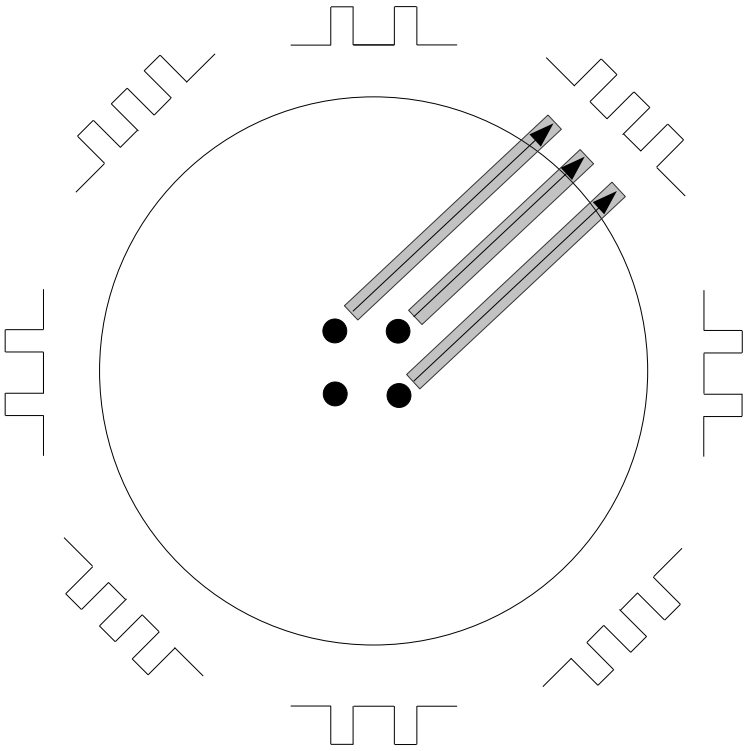

Figure 2.22: Forward projection showing the profiles of the aquired data from 8 separate angles

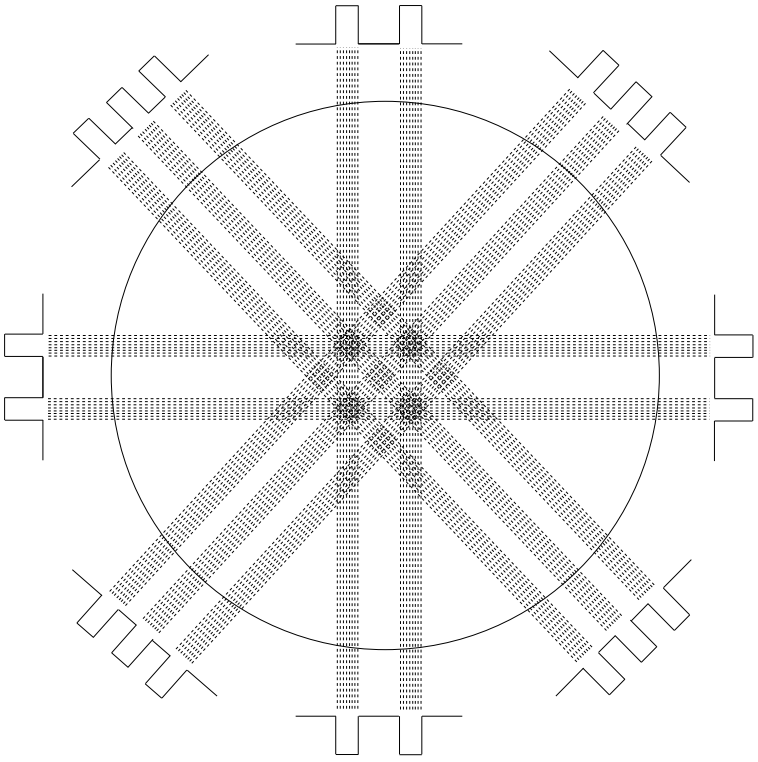

Figure 2.23: Back projection of the data shown in Figure 2.22

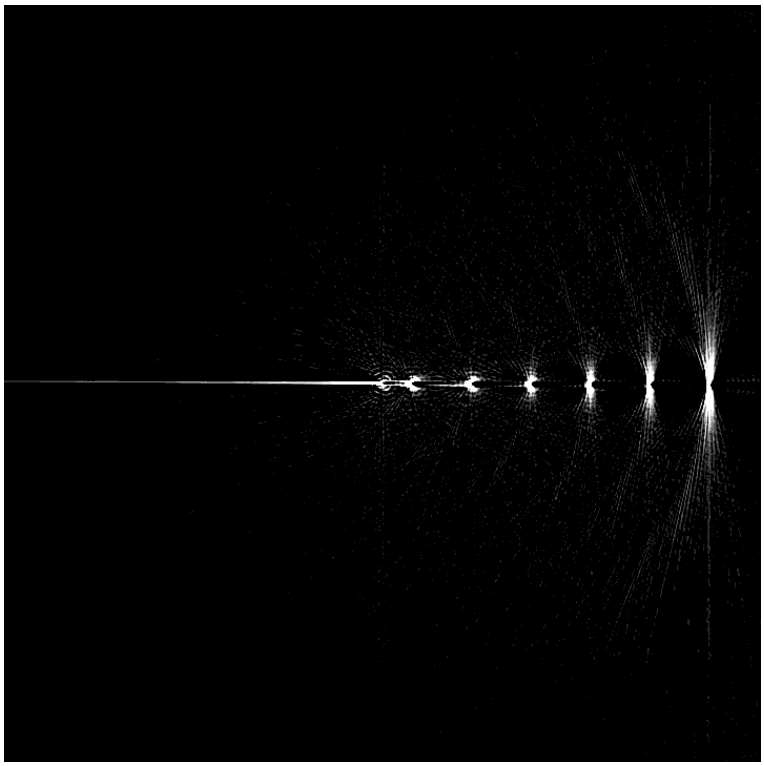

Figure 2.24: Streak artefacts in FBP image reconstruction of a number of point sources

frequency response of a normalised ramp filter and (d) the reconstruction after filtering with the ramp filter. The ramp filter reduces the low frequencies while allowing high frequencies to pass, demonstrating a linearly increasing response from low to high frequencies. This ensures that the low spatial frequency "haze" (blurring) is reduced while allowing high spatial frequency edges and boundaries to remain visible. Another type of filter which can be used is known as a modified ramp filter. A modified ramp filter is simply a ramp filter which has a rectangular window function applied to the ramp filter. That is, the window function only allows the ramp function to exist within the window, and sets the transmission of the filter to zero outside of this window above the Nyquist frequency. The modified ramp filters operate identically to the ramp filters in the area of removing the low frequency blurring however are superior in their ability to suppress noise above the Nyquist frequency.

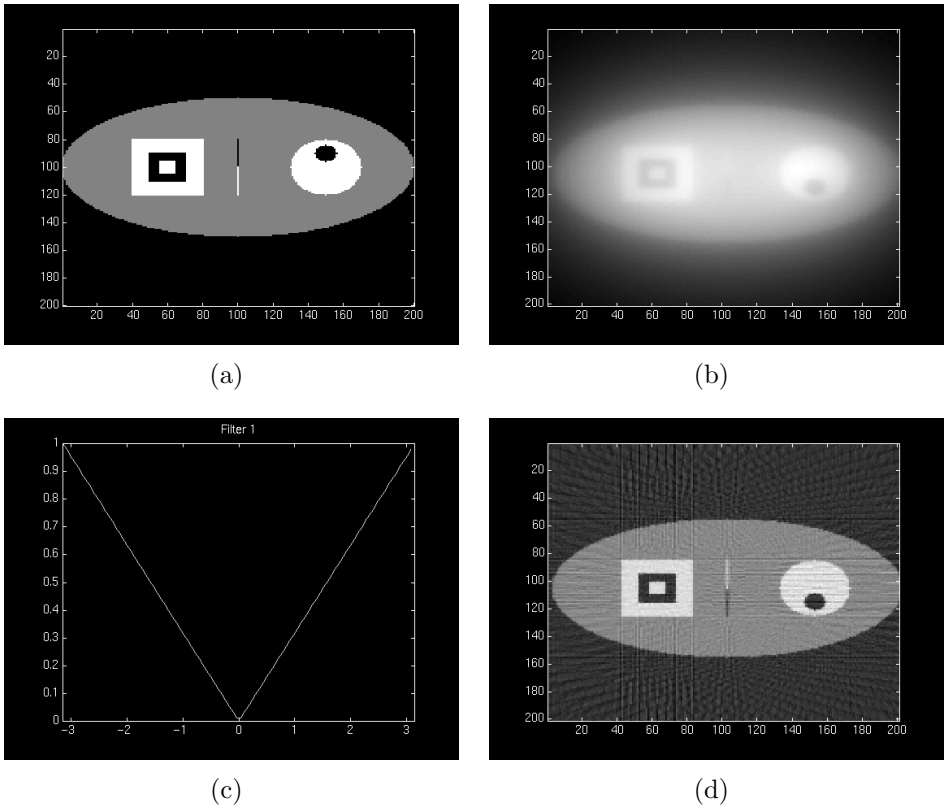


(a) (b)

(c) (d)

Figure 2.25: (a) a phantom; (b) a reconstruction without filtering; (c) the frequency response of a normalised ramp filter and (d) the reconstruction after filtering with the ramp filter [9]

Other filters such as the Butterworth, Shepp-Logan and Hann have more complex responses, however undertake the same purpose. It is possible to reduce the effect of the streaking in the reconstruction by intelligently choosing the filter type and its parameters. This may become a challenging process as it may be necessary to know the nature of the image being reconstructed before filtering.

### 2.12.2 Iterative Reconstruction

Iterative reconstructions start with an assumed or "prior" image. Generally this prior is selected as an entirely middle grey image. A forward projected prior is mathematically compared to the backprojected sinogram, and the result becomes the new prior for the next iteration of the reconstruction. Figure 2.26 illustrates

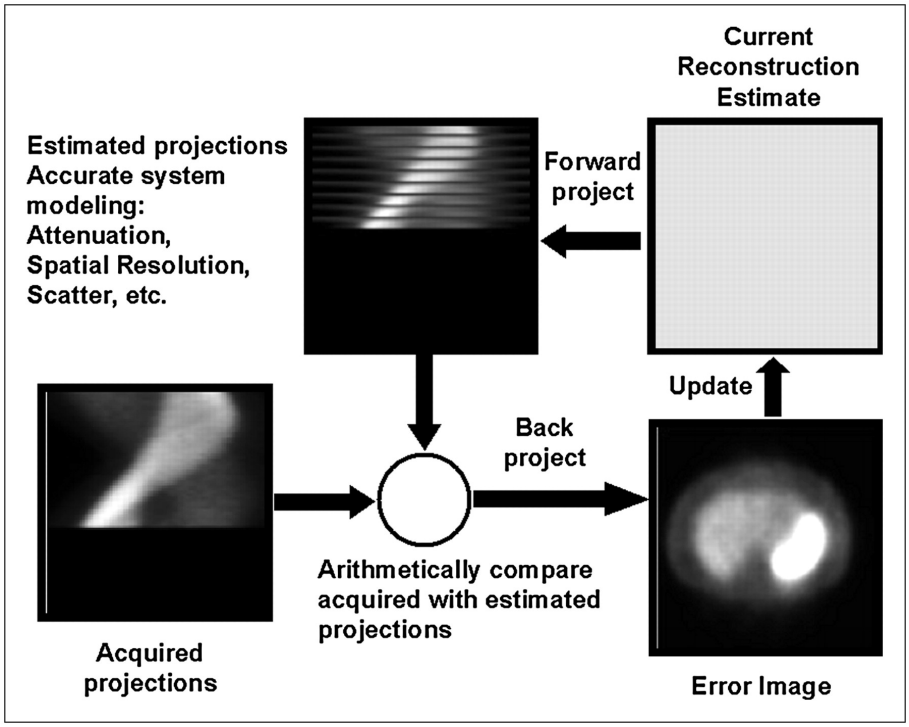


Figure 2.26: The schematic of the iterative image reconstruction process [10]

this process.

Iterative reconstruction allows the emission and detection process to be accurately modelled by considering factors such as attenuation correction, scatter and the spatial resolution of the system. While iterative reconstruction can produce images which are less sensitive to noise as well as reducing the traditional streaking artefacts of FBP, they can be computationally expensive as the convergence of the algorithm is slow and requires a significant number of iterations [45]. Figure 2.27 shows a comparison between an iterative technique and FBP [45]. As the number of counts contained within the study decreases, the FBP technique displays significant streaking, and at low counts, the final image becomes virtually unusable.

## 2.13 Conclusion

Limits on the resolution of small animal PET scanners exist as a result of the lack of DOI information available. Other factors such as positron range and Compton

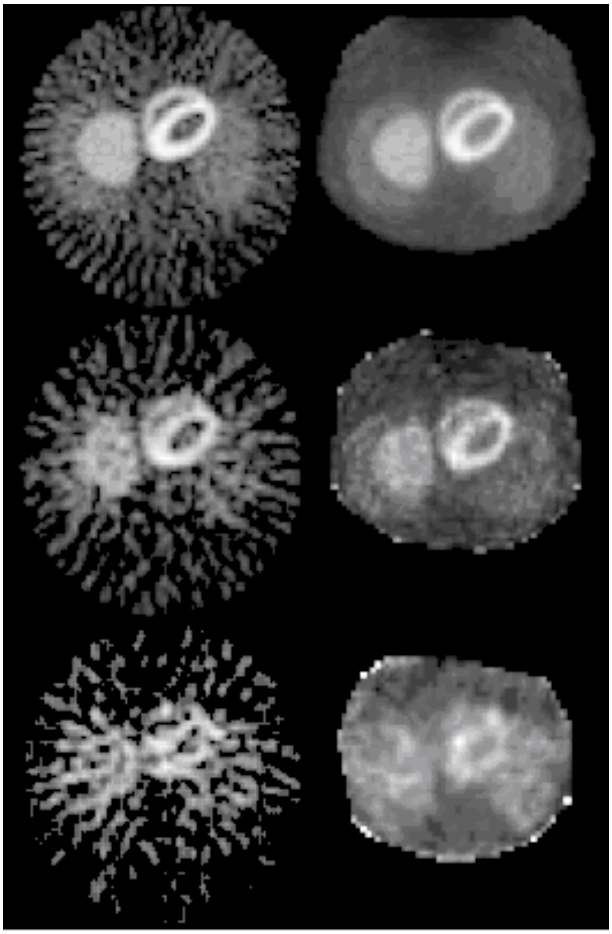

Figure 2.27: FBP (left) versus iterative reconstruction (right) for three different data sets containing 305000 counts (top), 29000 counts (middle), 10000 counts (bottom)

scatter add intrinsic limitations on the resolution, suggesting any improvement that can be made to eliminate factors such as the radial elongation artefact must be undertaken. Furthermore, it is vital to retain the sensitivity of the scanner at the same time as acquiring DOI information.

A number of detector modules have been presented, all specifically designed for DOI applications. While the literature about these detector modules is extensive and supports advancement in DOI measurement, they all rely on PMTs as a form of photodetection. As outlined previously, PMTs are bulky, expensive and require high voltage power supplies, making them unsuitable for large scale bulk production and utilisation. A method of one-to-one coupling of the scintillator crystal to smaller and cheaper photodetectors is required, a proposal outlined in more detail in the following chapter.

# CHAPTER 3

# MONTE CARLO SIMULATIONS

## 3.1 Introduction

The depth of interaction error is a significant limitation for PET scanners as it significantly compromises the resolution at the edges of FOV. The novel detector module proposed for this study provides depth of interaction information, however the benefit of this information remains unquantified. A method of simulating the multi-layered detector module and analysing the data from it needed to be developed in order to objectively illustrate its capabilities. This chapter discusses the methodology of the Monte Carlo method.

At present, the detector modules are prototypes and only 4 modules exist in prefabricated form. Significant optimisation of numerous aspects including geometric characteristics and electronic processing systems is required prior to large scale production. Section 3.2 and 3.3 discuss the detector module and the Monte Carlo simulation parameters during the optimisation process respectively.

## 3.2 Novel Detector Module

The module being developed has been designed to maximise its flexibility for easy module coupling so as to form a complete, customised, detection module that can be used in PET scanners dedicated to human brain and breast, and small animal studies. The proposed design contains an $8 \times 8$ array of optically isolated $3 \times 3 \times 3$ mm$^3$ LYSO crystals individually coupled to individual elements of an $8 \times 8$ Si photodetector array. However, the process of optimisation of the detector module requires testing of other crystal sizes and arrangements with the $3 \times 3 \times 3$ mm$^3$

crystals used as a starting reference point.

Considerations when selecting this scintillator included density, equivalent atomic number, stopping power, light output and energy resolution [46]. The new module is planned to be simple and robust, minimising module assembly complications and will be completely independent of photomultiplier tubes. It is designed with production line manufacturing in mind with each module assembled using a fully automated system with little or no labour involved. This process will include all passive elements, application specific integrated circuits (ASICs), detectors, wire-bonding of ASIC to detector and scintillator mounting.

The independent coupling of LYSO crystal and photodetector ensures depth of interaction information while maintaining the radial sensitivity of more traditional $24 \times 3 \times 3$ mm$^3$ crystals used in some present PET detectors. The 300 $\mu$m thick photodetectors are mounted on a 100 $\mu$m Kapton carrier and a 100 $\mu$m thick layer of optical paint is placed on the surface of the LYSO modules to prevent light escape thus making the detector module $3.5 \times 24 \times 24$ mm$^3$ in size. The space taken up by the photodetectors, Kapton carrier and optical paint are effectively "dead space" as they do not provide any actual imaging capability. A schematic of the proposed detector is shown in Figure 3.1.

### 3.2.1 LYSO Scintillator

Cerium doped Lutetium Yttrium Oxyorthosilicate (LYSO) is the scintillator used in the detector module. As outlined in Section 2.6.2, it has a high effective atomic number of 65 and a fast decay time of 42 ns, resulting in the capability to have high sensitivity and excellent timing resolution with low dead time [16].

The development of the detector electronics relies heavily on the choice of scintillator material, and at present significant characterisation studies are being undertaken at the CMRP. A number of suitable photodetectors for use in the detector

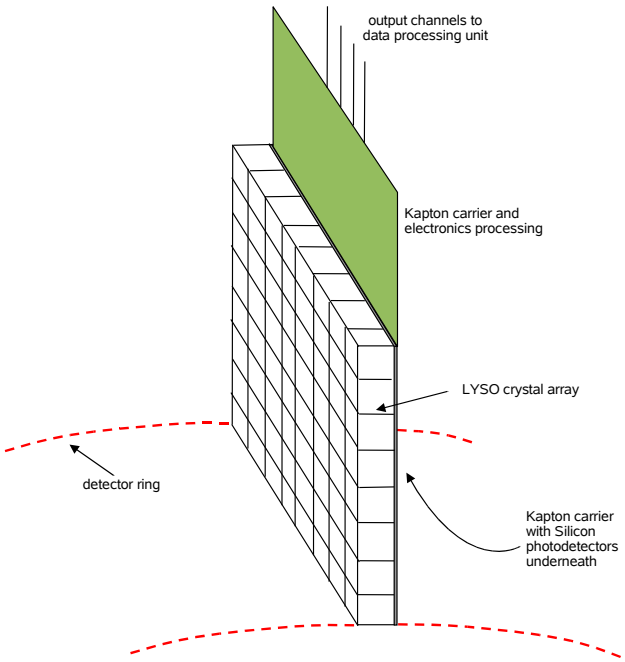


Figure 3.1: A schematic of a single module

module have been studied including p-intrinsic-n photodiodes (PINs), Silicon Photomultipliers (SiPMs), Avalanche Photodiodes (APDs) and Si photodiodes with the PIN providing promising results indicating it may be suitable for use in this application [47].

## 3.3 GATE Monte Carlo Simulations

### 3.3.1 GATE

GATE (**G**eant **A**pplication for **T**omographic **E**mission) was selected as the Monte Carlo simulation package for this study. As stated in Section 2.10.3, GATE utilises the Geant4 particle transport engine, the gold standard in Monte Carlo simulations. GATE is designed specifically for PET and SPECT as it has the ability to specify complex cylindrical co-ordinate geometries extremely easily, as well as specification of unusual scintillator crystal and detector structures. This makes it a far more suitable package for this study than other packages previously used for

PET studies such as SimSET [48], EGS4 [49] and MCNP [50].

GATE utilises a macro scripting language to replace the complex C++ coding requirements of Geant4. The macro scripting language has elements defining various features of the simulation with a detailed description of each element discussed in the next section. The GATE scripting is utilised in Geant4 to build the detector geometry, undertake the simulations with the prescribed parameters and finally output the data in the required format, all transparently to the user.

### 3.3.2 The World Volume

The world volume is specified as a large cube with sides 400 mm long. This volume is made up of air and made only slightly larger than the scanner diameter of 300 mm in order to prevent wastage of time involved with simulating photons headed away from the scanner and out of the world volume which have no effect on the simulation results.

The position in the world volume is defined according to cartesian coordinate system in the x, y and z directions as shown in Figure 3.2 in red, green and blue respectively.

Other references to radial, tangential and axial directions are made in this study as shown in Figure 3.3. These quantities in red, green and blue are shown respectively within the same detector ring.

### 3.3.3 Scanner Geometry

GATE features a function known as the scanner "system" which is the key to GATE and its operation. A system specifies a general template for a given scanner, a useful feature as numerous types of scanners share a general geometric specification. Each system contains a tree-like hierarchical structure, with each level of the tree having a given function within the geometry. The scanner system used in this study is the "cylindricalPET" system which consists of the top level structure,

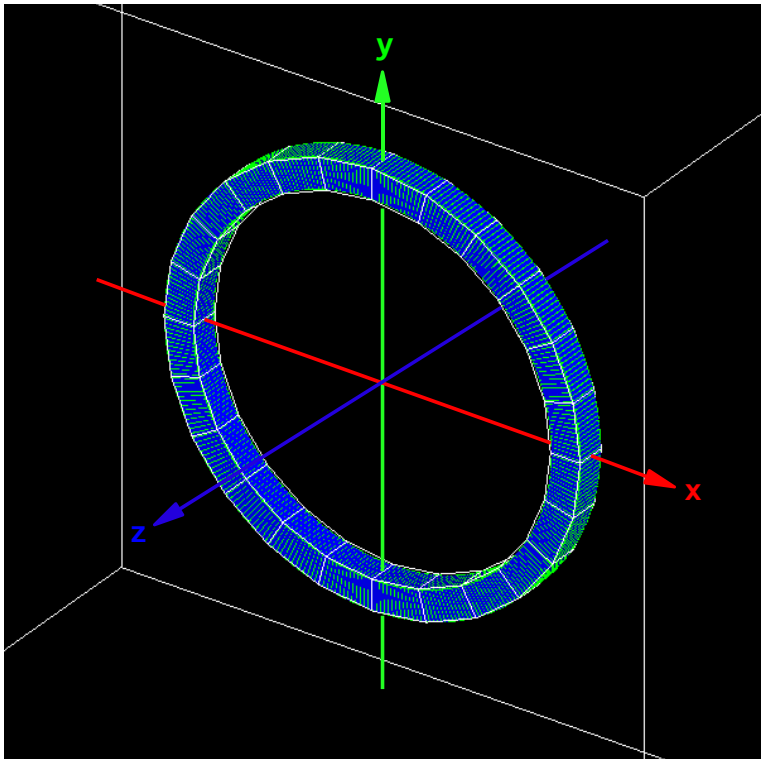


Figure 3.2: The cartesian coordinate system as defined by GATE. The red, green and blue axes represent the x, y and z directions respectively

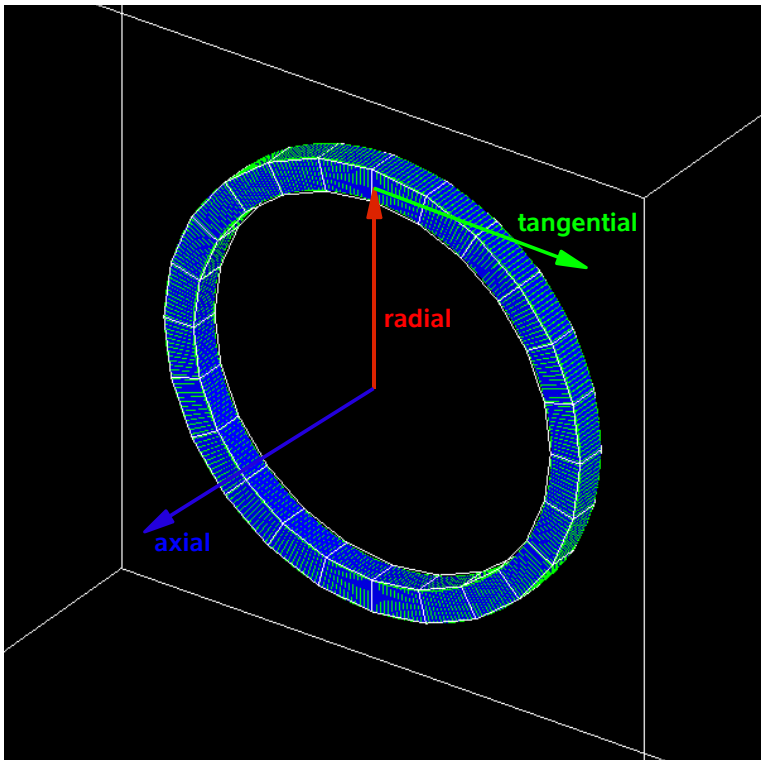


Figure 3.3: The radial, tangential and axial directions represented in red, green and blue respectively

the "rsector", with smaller volumes placed inside. The rsector is analogous to a single detector module unit in a scanner. The rsector contains within it modules, submodules, crystals and crystal layers, each being a level lower in the hierarchy than the previous volume unit. A given volume unit can be repeated inside its parent module as long as it remains within the confines of the parent volume. Other types of systems such as "scanner", "SPECThead", "ecat" and "CPET" can be specified for other geometry families [11].

As the original proposal for the detector module is an $8 \times 8$ array of $3 \times 3 \times 3$ mm$^3$ LYSO crystal, the rsector is a $24 \times 24 \times 3$ mm$^3$ box made of air filled with the crystals. The 3 mm wide detector module allows a total of 314 modules to be placed around the detector scanner if the dead space associated with the detector electronics is ignored. When the extra 500 $\mu$m of dead space from the optical paint, photodetectors and Kapton carrier is considered, a total of 268 detector modules can be placed around the ring. A GATE visualisation of an rsector containing an $8 \times 8$ array of crystals is shown in Figure 3.4.

Parameters such as the crystal size and the arrangement of the crystals and detector modules are systematically varied to determine the optimal arrangement with greater detail provided in Chapter 6.

### 3.3.4 The Sources

GATE allows users to select either ions, positrons or gammas as the primary source. The ion type can be specified by the atomic number, atomic weight and ionic charge and excitation energy. The main sources used in this study are positrons and gammas. The positron annihilation naturally requires a phantom to exist around the sources otherwise the positrons escape the world volume and faults can occur in the simulation.

Positrons, like electrons, interact with other particles and require a far greater number of interactions than photons before they deposit all of their energy and

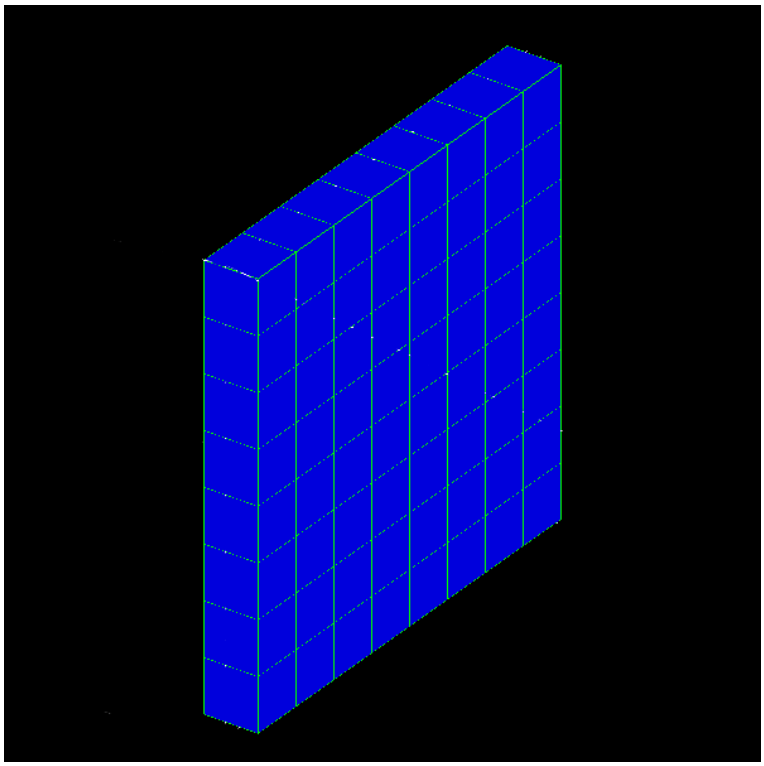

Figure 3.4: An rsector with an $8 \times 8$ array of crystals inside

significant time can be saved by not simulating electron and positron transport. This is achieved by removing the positron entirely from the simulation and using two back-to-back $\gamma$ photons as the starting point. That is, instead of modelling the positron emission from the source, the source itself is assumed to directly emit the two back-to-back annihilation photons. The use of back-to-back photons increases simulation speed at the expense of accuracy as the positron range is neglected (however, GATE allows the positron range to be incorporated into back-to-back $\gamma$ simulations for greater accuracy). Simulations comparing the positron emission and back-to-back $\gamma$ photons are considered in Chapter 6.

In experimental studies, the annihilation photons have an isotropic distribution within the phantom. A major factor reducing the sensitivity of a PET scanner is the number of photons generated within the phantom which propagate in a direction away from the detector crystals and out of the world volume. These photons are "wasted" as they do not provide any information to the scan while utilising

simulation time. This further enhances the need for a large number of crystal rings to maximise the solid angle of detector visible to the emission. Further time saving and increase in sensitivity can be obtained by emitting back-to-back photons within a specified solid angle having photons projected in the direction directly towards the scintillator crystal. By reducing the solid angle of emission to match the apparent width of the detector crystal, fewer photons which do not contribute to the useful scan data require transporting, hence an increase in the speed of the simulation [11].

The sources used in this study are small spherical sources with a radius 0.001 mm placed at various positions across the FOV. These sources are intended to emulate point sources. A source is placed at the centre (0 mm), 10 mm, 30 mm, 50 mm, 70 mm, 90 mm and 110 mm across the FOV. In positron emitting studies, the spectrum of emission was set to match that of Fluorine-18, the most commonly used PET radioisotope.

### 3.3.5 The Phantom

As with experimental PET studies, GATE allows complicated phantoms to be described and placed within the FOV. When simulating positron sources, the phantom is essential in order to provide a medium for the positrons to annihilate. Most studies using a PET scanner involve human or animal subjects with a water phantom being the simplest approximation of tissue and muscle.

The phantoms used in this study are large cylinders typically filling up most of the FOV.As the sources were isotropic for positron studies, a large volume ensures that a significant scatter contributions from sources is recorded. The phantom is not placed on a bed as would be required in an experimental study. Introducing the bed can create further scatter contribution to the data acquisition.

### 3.3.6 The Sensitive Volumes

Once the basic parameters of the scanner and the phantom are defined, GATE requires the user to specify sensitive detectors. These volumes refer to those in which all interactions between particles are recorded, with each interaction known as a "hit". Hits store large amounts of information about each interaction including energy deposition, type of particle, size of the previous step in the transport, position of interaction and time of interaction as well as a range of other selectable parameters. Figure 3.5 is reproduced from the GATE Manual and shows some of the terminology used in recording of hits in a sensitive volume placed in water.

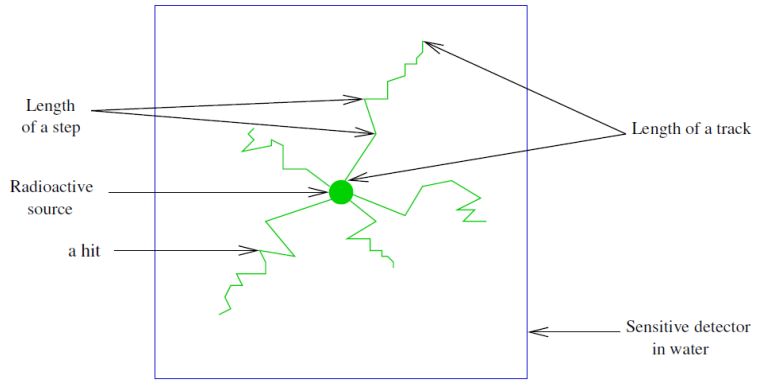


Figure 3.5: Particle interactions in a sensitive detector [11]

The phantom placed inside the field of view can also be declared as a sensitive volume. This allows the program to determine whether a photon that has reached the detector has been scattered inside the phantom and contributes to a real or a random coincidence. The information gathered using this process is not readily achievable in an experimental study as interactions within a phantom cannot be measured however other techniques can provide the same information. Using a transmission source on one side of the scanner can allow scatter and attenuation correction images to be acquired, effectively providing the same information as the phantom sensitive detector volume data. This scatter and attenuation correction

data is mathematically incorporated into the acquired PET data to create a more accurate reconstruction.

### 3.3.7 Physics Processes

A main limitation of Monte Carlo studies is that they only provide an approximate solution. The accuracy of the study depends on a number of parameters, the most important being the number of primary particles. Increasing the number of primary particles results in more accurate solutions due to improved statistical sampling, at the expense of increased simulation time. A number of techniques can be used to reduce the simulation time, while retaining accuracy.

The transportation of electrons is a significantly time consuming element when simulating electrons and positrons. In all Monte Carlo packages, it is possible to set energy cut-off values which force the particle to deposit the remainder of its energy when it reaches the cut-off energy. The electrons in this study have not been modelled (ie. their energy cut-off is set to 1 m, resulting in all electrons which have a range less than 1 m not being transported). Setting high energy cut-off values can compromise results as the range of electrons within water for this study is on the sub-millimetre scale. However, this approximation was essential as not doing so would result in simulation times becoming prohibitive with the computing resources available.

Other variance reduction techniques were not available at the time the studies in this thesis were undertaken however recently released versions of GATE incorporate limited methods.

### 3.3.8 Data Acquisition

GATE has a sophisticated processing technique to simulate the behaviour of a detector within a scanner and the signal processing chain from this detector known as the “digitiser module”. This module uses a number of complex algorithms to

model numerous processes including the summation of light inside a crystal, energy response of the detector, energy thresholds and dead times. Each crystal specified in the detector module is considered independent and as the smallest sensitive volume defined. In the event of multiple "hits" occurring inside a given crystal element, their individual energy depositions are added. Once a particle has interacted with a sensitive detector volume, the digitiser module processes the data until it reaches a form similar to what would be the output from the Front End Electronics (FEE). The FEE takes in the "hit" information, and outputs information corresponding to physical information observed from a real scanner such as the position of interaction (ie. the detector IDs), energy deposited in the smallest defined subvolume and time. This new data is stored in a set of data known as "singles". A secondary stage of processing to sort coincidences can be carried out if desired by taking the singles and passing through a coincidence timing window into a new data set called "coincidences". The actual modelling of the electronics has been extremely simplified within these studies, with actual PET scanner pulse analysis being a far more complex process.

The energy response of a sensitive volume in a Monte Carlo study is assumed to be ideal; that is, the exact amount of energy deposited in a crystal is known. This is often not the case and a gaussian distribution for the measured energy exists. The 511 keV photopeak in this study is blurred to a gaussian distribution of 26% FWHM.

### 3.3.9 Data Output

GATE allows two different types of data outputs, namely:

- Standard outputs: ASCII, ROOT
- System dependent outputs: LMF (List Mode Format), sinogram and ecat7, Interfile

The standard outputs are fully customisable to select only the output parameters required and are available for all GATE system geometries. The system dependent outputs, as their name suggests, are only available when certain system types with certain geometric properties are used. These outputs are not customisable and often require other 3rd party software processing in order to analyse. Originally, a number of the system dependent output modes were selected but data analysis was not readily achievable. The design of the novel detector module necessitated a customised way of processing the data therefore the ASCII output format was selected in order to provide the greatest flexibility for post processing.

GATE records a large number of parameters for each coincidence and allows users to select only the data they require using a "data output mask". That is, by using a series of 1s and 0s in the data output specification file, a user can specify if they want a certain parameter to be put into the data output file. The following data was selected to be sent to the data output files from the simulations:

- time stamp of interaction
- energy deposited
- x, y, z position of interaction in world reference
- volume IDs of interaction (rsectorID, moduleID, submoduleID, crystalID, layerID)
- number of Compton interactions in the phantom before reaching the detector
- number of Compton interactions in detectors before reaching the detector
- scanner angular position.

This data was recorded for each event within the coincidence (known as a "single") with each line containing both singles in the coincidence and a new line separating each coincidence in the final data output file. Other parameters which can

be recorded by GATE are outlined in the GATE User Manual [11].

### 3.3.10 Simulation Time and High Performance Computing Grid

GATE simulations are often extremely slow as there are large numbers of sensitive volumes through which radiation is transported. Furthermore, PET studies have extremely low sensitivity, meaning a large number of primary photons need to be simulated in order to achieve significant statistical accuracy within the study. Variance reduction techniques that increase simulation speeds have been introduced in the latest version of GATE (version 4.0) however none were available in the older versions of GATE, the platform on which these simulations were undertaken.

Simulations using a single computer proved to be extremely slow and often numerous compromises were made in relation to the statistical sampling in order to have reasonable simulation times. The simulation time in all simulations was set to 360 seconds. For an 8 axial ring detector (1 detector module), a simulation takes approximately 2 weeks of real time on a single core processor, and demonstrate a poor signal to noise ratio. Hence, a solution requiring multiple simulation threads was required. The Centre for Medical Radiation Physics has invested in the development of a High Performance Computing Grid in order to provide access to undertake Monte Carlo simulations. This cluster presently consists of 50 nodes (11× Pentium D 3.2GHz with 2GB RAM, 7× Pentium Quad Core 2.4GHz with 2GB). As there is significant queuing, 8 nodes are made available to a user at a given time. For GATE studies, 8 identical simulations with different random seeds were run simultaneously with data combined once all simulations were completed. Later versions of GATE released during the final stages of this study support cluster based simulations, however are only able to output data in ROOT format. As ASCII data was required for this study, manual splitting of simulations and recombination of data was required before analysis.

# CHAPTER 4

# SINOGRAM BINNING APPLICATION

## 4.1 Introduction

The sinogram binning application developed for this study is extremely flexible and able to adapt to nearly all data sets provided by the "cylindricalPET" family of scanners in GATE. It utilises user input on the geometry of the scanner and data from the output file to create a sinogram from the Monte Carlo data. Sinograms have been traditionally used with single layer detector systems, yet limited studies have documented the use of sinograms for systems with depth of interaction [51]. The sinogram constructed in this study is represented using a 3D array, the first two dimensions representing the radial position of the Line of Response (LOR) and the angle of the LOR, whereas the final dimension represents the slice of the image that the LOR is binned into.

The application is split into a number of smaller functions: the user input stage, the reading in of coincidence data from the Monte Carlo output files, the calculation of the LOR for the sinogram and finally the data output stage. The sinogram binning application underwent several revisions, starting at version 1.0 and going up to version 1.4, with version 1.3 and 1.4 used extensively in the processing of the data presented in study. There are a number of areas that can be developed further within this application which are discussed in Chapter 7.

The main purpose of the sinogram binning application is to determine the LORs from the coincidence data. For a given coincidence, it carries out the following:

- reads in the detector IDs of each "single" in the coincidence
- calculates the position of each "single" in the world referential volume

- determines the equation of the LOR in the cartesian coordinate system using each of the 2 singles recorded per coincidence
- determines the radial distance of the LOR from the centre of FOV and the angle the LOR makes with a predetermined fixed reference as well as the axial slice the LOR is binned into
- increments the element of the sinogram represented by the LOR
- writes sinogram data out to file.

A summary of each main function within the application is provided in the following sections.

## 4.2 User Input

The sinogram binning application is extremely flexible, able to handle data from any scanner of the "cylindricalPET" system specified in GATE. The user is required to specify the following:

- ring radius
- the number of rsectors in the ring
- the crystal size
- the depth of the detector module in the radial direction
- whether there are multiple detector modules in axial direction of the scanner. If so, the following information must also be provided:
  - the number of detector modules placed axially
  - whether coincidences between different detector modules can be accepted and if so, the maximum ring span
- the number of crystals in the axial direction of a module

- the number of crystals in the tangential direction of a module
- the number of crystals in the radial direction of a module (ie. the number of depth of interaction layers)
- the energy window thresholds (in MeV).

There are also a number of other parameters which the user is required to specify including:

- method of position calculation (Section 4.9.5)
- upsampling factor (Section 4.7)
- whether the gantry is rotating
- whether there is Compton scatter information in the simulation data
- whether there is information on the positron annihilation positions in the simulation data (not physically obtainable data)

These parameters are used to determine what information is present in the data output file. If parameters are entered incorrectly by the user, errors can occur when reading in the data as well as in the sinogram binning process which can result in segmentation faults or incorrect sinograms.

## 4.3 Reading in Data

The data from the simulations is stored in numerous large ASCII data files. The Monte Carlo simulation continuously writes data out into these data files, storing various selected parameters for each "single" detected within a coincidence. The single line in the output data file holds information about both singles within the coincidence. A typical single line of data (although presented as two) from an output file is shown below.

7.65540223966124333543348e+00 | 5.209e-01 | 1.052e+02 -1.321e+02 4.503e+00 | 0 269 0 0 46 0 | 0 | 1 | 3.825e-01

7.65540223941802544516122e+00 | 4.544e-01 | -1.372e+02 9.270e+01 -5.692e+00 | 0 127 0 0 21 0 | 0 | 2 | 3.825e-01

A detailed description of each element in the data from the first line above is provided below. The second line contains the same information, however for the second "single" within the coincidence.

`7.65540223966124333543348e+00` : timestamp of 1st "single" (in seconds).

`5.209e-01` : energy deposited in the crystal by 1st "single" in MeV (after digitisation module has undertaken processing of individual hits and energy resolution blurring).

`1.052e+02 -1.321e+02 4.503e+00` : X, Y, Z positions in world volume of the interaction within the crystal sensitive volumes. This information is not accessable from a real scanner as it requires infinitesimally small volume elements for accurate determination. It is used to show the theoretical limits of performance for comparison (discussed in further detail in Section 4.9.5).

`0 269 0 0 46 0` : the detector IDs as specified by GATE. From first to last, each number represents the ID of the volume attached to the "base" level of the system, the rsector, the module, the submodule, the crystal and layer. Since only rsectors and crystals are defined in the system geometry, all other numbers in the detector IDs are always zero. As all of the detector IDs are printed out in a group, it is not possible to output only the rsector and crystal IDs.

`0 1` : the number of Compton interactions in the phantom before reaching detector and the number of Compton interactions in detectors before reaching the detector respectively.

`3.825e-01` : the angular position of the gantry when that coincidence was measured (used for rotating gantry studies only).

## 4.4 LOR Calculation

The radial distance of the LOR from the origin and the angle it makes with the specified reference frame must be calculated in order to place the LOR into the sinogram (shown in Figure 4.1). The detector ID specified for each "single" provides the position of interaction accurate to the nearest crystal, as a real scanner's electronics modules would. The two positions from each coincidence are translated into cartesian coordinates in order to determine the LOR.

The reference frame used in the definition of the geometry is the same as that used in traditional quadrant definition (quadrant 1 is the top right quadrant, 2 is top left, 3 is bottom left and 4 is bottom right).

In order to calculate the LOR the cartesian coordinates of the position of interaction for each of the singles in the coincidence must be determined. A number of calculations using the user input specifying scanner geometry parameters and some trivial coordinate geometry is required. The following list outlines the calculations required to determine the cartesian coordinates of the crystal elements in which the

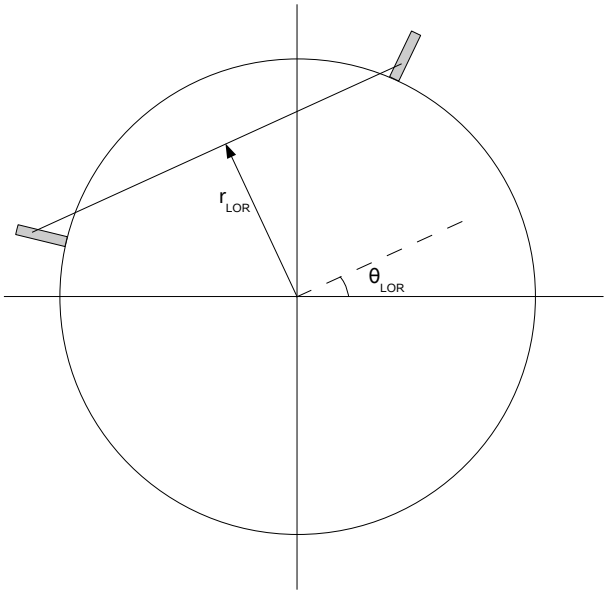


Figure 4.1: The radial distance of the LOR and the angle it makes with a fixed reference frame

coincidence is measured between. A more detailed analysis of these processes is given in the following sections:

- Determine the angles of the rsectors that each single is measured in
- Calculate the distances from the origin to the centre of the crystals in which each single is measured in
- Using the radial distance of the crystal and the angle of the rsector, calculate the x and y coordinates of each of the singles in the coincidence
- Using the crystalIDs and the SSRB, determine the axial position for the origin of the LOR.

## 4.5 Interaction Position Calculation

The angular position of the rsector with respect to the reference frame can be calculated using:

$$rsector\ angle = \frac{rsectorID}{number\ of\ rsectors} \times 360^o \tag{4.1}$$

When specifying the geometry of the scanner, GATE defines the crystalIDs inside an rsector as shown in Figure 4.2.

The radial distance from the centre of field of view to the crystal can be calculated by determining the depth at where the crystal is. This can be calculated according to:

$$\begin{aligned} radial\ distance\ \ = \ \ & ring\ radius + \\ & (crystalID)\ mod\ (number\ of\ layers) \times crystal\ size + \\ & \frac{1}{2} \times crystal\ size \end{aligned} \tag{4.2}$$

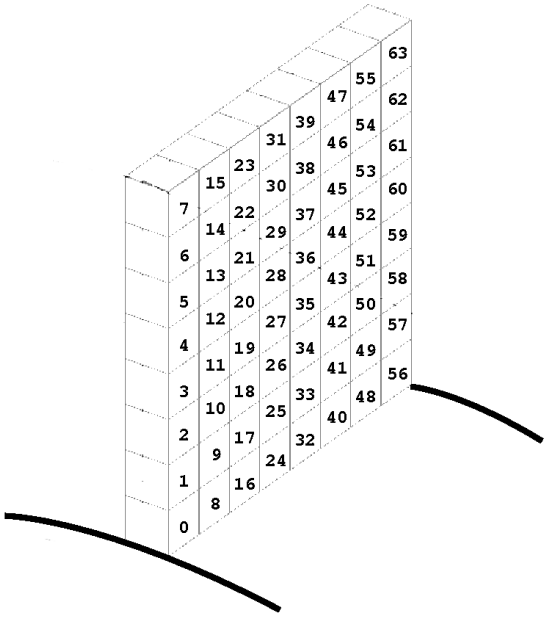


Figure 4.2: CrystalIDs within an rsector

A detector module showing eight $3 \times 3 \times 3$ mm$^3$ crystals in the axial and radial directions is shown in Figure 4.3 illustrating the crystalIDs and the axial position coordinates. The central point of the detector module in the axial direction is considered to be the axial central point.

The angle of the rsector and the radial distance of the crystals are used to determine the cartesian coordinates of the crystals as shown in Figure 4.4.

The x and y positions are calculated using:

$$x = radial\ distance\ \times cos\theta \tag{4.3}$$

$$y = radial\ distance\ \times sin\theta \tag{4.4}$$

As the quadrant specification follows a mathematical convention, the placement

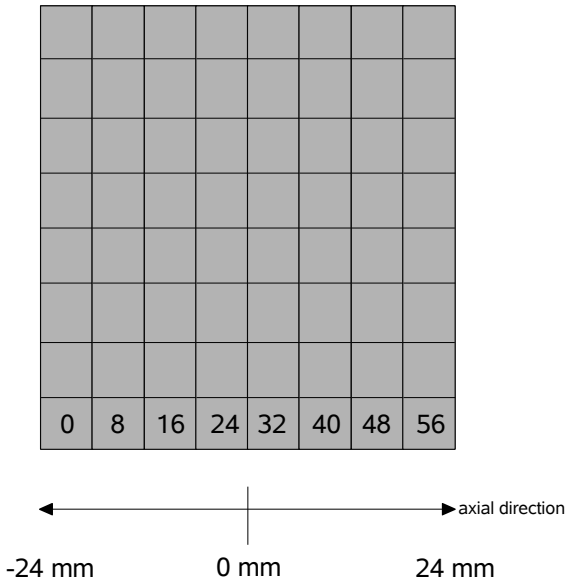


Figure 4.3: The axial positions of various crystals along a detector module containing 3mm crystals

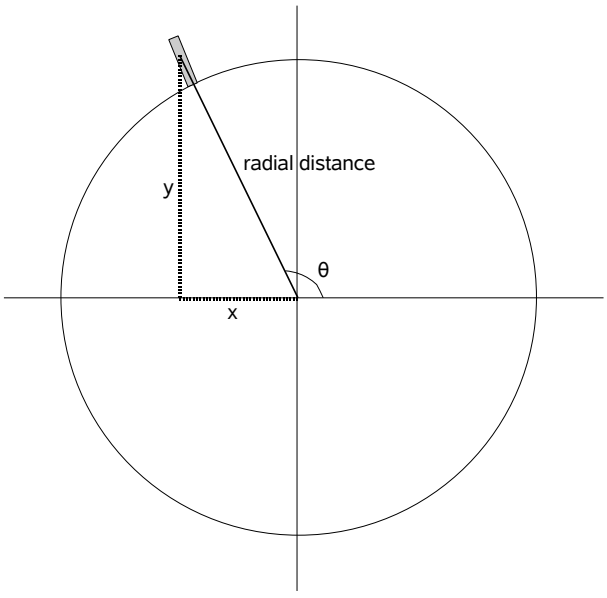


Figure 4.4: Using the angular position and radial distance to calculate the cartesian coordinates

on the negative or positive side of an axis is automatically taken care of by the trigonometric expressions in equations (4.3) and (4.4).

The axial origin of the LOR according to the SSRB can be calculated similarly using the crystalIDs according to:

$$\begin{aligned} axial\ position\ = \ & \Bigg\{ -\frac{crystals\ in\ axial\ direction}{2} + \\ & \frac{crystalID}{crystals\ in\ axial\ direction} | + \\ & \frac{1}{2} \Bigg\} \times crystal\ size \end{aligned} \tag{4.5}$$

Since the first column of pixels lies in the negative section of the axial plane, the distance from the centre of the rsector module to a position half a crystal width from the edge needs to be subtracted in order to provide the axial position in terms of the cartesian coordinate reference frame.

## 4.6 LOR Calculation

The radial distance ($r_{LOR}$) from the origin and angle ($\theta_{LOR}$) of the LOR are calculated using the cartesian coordinates of the crystals determined in the previous section as illustrated in Figure 4.5.

The angle of the LOR can be simply calculated using:

$$\theta_{LOR} = tan^{-1}(\frac{y_2 \ - \ y_1}{x_2 \ - \ x_1}) \tag{4.6}$$

The radial distance calculation requires the y-intercept of the LOR to be determined (illustrated in Figure 4.5). Utilising the two-point formula in coordinate geometry and the knowledge that x=0 at the y-intercept, the expression for the y-intercept becomes:

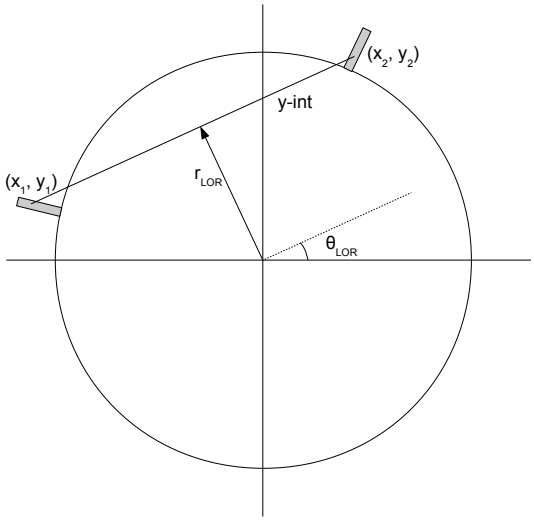


Figure 4.5: Calculation of LOR angle and radial distance

$$y_{int} = y_1 \ - \ x_1 \times \frac{y_2 \ - \ y_1}{x_2 \ - \ x_1} \tag{4.7}$$

The radial distance of the LOR from the centre of FOV then simply becomes:

$$r_{LOR} = |y_{int} \ \times \ cos\theta_{LOR}| \tag{4.8}$$

The average axial position is calculated using the SSRB algorithm described in detail in Section 2.11.3. Figure 4.6 shows the two axial positions at which the LOR is drawn between being averaged to specify the point at which the LOR is determined to originate from. The SSRB algorithm determines the axial position of the origin of the LOR as:

$$z_{average} = \frac{z_1 \ + \ z_2}{2} \tag{4.9}$$

The number of axial slices in the final reconstruction in this study was set to

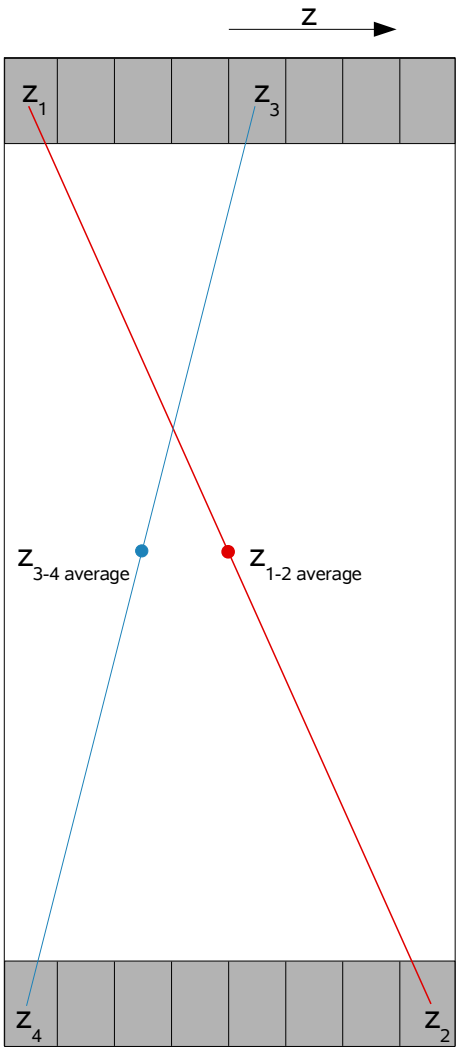


Figure 4.6: Calculation of source of the LOR in the axial direction

the same as the number of rings in the detector. That is, if there are 8 crystals in a single detector module along the axial plane, 8 sinograms are produced and hence 8 independent reconstructed images. This choice was made, inititially to minimise the amount of data output from the sinogram binning application as traditional scanners employ 2N - 1 slices (where N represents the number of axial crystal modules). Increasing the number of slices in the final reconstruction to 2N - 1 slices is considered in Section 7.1.9.2.

The calculated average axial position for each LOR determines the slice of the

sinogram into which the LOR is placed using:

$$slice = round(\frac{z_{average} + \frac{crystal\ size}{2}}{crystal\ size}) + \frac{number\ of\ axial\ crystals}{2} \quad (4.10)$$

The values determined for $r_{LOR}$, $\theta_{LOR}$ and the slice are sent to the next step of the program, the sinogram binning stage.

## 4.7 Sinogram Binning

The size of the sinogram determines the output resolution of the reconstructed image. Often, the number of projection angles in a system restricts the dimensions of the sinogram which are generally equal to half the number of detector modules in the ring.

Placing interactions from multiple layers of crystal into a single sinogram effectively results in upsampling along the projection angle axis of the sinogram. That is, smaller angular increments are possible in the angular sampling as shown in Figure 4.7.

The angles of projection described by the lines at angles $\theta_1$ and $\theta_2$ in Figure 4.7 are adjacent angles of projection in a traditional scanner design. Depth of interaction data allows projection angles at values inbetween the existing projection angles expressed by lines at angles of $\theta_1 + \Delta_1$ and $\theta_1 + \Delta_2$ (and all other unlabelled lines between the existing projection angles $\theta_1$ and $\theta_2$) effectively allowing smaller increments in the projection angle. These additional projection angles result in an increased number of pixels in the constructed sinogram leading to increased sampling. If there are significant LORs within the new projection angles, an increase in the resolving power may be observed, as well as a reduction in the radial elongation artefact. However, the improvement is negligible at positions where LORs

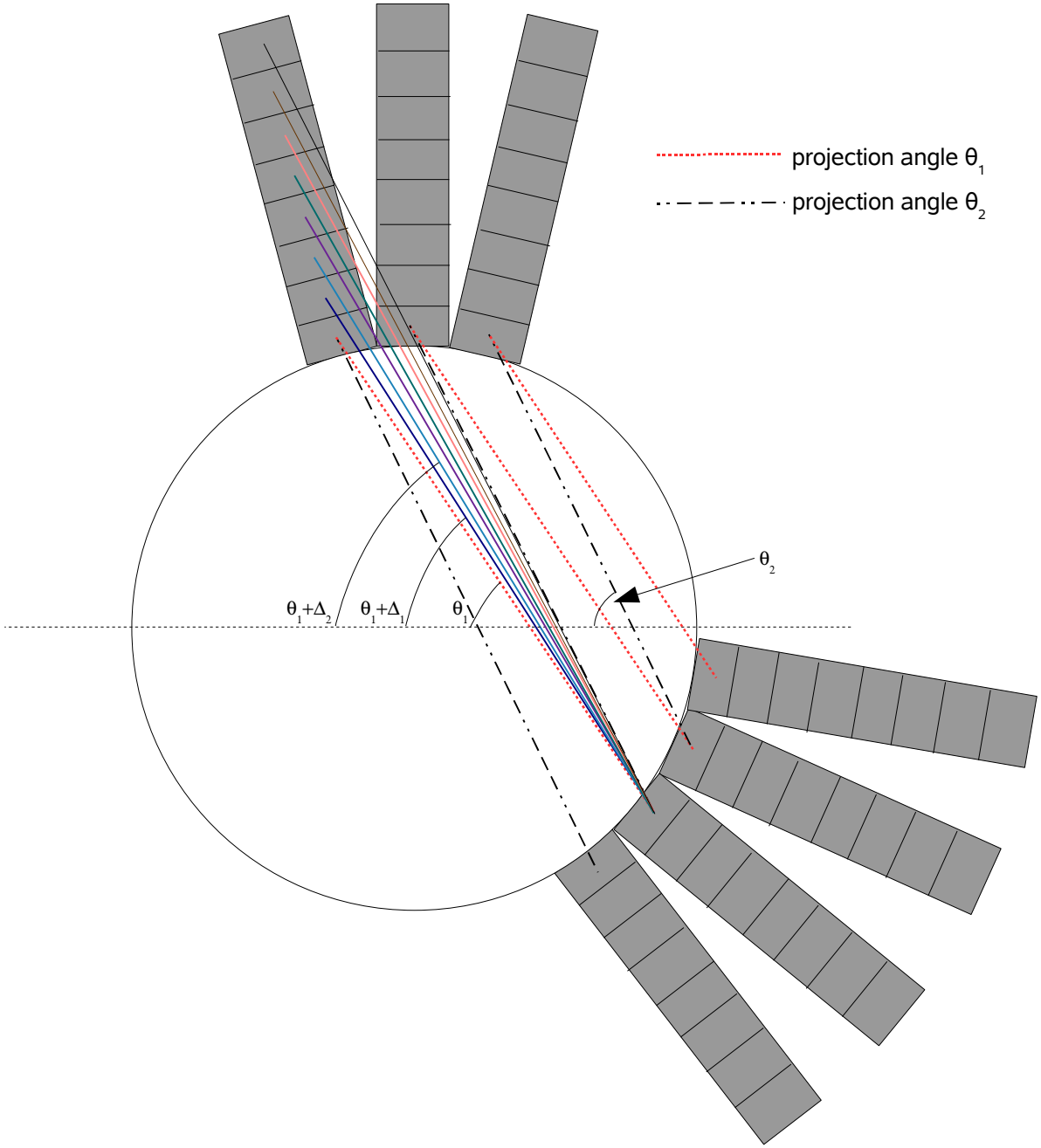


Figure 4.7: The upsampling effect due to DOI information data being available from a detector module (not to scale)

are normally (or close to normally) incident on the crystals as the depth of interaction provides no additional information than what is available from a single layer of crystal. These "zero efficiency" bins are confirmed in [51].

Having 8 layers of crystal does not necessarily provide 8 times upsampling due

to degenerate LORs. That is, certain LORs from deeper level crystals have radial distances and angles similar or identical to LORs already commencing from adjacent detector modules. This also results in zero efficiency bins within the sinogram and methods such as rotating the gantry are required to create greater angular sampling [52], a technique which has been incorporated in the current studies.

The "upsampling factor" provided by the user is a measure of the dimensions of the sinogram. As the upsampling factor increases, the dimensions of the sinogram also increases allowing smaller angular and radial increments between adjacent sinogram elements. By default, the upsampling factor is set to 1 providing the same resolution as in a monolithic scintillator crystal system. Higher upsampling factors allow LORs originating from deeper level crystals with slightly different radial distances and angles to be accepted and subsequently recorded as unique data.

The number of array elements in the sinogram increases with the square of the upsampling factor. The "real space" inside the FOV is therefore being represented by increasingly smaller pixels in the sinogram. Hence, a scaling factor between real dimensions (as $r_{LOR}$ and $\theta_{LOR}$ are) and sinogram pixels representing $r_{LOR}$ and $\theta_{LOR}$ exists within the code. This factor is defined by:

$$r_{LOR\ pixels} = \frac{r_{LOR}}{radial\ scaling\ factor} \tag{4.11}$$

$$\theta_{LOR\ pixels} = \frac{\theta_{LOR}}{angular\ scaling\ factor} \tag{4.12}$$

The radial and angular scaling factors relate to the real dimensions of the detector geometry. In this instance, the radial size of the detector geometry is approximately 350 mm (300 mm ring diameter and two 24 mm deep scintillator units on either side of the ring), and the angular scaling for the sinogram considers LORs which are up to $180^o$ apart from each other. The radial and angular scaling factors

are described by:

$$radial\ scaling\ factor = 350 \div number\ of\ radial\ bins\ in\ sinogram \tag{4.13}$$

$$angular\ scaling\ factor = 180 \div number\ of\ angular\ bins\ in\ sinogram \tag{4.14}$$

The number of radial bins and angular bins as mentioned previously is determined by the number of detector modules present. However, the upsampling factor needs to be considered as well, and the number of radial and angular bins is scaled according to the upsampling factor based on:

$$number\ of\ radial\ bins = \frac{number\ of\ detector\ modules}{2} \times upsampling\ factor \tag{4.15}$$

$$number\ of\ angular\ bins = \frac{number\ of\ detector\ modules}{2} \times upsampling\ factor \tag{4.16}$$

The sinogram is defined in the progam as a 3 dimensional array, the first element representing the radial position of the LOR, the second being the angular position and the 3rd representing the axial slice.

```
sinogram[radial position][angular position][axial slice]
```

The size of this array is modified according to the input parameters producing a sinogram with dimensions (number of radial bins) × (number of angular bins) × (number of axial crystals × number of axial modules). Using the values calculated for $r_{LOR}$, $\theta_{LOR}$ and the axial slice in the previous section of the code, the corresponding sinogram element is incremented.

The values of $r_{LOR\ pixels}$ and $\theta_{LOR\ pixels}$ calculated are in floating point form (ie. numbers with decimal points). The sinogram array elements are discretised and therefore are referred to in integer form. In order to determine the sinogram element that the LOR falls into, the values for $r_{LOR\ pixels}$ and $\theta_{LOR\ pixels}$ need to be rounded into integer form. The rounded values access the desired elements in the sinogram with the value of that element incremented by 1.

Rounding of the $r_{LOR\ pixels}$ and $\theta_{LOR\ pixels}$ values for array referencing can however result in a significant reduction in the spatial resolution of the sinogram and furthermore can cause unwanted discretisation artefacts. In order to not "waste" the floating point information for $r_{LOR\ pixels}$ and $\theta_{LOR\ pixels}$, a unique solution was developed. A 1 pixel wide scoring kernel surrounding the $r_{LOR\ pixels}$ and $\theta_{LOR\ pixels}$ positions in the sinogram is first visualised. This kernel allowed contributions from adjacent pixels to be accounted for by determining the amount of the kernel overlapping these surrounding elements. A graphical representation process is shown in Figure 4.8 with example $r_{LOR\ pixels}$ and $\theta_{LOR\ pixels}$ values of 2.25 and 2.4 pixels respectively. The axial position is not significant in this process.

With versions 1.0 to 1.2 sinogram binning application, the only element incremented would be the element corresponding to $r_{LOR\ pixels}$=2 and $\theta_{LOR\ pixels}$=2. Version 1.3 and 1.4 of binning algorithm allows scoring into:

- $r_{LOR\ pixels}$=1, $\theta_{LOR\ pixels}$=1 **(Area $\mathbf{A}_1$)**
- $r_{LOR\ pixels}$=1, $\theta_{LOR\ pixels}$=2 **(Area $\mathbf{A}_2$)**
- $r_{LOR\ pixels}$=2, $\theta_{LOR\ pixels}$=1 **(Area $\mathbf{A}_3$)**
- $r_{LOR\ pixels}$=2, $\theta_{LOR\ pixels}$=2 **(Area $\mathbf{A}_4$)**

The contribution to each element corresponds to how much of the scoring kernel overlaps with the element (shown in the graphical representation in Figure 4.8). The areas of $A_1$, $A_2$, $A_3$ and $A_4$ are calculated using the floating point values for

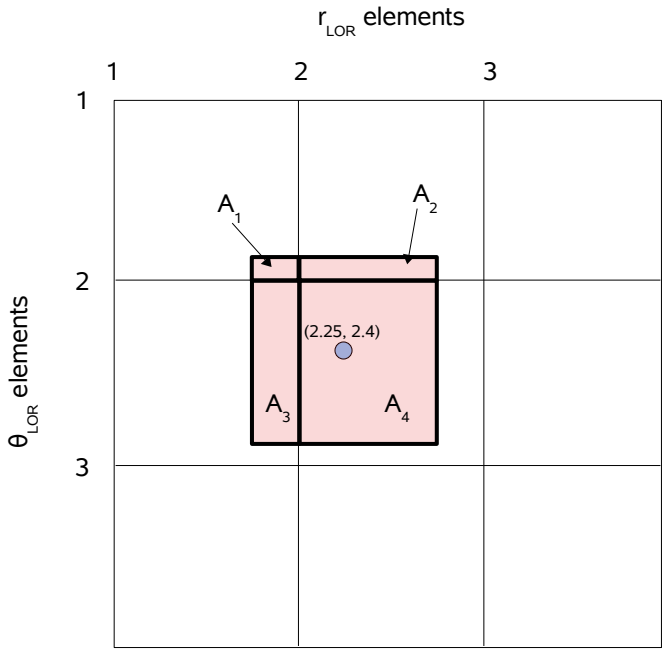


Figure 4.8: Sinogram Binning using a 1 pixel scoring kernel

$r_{LOR\ pixels}$ and $\theta_{LOR\ pixels}$. The corresponding values for $A_1$, $A_2$, $A_3$ and $A_4$ are then added to the sinogram element in which they lie. This results in a much "smoother" and accurate sinogram with fewer discretisation errors as shown in Figure 4.9. The reduction in the discretisation errors can clearly be seen at the centre of the FOV.

## 4.8 Data Output

The final stage of the sinogram binning application is to output the sinogram into data files ready for reconstruction. The data format for a given output file has X rows and Y columns where X is the number of elements in the radial bins within the sinogram and Y is the number of elements in the angular bins. Each element in the output file represents the number of counts for a LOR with given radial distance from the origin and angle.

There are a number of sinogram output files, each representing a different axial slice. For sources placed at the centre of the axial field, central slices record a higher number of counts than the slices at the axial extremities. This is as a result

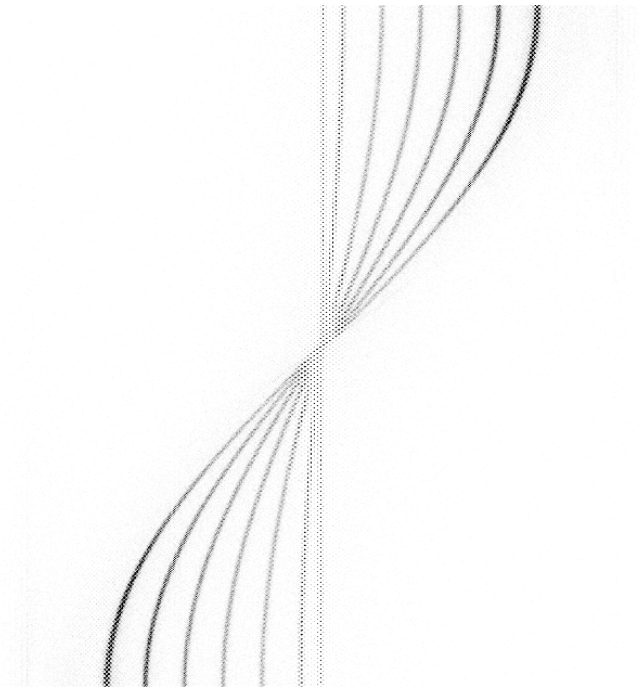

(a)

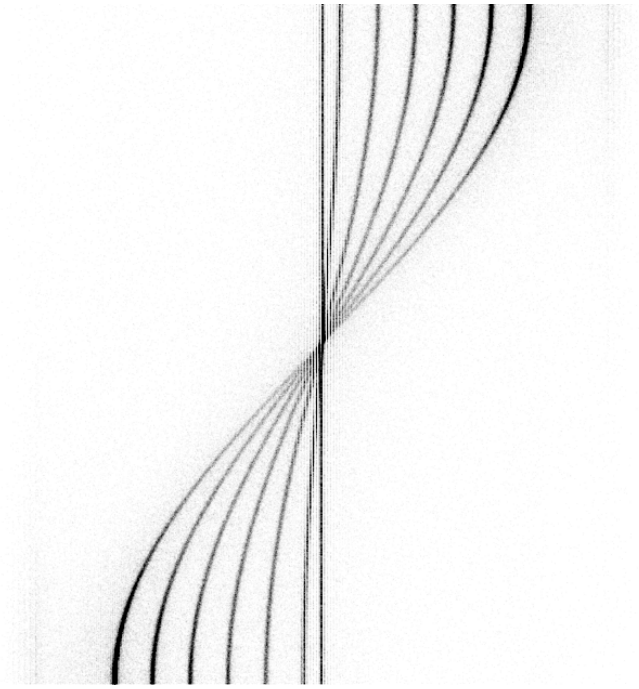

(b)

Figure 4.9: A comparison of the results of the (a) original binning (v1.0, v1.1, v1.2) and (b) new binning (v1.3, v1.4) techniques. There are fewer discretisation errors within (b), especially at the centre of the sinogram and all of the lines in the sinogram appear "smoother".

of the SSRB algorithm determining the average axial position to be close to the axial centre. The magnitude of the counts recorded in the 8 slices for sources placed at the axial centre are shown in Figure 4.10. The slices exist from the axially most negative position in the world volume to the axially most positive position. The top row contains slices 1, 2, 3 and 4 while the bottom row contains slices 5, 6, 7 and 8. The sources are placed at the position represented by the boundaries of slices 4 and 5. The number of counts recorded in these central slices is significantly greater than in slices 1, 2, 3, 6, 7 and 8. In order for these lower counts to be visible, the brightness of the image was adjusted, resulting in "clipping" of the counts in the central slices. That is, greyscale values have been forced to their maximum value (white) by this process.

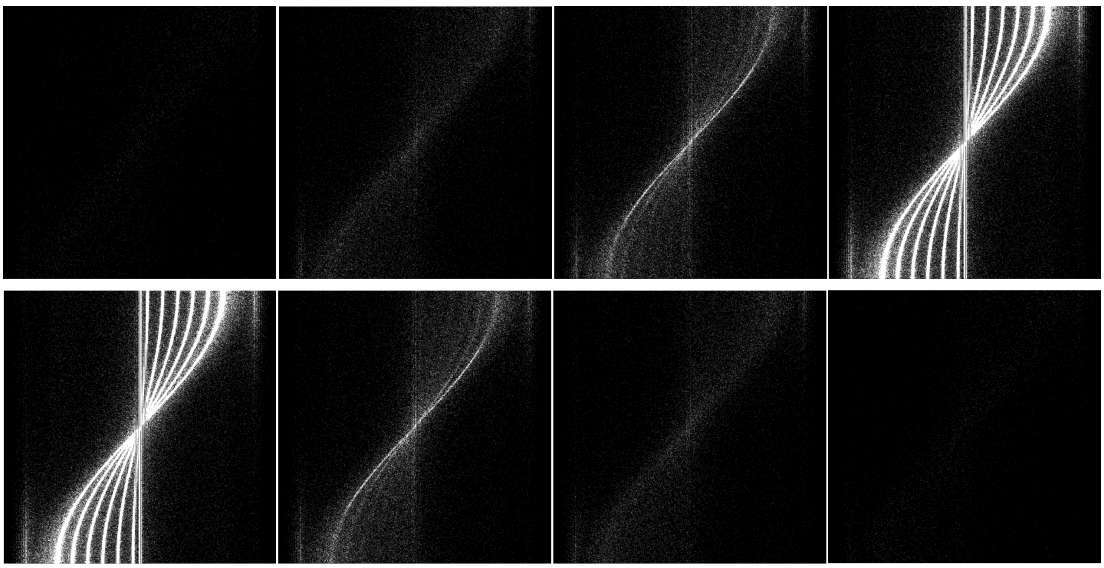

Figure 4.10: The sinograms for each of the 8 slices. The sinograms start on the top left at the axially most negative position and the bottom right sinogram is at the axially most positive position.

## 4.9 Advanced Features

### 4.9.1 Introduction

The basic function of the sinogram binning application was outlined in the previous sections of this chapter, however the application has numerous other features which allow it to be robust and adaptable to other types of data from Monte Carlo PET scanners. An outline of the advanced features is presented in the following sections.

### 4.9.2 Crystal Rebinning

As stated in Section 2.9.1, different crystal types are sandwiched together to provide a module with multiple layers, capable of DOI measurements. The total thickness of the crystals is comparable to monolithic crystal detectors in order to maintain sensitivity. The amount of DOI information that can be extracted from a phoswich scanner is affected by the number of different layers present and the ability to localise a signal to a specific layer. It is possible to mimic the behaviour of a phoswich scanner for this data using a crystal rebinning technique. The user can choose how many layers of DOI information are to be provided to the sinogram binning process. This relies on the DOI data being acquired correctly from the GATE study with a greater or equal number of layers in the Monte Carlo study than required by the sinogram binning process. If the user has specified different values for the rebinned number of crystals and the actual number of crystal layers, rebinning of the data is undertaken. Figure 4.11 shows the change in the depth of each crystal for an 8 layer module being rebinned into a 4 layer module.

Section 4.4 presented the calculation associated with determining the centre of the crystal element in which the pulse is detected. When rebinning the data into a different number of layers, the centroid of the element in which the pulse is determined changes according to the number of layers the data is being binned

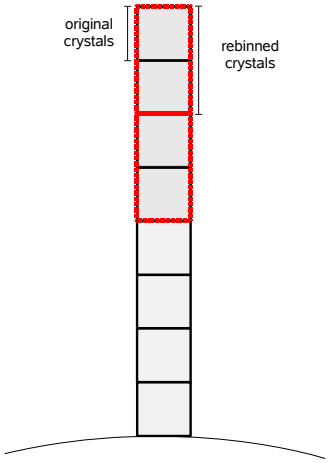


Figure 4.11: Rebinning of DOI to simulate phoswich scanners; in this case, 8 layers are rebinned into 4 layers making each crystal twice as long

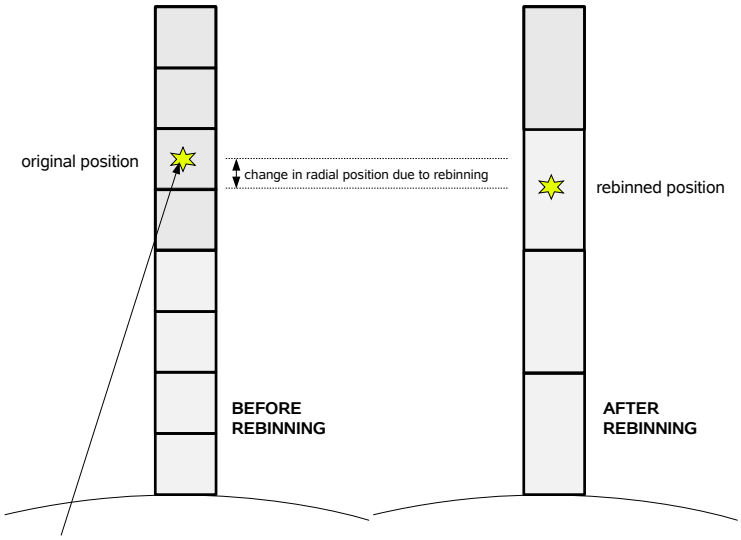


Figure 4.12: Rebinning of DOI for a pulse from an 8 layer module into a 4 layer module

into. This positional change depends on the number of rebinned layers the user defines. Figure 4.12 again shows the 8 layers of data being rebinned into a scanner containing 4 DOI layers with the positional errors associated to rebinning. The errors effectively reduce the accuracy of the DOI information and by using this data, the effect of decreasing the number of DOI layers on the spatial resolution can be quantified.

### 4.9.3 Larger Detector Modules

In many PET scanner designs, detector modules contain multiple crystals in the axial and tangential direction (as well as the radial direction if they record DOI). It is therefore necessary to make the sinogram binning application capable of processing data from detector modules with multiple tangential elements within a detector.

The specification of crystalIDs for a module with multiple tangential elements is different to modules which contain only 1 tangential element. As Figure 4.13 shows, the crystalIDs are first incremented along the radial direction and then the tangential direction and finally the axial direction. The sinogram binning application upto this point is only capable of determining the position of the block directly along its central axis. A method of determining the position of points of interaction at positions away from the central axis of the larger detector module was developed using a set of correction factors for the radial and tangential directions as well as the angular shift.

For a larger detector module with multiple crystals in the axial and tangential direction, the radial distance simply becomes the ring radius plus the radial correction factor. The radial correction factor is specified by:

$$\begin{aligned} radial\ correction\ \ = \ \ & \left\{ floor \left[ \frac{crystalID\ mod\ layers\ per\ module}{\left( \frac{layers\ per\ module}{rebinned\ number\ of\ layers} \right)} \right] + \frac{1}{2} \right\} \\ & \times\ crystal\ size \times \frac{layers\ per\ module}{rebinned\ number\ of\ layers} \end{aligned} \tag{4.17}$$

The reference to "floor" in this and future equations is a mathematical function available in C++ which rounds a floating point value down to the nearest integer

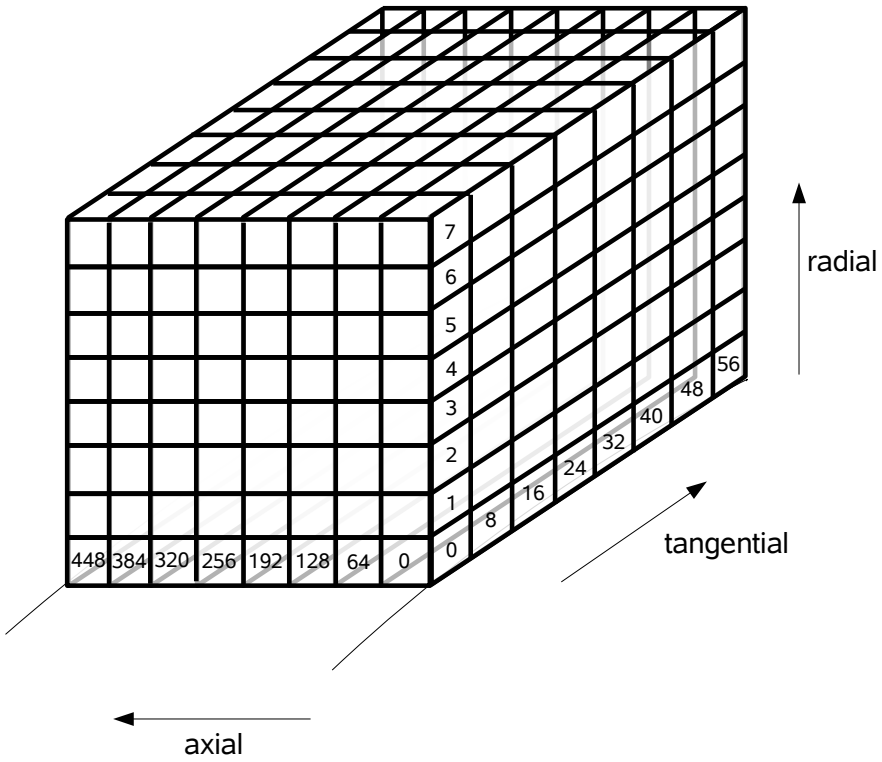


Figure 4.13: Larger detector modules and the method by which the detectorIDs are incremented

value.

The tangential correction factor is specified as:

$$tangential\ correction = \left\{ -1\ \times\ \frac{crystals\ in\ tangential\ direction}{2}\ +\ floor \left( \frac{crystalID\ mod\ (crystals\ in\ tangential\ direction \times rebinned\ number\ of\ layers)}{rebinned\ number\ of\ layers} \right) + \frac{1}{2} \right\} \times crystal\ size \tag{4.18}$$

The angular correction is determined by using the tangential correction and the radial distance resulting in:

$$angular\ correction = tan^{-1} \left( \frac{tangential\ correction}{radial\ distance} \right) \tag{4.19}$$

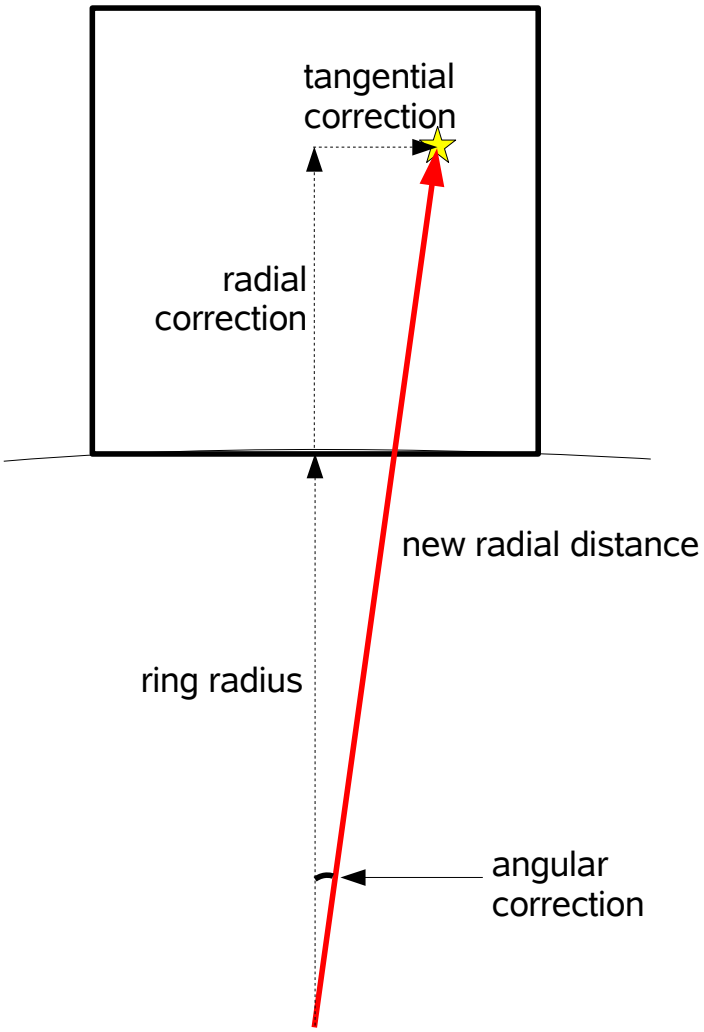


Figure 4.14: The tangential and axial corrections (not to scale)

The new distance from the centre of FOV is determined using Pythagoras' Theorem and the correction factors as illustrated in Figure 4.14. At this point, the position calculation process returns to Equations (4.3) and (4.4) and follows on as previously outlined in Section 4.6.

### 4.9.4 Rotating Scanner

In some circumstances, it is possible to achieve identical LORs from interactions within different crystal and rsector pairs. An example is shown in Figure 4.15 where a single LOR can be recorded from 2 different sets of detectors.

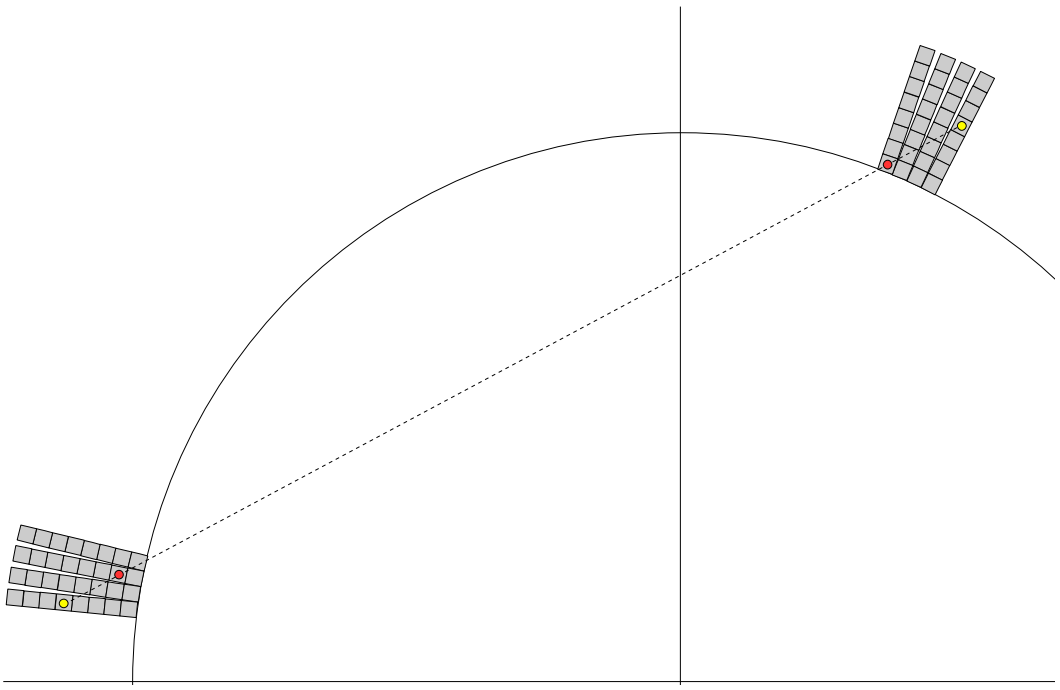

Figure 4.15: LOR redundancy showing 2 different possible coincidences which can create a single LOR

In order to fully utilise the 8 layer features of this detector module, the gantry can be rotated slowly leading to greater angular sampling. Rotating the gantry effectively simulates the detector ring being filled completely with scintilator crystals as a static gantry has dead space between detector modules. The dead space between the detector modules forces certain LORs to not be recorded resulting in decreased sensitivity and zero efficiency bins within the sinogram. However, if the rate of rotation is appropriately selected, the dead space can be made to appear as if they are filled with scintillator crystal and enable the recording of other LORs which may not have been measured if the gantry was stationary.

If the user specifies that rotation data has been recorded in the simulation output files, the gantry angular position is considered when calculating the angle of the LOR.

### 4.9.5 Cartesian Coordinate Rebinning

The GATE simulations can be set up not only to provide detectorIDs for each coincidence but also to provide the exact position of each single measured within the crystal. It is not possible to acquire this data in an experimental study as infinitesimally small, optically isolated sensitive volume elements are required. This feature is incorporated into the sinogram binning program to indicate the theoretical limit of performance for a given detector geometry and sinogram binning parameters. As this method utilises the exact coordinate of interaction, there are no discretisation artefacts observed and hence the sinogram is far superior to any of the other detectorID sinogram rebinning with the same upsampling factor. The sinograms when using both detectorIDs and exact cartesiathen coordinate binning methods is shown in Figure 4.16.

During the user input stage, the user can specify whether the sinogram binning is undertaken using detectorIDs or cartesian coordinate information. If the cartesian coordinate option is selected, the interaction position calculation described in Section 4.4 is skipped as the coordinates of the interaction position are known from the data directly.

### 4.9.6 Multiple Axial Detector Module Geometries

As a single module in this study has 8 rings covering 24 mm in the axial direction, it is necessary to incorporate a number of modules in order to provide greater coverage in the axial direction. The rsector IDs for a single axial module scanner increments together with the adjacent angular position of the rsector. For multiple axial modules, consecutive rsector IDs correspond to rsectors at the same angle but

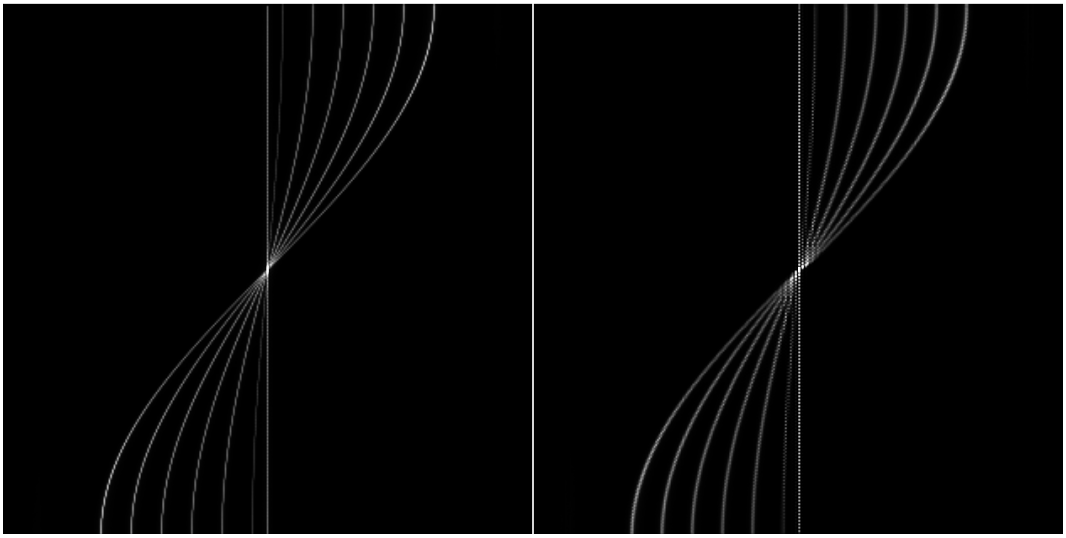

Figure 4.16: Cartesian coordinate sinogram binning (left) vs DetectorID binning (right). An improvement in the "smoothness" of each line within the central line in the sinogram can be noticed, as well as a decrease in the width of the lines when the cartesian coordinate method is employed.

axially adjacent modules. Hence, in a multiple axial module scanner, angularly adjacent rsectors at a given axial position have rsector IDs that are separated by the number of axial modules in the scanner. Additional code is embedded in the interaction position calculation code (as specified in Section 4.4) to account for multiple axial modules.

As photons scatter within bodies, they not only deflect in transaxial plane but in the axial plane as well. GATE rejects coincidences which occur within 3 rsectors of each other, however no such mechanism is in place for the axial direction for multiple axial modules. The sinogram binning application allows the user to reject coincidences which occur between elements in modules separated by a user specified value. That is, the user can choose to reject coincidences occuring outside a specified ring span. A ring span of 8 corresponds to "singles" detected within the same ring (as observed in a single ring system). Rejection of inter-ring scatter leads to a reduction in the number of random coincidences. However, it also leads to a reduction in the sensitivity of the scanner. Figure 4.17 shows a cross section

in the axial direction (N.B. multiple layers are not shown for clarity). This shows coincidences which do and do not meet the selection criteria for a specified ring span of 24. That is, if the 2 positions within the coincidence are separated by greater than 24 rings, it will be rejected and not counted.

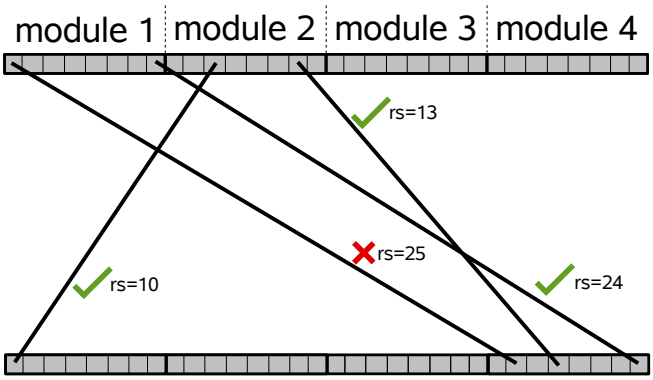


Figure 4.17: An axial view of a scanner with a specified ring span of 24 illustrating the LORs that will be accepted and rejected

### 4.9.7 Energy Discrimination and Histograms

The energy of each interaction is recorded by the Monte Carlo simulations and stored in the output data file as described in Section 3.3.9. In order to prevent having to perform multiple simulations with different energy windows, a single simulation with an energy window from 150-650 keV is considered for each study. The sinogram binning application then undertakes post filtering of the coincidence to ensure that the recorded energies for that coincidence lie within the specified LLD and ULD values set by user input. If the energy deposition of each coincidence lie within the discriminator values, further calculation of the LOR takes place, however if the energy deposition lies outside, the coincidence is ignored and the next coincidence read in. By increasing the value of the LLD, the amount of coincidences rejected by the photons increases significantly.

The user can also analyse the energy depositions within the coincidences. The

energy data can be processed by the sinogram binning application and placed in an output file in the form of a histogram. If processed, the output file contains two columns, the 1st being the energy deposited and the 2nd being the number of interactions recorded in that energy bin. The data can be processed offline by a spreadsheet or graphing package.

### 4.9.8 Unscattered/Scattered Coincidences Ratio

One of the parameters that can be selected using the data output mask in GATE is a recording of the number of Compton interactions within the phantom and the detector crystals. The number of interactions within the phantom cannot be directly measured in an experiment and accurate measurement of scattering between crystals is a challenging task due to lack of energy and timing resolution. Hence, Monte Carlo information can provide an insight into these aspects. During the user input stage of the sinogram binning application, the user can specify whether Compton scatter data is present within the data. If this flag is incorrectly selected, subsequent data read in from the Monte Carlo output is placed in the incorrect variables and errors in the sinogram binning application can occur.

The number of interactions within the phantom provides a relatively simple method of determining the amount of scatter in a study. The sinogram binning application determines whether a given coincidence has a photon which has Compton scattered within the body and if so, increments a scattered coincidences counter. The number of unscattered coincidences is also recorded and at the end of analysing the data set, a ratio for the unscattered to total coincidences is calculated using:

$$unscattered\ photon\ ratio = \frac{unscattered\ coincidences}{scattered\ coincidences + unscattered\ coincidences} \tag{4.20}$$

#### 4.9.9 .info File

An information file containing the parameters used in binning the sinogram is also provided at the completion of sinogram binning. This file provides information related to the ring geometry, the number of counts analysed, upsampling factor, method of interaction and position calculation to name a few. It is provided as a reference point for the sinogram slices as it is not possible to embed this data within the sinogram data, nor is it possible to provide the sinograms with detailed filenames which contain all the necessary information.

### 4.10 Image Reconstruction and Analysis

The sinograms obtained in this study are reconstructed using a Radon Transform (Backprojection) plugin [53] available for ImageJ [54] which is a freely available Java based image processing toolkit with a wide range of scientific data analysis tools. A typical sinogram constructed from a Monte Carlo study along with a measured line profile showing the ImageJ user interface is shown in Figure 4.18.

The Radon Transform plug requires 8-bit greyscale images with the number of projection angles and the size of the angular increments, as well as the type of filtering required. The NEMA specifications for quantification of a PET scanner suggest the use of a ramp filter with cutoff at the Nyquist frequency for reconstruction.

The sinogram binning application does not provide the sinogram in the correct format for the Radon Transform plugin to reconstruct and hence requires manipulation using a graphical editing program. A detailed description of the process required to reconstruct the image using the Radon Transform plugin is provided in Appendix B.

The zoomed-in reconstructed image of a series of point sources is shown in Figure 4.19. A straight line is drawn through the sources and the profile measured along the line using the "Plot Profile" feature in ImageJ.

The real distance between the peaks in millimetres is known and a calibration

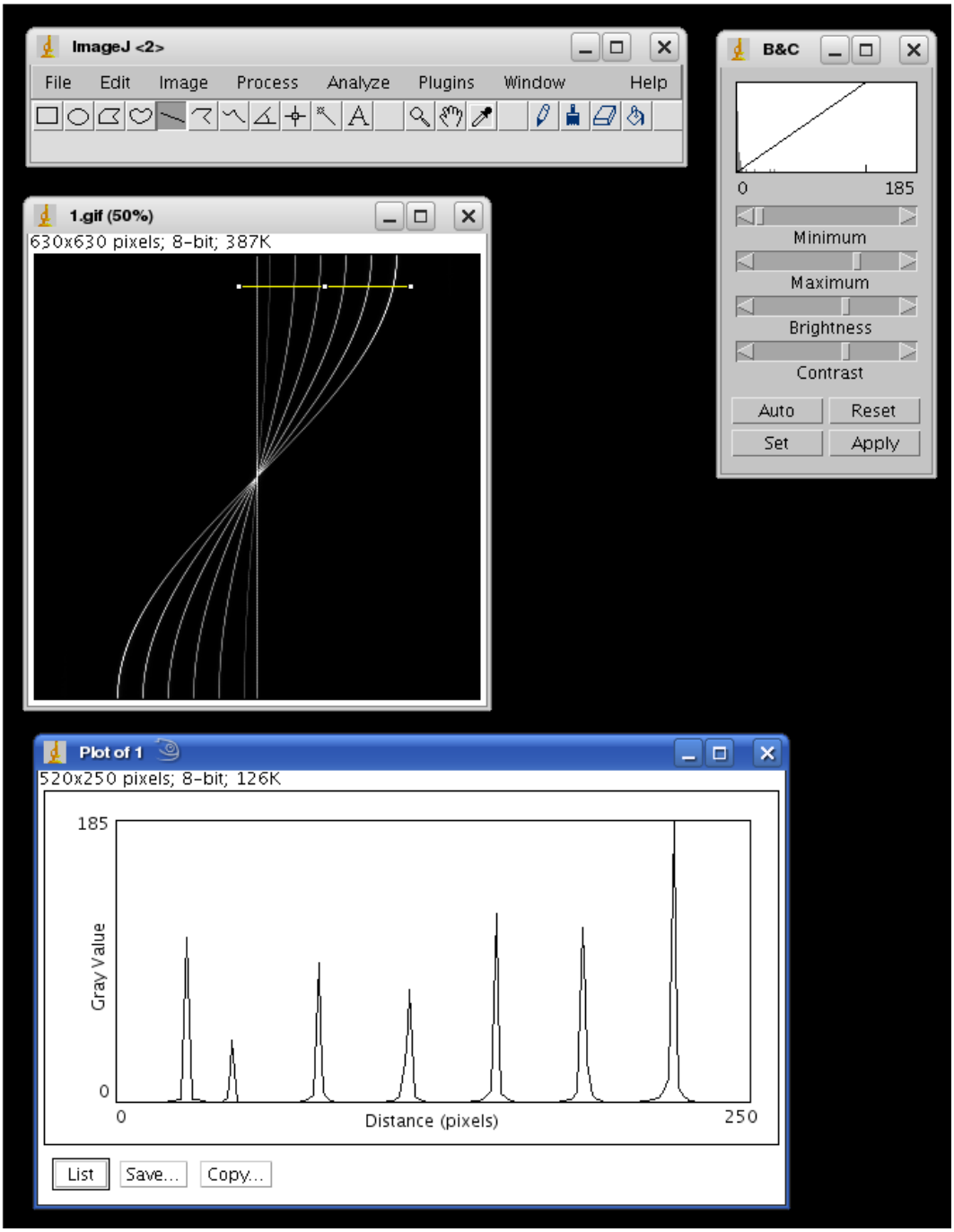


Figure 4.18: The ImageJ user interface with a measured line profile of a section of a sinogram

factor for the distance versus reconstructed image pixels is determined. Using this quantity, the point spread function (PSF) of each source can be measured, a measure of the spatial resolution of the scanner at that point.

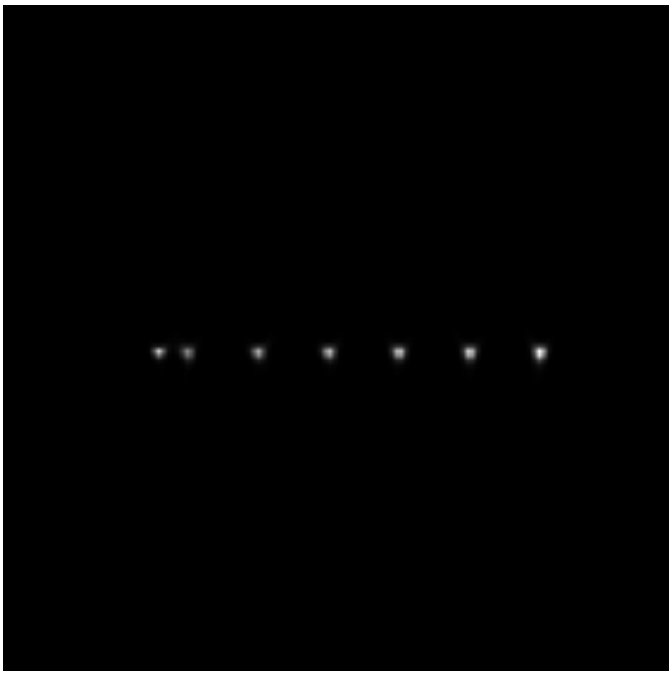

Figure 4.19: A reconstructed image showing 7 point sources

# CHAPTER 5

# EXPERIMENTAL VERIFICATION OF SINOGRAM BINNING APPLICATION

## 5.1 Introduction

The sinogram binning application is the greater contribution to the work presented in this thesis. The accuracy of the results presented is highly dependent on the performance and limitations of the sinogram binning application. Experimental work was undertaken to provide verification that the sinogram binning application operates as expected using a MicroPET Focus 220 scanner at the Brain and Mind Research Institute (BRMI), Camperdown, Australia. There have been numerous studies published related to Monte Carlo studies of MicroPET scanners and this study is not attempting to supersede the results presented previously; this study is designed to compare the Point Spread Functions (PSFs) across the FOV for experimental data with the GATE simulation data processed with the sinogram binning application. Agreement between both sets of data provides offers verification of the sinogram binning application and suitability for future use.

## 5.2 MicroPET Focus 220 Small Animal PET Scanner

As only 4 detector modules of the proposed design exist, the MicroPET Focus 220 scanner was selected as an alternative as it was readily available and had been previously modelled extensively in GATE. The MicroPET Focus 220 is a high resolution small animal PET scanner. It has 4 rings of diameter of 260 mm containing 42 detector modules each. The detector modules have a 12 $\times$ 12 array of 1.5 $\times$ 1.5 $\times$ 10 mm$^3$ LSO crystals. The active field of view is 196 mm.

The hierarchy of the sinogram binning application requires that a "cylindricalPET" family scanner is defined with a mother "rsector" volume filled with smaller "crystal" volumes. In the case of the MicroPET scanner, each rsector volume is $19.1 \times 19.1 \times 10$ mm$^3$ containing a $12 \times 12$ array with 6 layers of $1.5 \times 1.5 \times 1.5$ mm$^3$ LSO scintillator. One of the major limitations of the sinogram binning application is the requirement of cubic crystal volumes, hence the necessity to define 6 layers of crystal whereas in reality, the MicroPET scanner utilises only a single $1.5 \times 1.5 \times 10$ mm$^3$ crystal element. Using six $1.5 \times 1.5 \times 1.5$ mm$^3$ cubic crystals results in an extra 0.5 mm of crystal in the radial direction however the result of this is minimal as most photons are absorbed within the first few millimetres of the the crystal. The data from the multiple layers is combined in the sinogram binning application to simulate a single 10 mm long crystal.

## 5.3 Phantom for Experimental Work

The experiments required the building of a phantom which could be easily modelled in GATE. A large hollow cylinder was selected as the basic shape of the phantom and was able to have "hot" active sources placed inside, isolated from the "background". An illustration of this phantom is shown in 5.1. The hollow section can be filled with water and radioactive FDG to create the "background" activity in order to create a scatter contribution to the acquisition. The hot sources are placed at positions as used in the Monte Carlo studies with line sources placed at the centre of FOV, 10 mm, 30 mm, 50 mm and 70 mm off-centre of the FOV. The phantom is constructed out of perspex has an external diameter of 180 mm and is 65 mm thick with internal dimensions of 165 mm and 50 mm respectively. A top view and a cross sectional view are shown in Figure 5.2 and Figure 5.3 respectively.

A number of large screw holes are placed into the phantom to enable filling and draining of the hollow part of the phantom. Each screw is made out of nylon with the threaded section covered with thread tape to provide better water-sealing. A

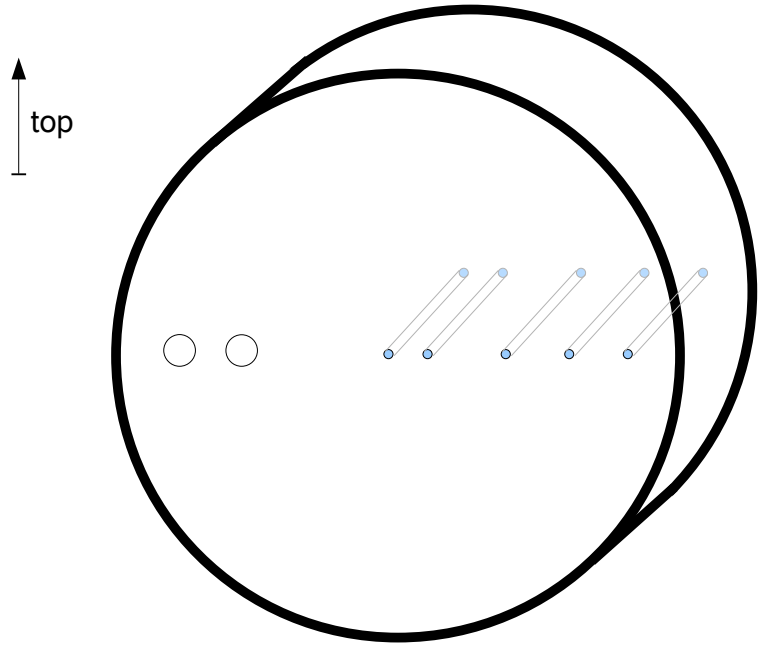


Figure 5.1: An outline of the phantom used in the experimental work

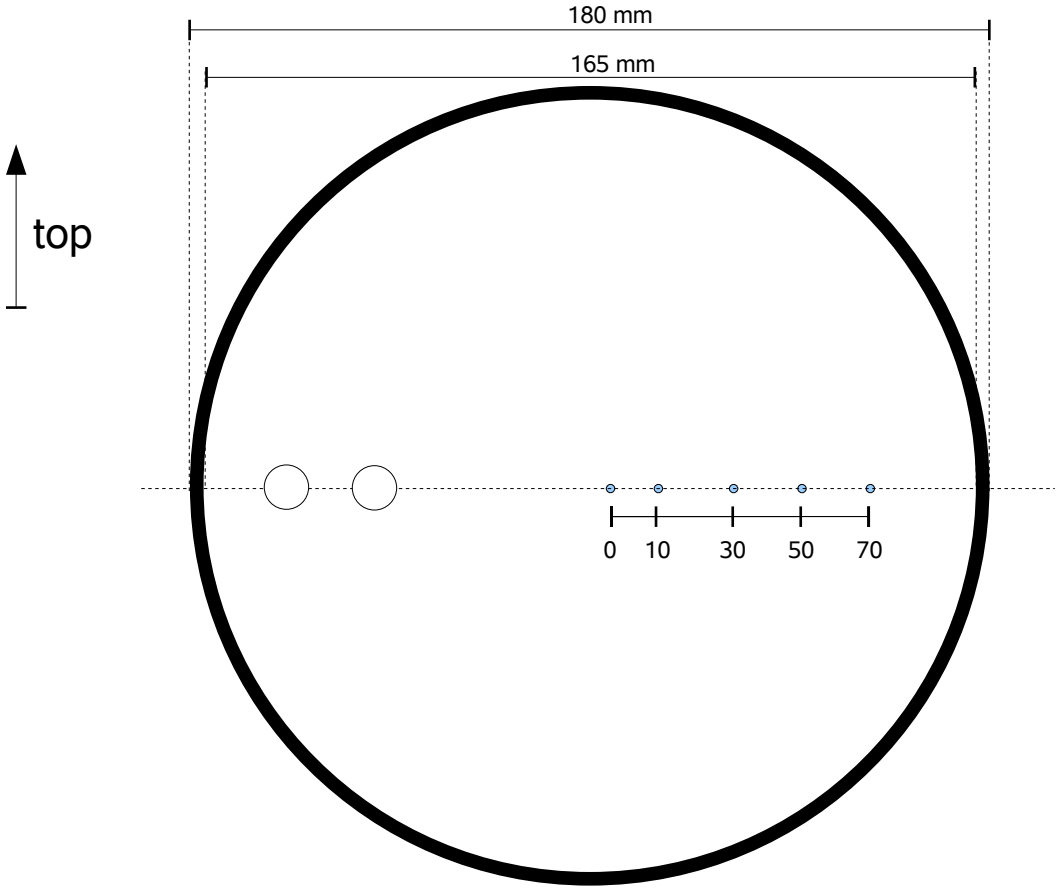


Figure 5.2: A top view of the phantom

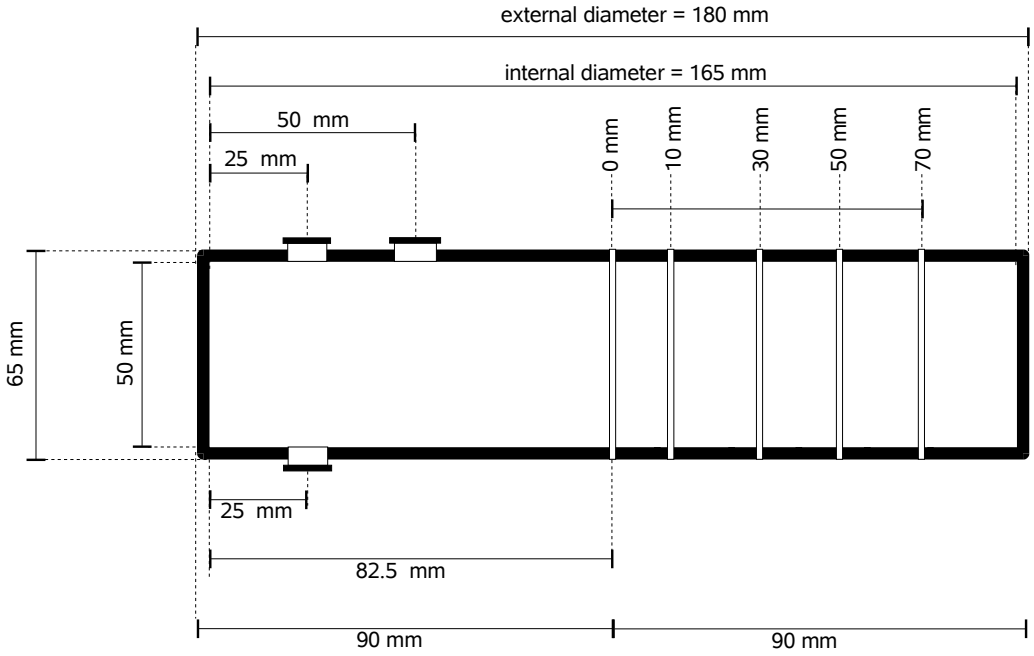


Figure 5.3: A cross sectional view through the dotted line shown in Figure 5.2

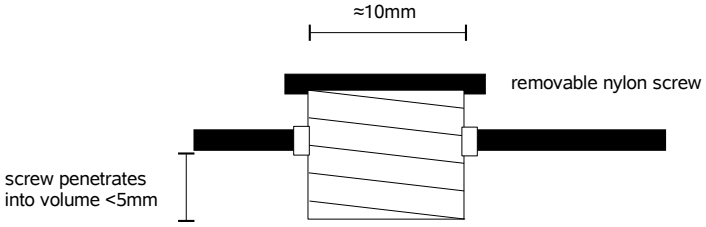


Figure 5.4: The screw mounting within the phantom

diagram illustrating the screw mounting is shown in Figure 5.4.

The tubes in the phantom are made out of a long section of 4 mm external diameter, 2.5 mm internal diameter glass capillary. The required 50 mm lengths are cut and insterted into the holes in the phantom and sealed using a liquid perspex glue. A cross section of the tube mounting is shown in Figure 5.5.

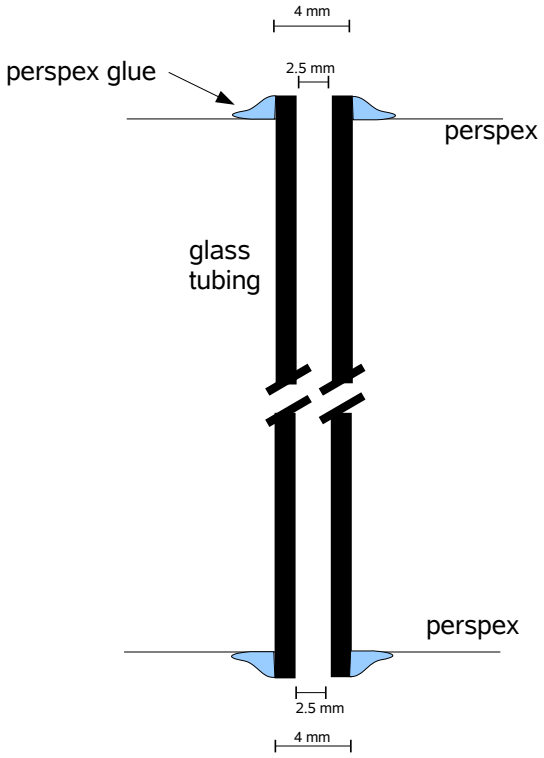


Figure 5.5: The mounting of the glass tubes

## 5.4 MicroPET Focus 220 Experiments

The phantom was filled with 1.07 L of water and an initial transmission study undertaken with a Cobalt-57 point source. This transmission study was used for attenuation correction of all other acquisitions. A figure showing the phantom on the microPET bed awaiting imaging is shown in Figure 5.6

The capillaries (shown in Figure 5.7) used in this study for containing the radioactive liquid have an external diameter of 0.8 mm and an internal diameter of 0.5 mm. They were filled with Fluorodeoxyglucose (FDG) and inserted into the hollow tubes of the phantom. The ends of each capillary were pressed into a putty-like sealer to ensure the FDG remained inside the tube. The total volume of liquid inside the capillary was approximately 0.1 mL.

### 5.4.1 Source to Background Ratio Studies

The Monte Carlo studies undertaken investigated unrealistic scenarios with simple point sources in air and in a large homogenous water phantom. A more common clinical situation includes hot sources placed inside a volume with background activity. A number of tests investigating the tumour to background activity ratio were undertaken on the MicroPET scanner. The activity ratio of the sources to the background was initially set to 3:1 with a total activity of 37.5 MBq inserted into the phantom. A 20 minute acquisition period was used with the LLD and ULD set to 350 keV and 650 keV respectively and the coincidence window set to 6 ns. The

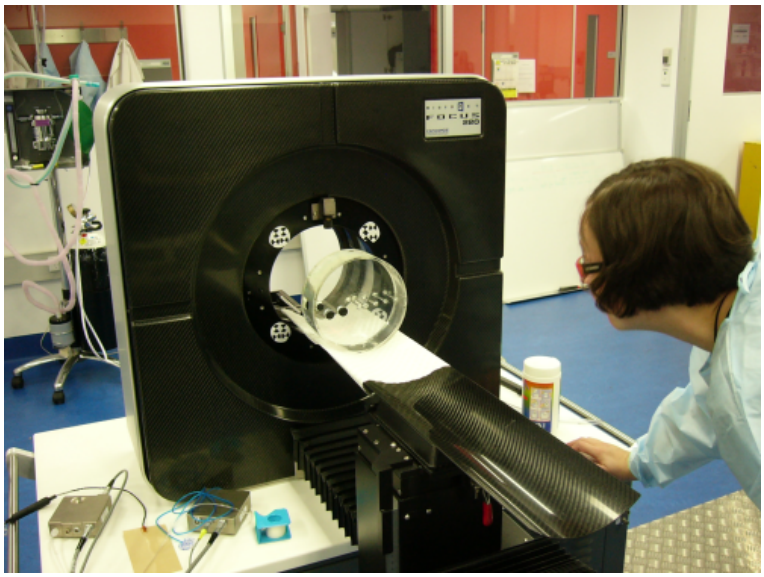

Figure 5.6: The phantom on the microPET bed awaiting insertion into the detector ring

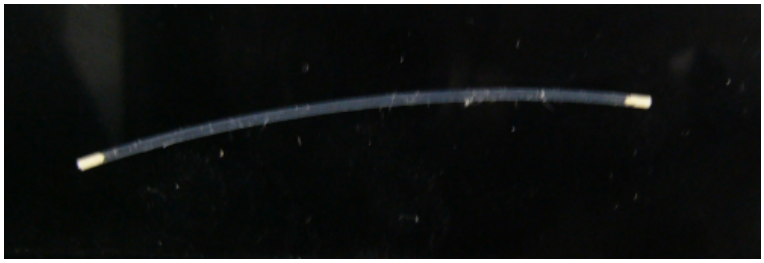

Figure 5.7: The capillaries filled with FDG used inside the tubes of the phantom

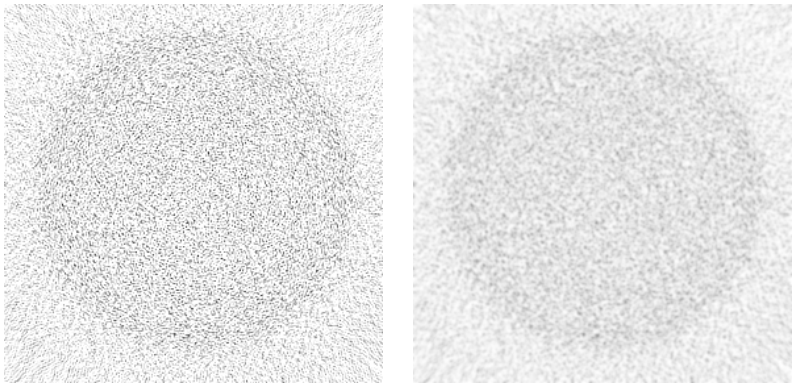

(a) Pre-filtering (b) Post-filtering

Figure 5.8: Pre- and post-filtered image reconstructions of the water phantom and sources acquired by a MicroPET Focus 220 Scanner. Filtering reduces some of the high frequency noise at the expense of sharpness.

sinograms from the MicroPET are 288 × 252 pixels and form part of a 66 MB data set containing LORs from various axial rings and segments. The central slice for segment 0 (ie. axially normally incident LORs only) are extracted using IDL and reconstructed using the method described in Appendix B. In this case however, the sinograms are 288 × 252 requiring the sinogram to be resampled along the y-axis to make it 288× 288 pixels and enable the Radon Transform plugin within ImageJ to reconstruct it.

The final reconstructed images are rather grainy as shown in Figure 5.8(a) as the acquisitions are relatively short when considering the injected activity and the sensitivity of the microPET scanner. A smoothing filter was applied to each image after reconstruction, removing some of the high frequency noise at the expense of sharpness as shown in Figure 5.8(b).

The reconstructed images show the background activity of the cylinder quite well. However, the sources, with an activity concentration 3 times higher, are not discernable from the background as Figure 5.10(a) shows. The test was repeated for background activity ratios of 5:1, 10:1 and 100:1 (as shown in Figure 5.9 (b), (c) and (d) respectively) with identical results, where the sources could not be located.

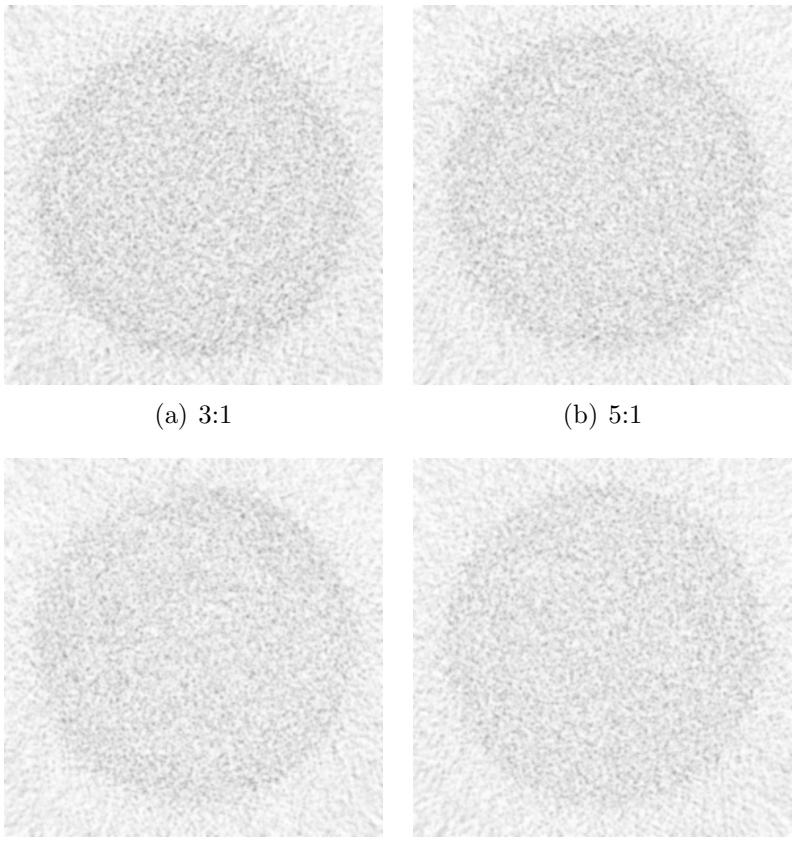

(a) 3:1 (b) 5:1

(c) 10:1 (d) 100:1

Figure 5.9: Reconstructed images from the microPET scanner for various source to background activity ratios

This can be attributed mostly to the partial volume effect as the sinogram's pixels cover a significantly larger volume than the actual volume represented by the source. The partial volume effect "smears" the small source's activity over a larger pixel reducing its brightness and the ability to differentiate it from the background.

### 5.4.2 Point Spread Function Studies

The activity within each of the capillaries was increased to 45 MBq and a 20 minute acquisition performed. The energy window had LLD and ULD values of 350 and 650 keV. The reconstructed images from these studies would enable the point spread functions (PSFs) of the sources to be measured across the FOV. A zoomed

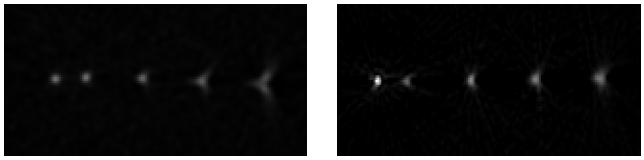

(a) Experimental (b) Monte Carlo

Figure 5.10: The reconstructed point sources for (a) the experimental study and (b) the Monte Carlo study

in section of the reconstructed point sources from the experimental is shown in Figure 5.10(a) while the Monte Carlo study for the same sources is shown in Figure 5.10(b). At this point in the study, the background activity had not been updated and was approximately 2 half-lives old, reducing the activity in the phantom to approximately 10 MBq. This constituted a source to background ratio of approximately 9000:1. In this study, only the sources are visible and the background is not visible unless the brightness and contrast of the final image is significantly adjusted.

The PSFs were measured for each study and are shown in Figure 5.11. Along with the data from the Monte Carlo and experimental studies, another set of spatial resolution data as measured by Tai et. al. [55] has also been presented to show the validity of the data from this study. The Tai study utilised a Sodium-22 source of nominal size 0.5 mm placed inside a lucite disc moved across the FOV. An energy window of 250 - 750 keV was used, along with a coincidence 6 ns.

As Figure 5.11 shows, the resolution of the Monte Carlo and experimental data follows the same trend, however there appears to be a constant offset of approximately 0.4 mm. This offset is predominantly due to the method in which the sinogram is binned. The experimental data provides a sinogram that is 288 $\times$ 252 while the Monte Carlo sinogram is 336 $\times$ 336. The sinogram dimensions from the sinogram binning application are determined by half the number of rsectors in the ring (21) multiplied by the upsampling factor (in this case set to 16) as mentioned Section 4.7 However, in this case, there is no DOI information as the microPET

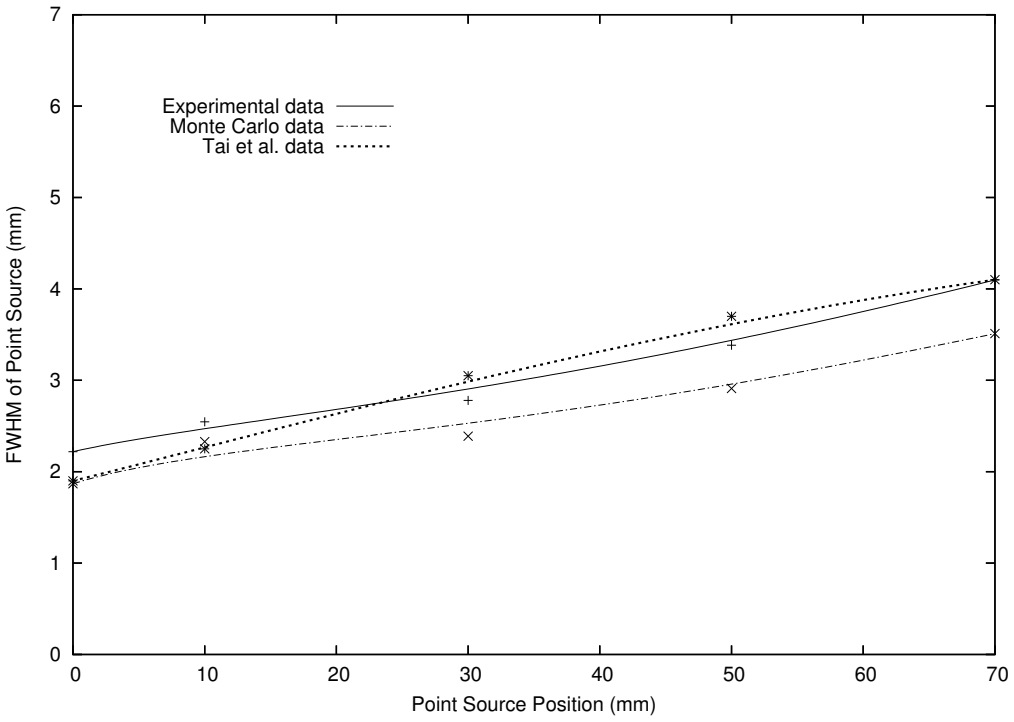


Figure 5.11: The experimentally measured and Monte Carlo PSFs of point sources placed across the FOV

has monolithic crystals and selecting a higher upsampling factor simply increases the dimensions of the sinogram without actually increasing angular and positional sampling. It is anticipated in future studies that the sinogram dimensions can be adjusted manually by the user without being automatically defined according to the number of detector modules and the upsampling factor (discussed in further detail within Section 7.1.14).

The study was repeated for two other LLD values, 250 keV and 150 keV and identical PSFs were recorded. The only noticeable difference between the three sets of data was the SNR value with increasing amounts of noise detected as the LLD was reduced. Even with the LLD at its lowest value of 150 keV, the noise levels were extremely low and had no effect on the measured resolution of the sources.

## 5.5 Conclusion

The experiments carried out at the Brain and Mind Institute using the MicroPET Focus 220 Scanner provide an excellent method of verifying the sinogram binning application. As the data presented above illustrates, excellent correlation is observed between the experimental data and the Monte Carlo data processed with the sinogram binning application. Both sets of data also corresponds well with previously established resolution data as presented by Tai et al. Hence, the sinogram binning application is a suitable tool for the processing of data produced by Monte Carlo studies.

# CHAPTER 6

# APPLICATION OF SINOGRAM BINNING APPLICATION TO ANALYSE MONTE CARLO DATA

## 6.1 Introduction

The work of this thesis centres on the development of a sinogram binning application capable of accepting the depth of interaction data output from Monte Carlo simulations of the newly developed detector module, as discussed in detail in Chapters 3 and 4. This chapter presents the results of Monte Carlo simulations analysed using the sinogram binning application, including optimisation of the sinogram binning application, point spread function (PSF) measurements and scatter studies.

## 6.2 Sinogram Binning Optimisation

The sinogram established using a PET study plays a significant role in the quality of the final image reconstruction. As mentioned in Section 4.7, the number of detector modules around the ring determines the number of projection angles that an LOR can possibly have. For $n$ detector modules, there are $n/2$ possible projection angles, subsequently, the sinogram has $n/2$ angular samples (the y-axis of the sinogram). As the proposed detector modules contain DOI information, further LORs are possible with smaller angular increments than a similar monolithic crystal and hence upsampling of the data takes place as outlined in detail in Section 4.7. However, improvement in the spatial resolution can only be obtained if the upsampling represents the LORs more accurately than non-upsampled data. If the sinogram is upsampled by a much larger factor than necessary to represent all of

the data, oversampling occurs and artefacts are observed in the sinogram, as can be seen in Figure 6.1(a). This figure shows "zero efficiency" bins at the centre, or bins which have not registered any counts inside them. That is, there were no LORs with the radial distance and angle represented by those bins in the sinogram. The zero efficiency bins are of significance as they can cause unwanted streak artefacts in the image reconstruction. It is possible to create greater sampling in the sinogram by rotating the gantry [52], resulting in some of the "zero efficiency" bins registering counts. Figure 6.1(b) shows a sinogram from a rotating gantry. The difference between the two sinograms is very slight and may not be visible in all prints of this document. In the rotating gantry sinogram, note the increase in sampling observed for the central sources with fewer "blocky" areas, especially at the exact centre of the sinogram. However oversampling is still present, as are a large number of zero efficieny bins. As a result of the improvement that has been demonstrated, the gantry in all of the Monte Carlo studies presented in this chapter was rotated about the z-axis at 0.5 degrees/sec.

In order to quantify the effect of upsampling on the PSFs, a simulation with point sources at 0, 10, 30, 50, 70, 90 and 110 mm from the centre of FOV within a large 120 mm radius water phantom placed inside a 150 mm diameter ring containing 314 detector modules was undertaken. The data from this study was then processed with different upsampling factors. The PSFs across the field of view was determined and are shown in Figure 6.2. Increasing the upsampling factor, as somewhat expected, resulted in an improvement in the PSFs. However, significant image artefacts are observed in the reconstruction at the centre of FOV with increasing upsampling factor due to the zero efficiency bins and inherent properties of the FBP algorithm. The FBP algorithm creates streak artefacts as a result of insufficient sampling as previously illustrated in Figure 2.27. The streaks are observable at the central point sources in Figure 6.3 which shows the reconstructed images for different upsampling factors. For this figure and all proceeding figures, smooth bezier curves were fitted

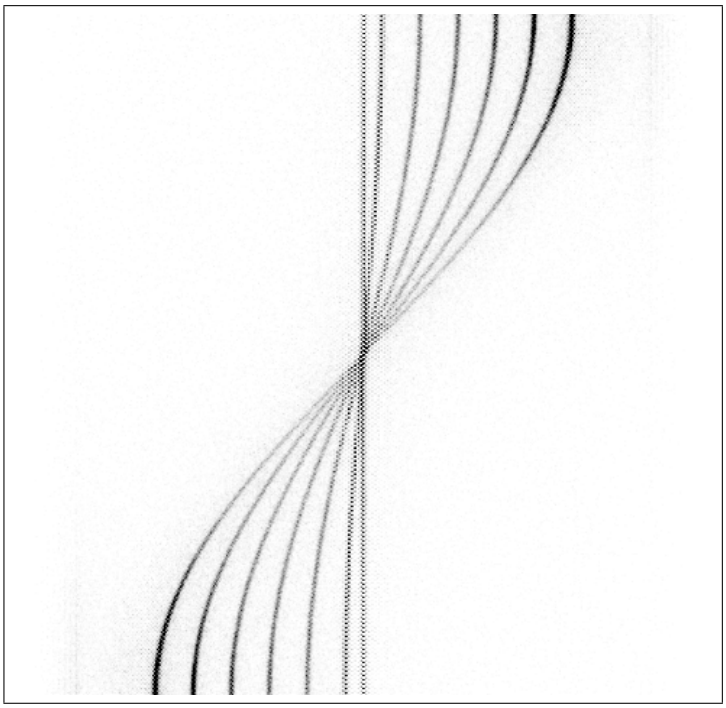

(a) Stationary gantry

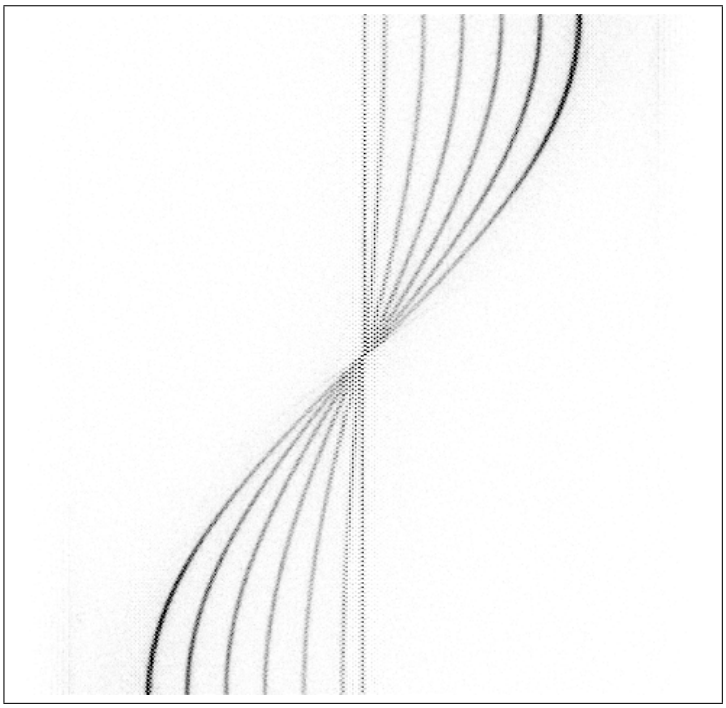

(b) Rotating gantry

Figure 6.1: Oversampled sinograms which have been produced by scanners (a) with a stationary gantry and (b) with a rotating gantry

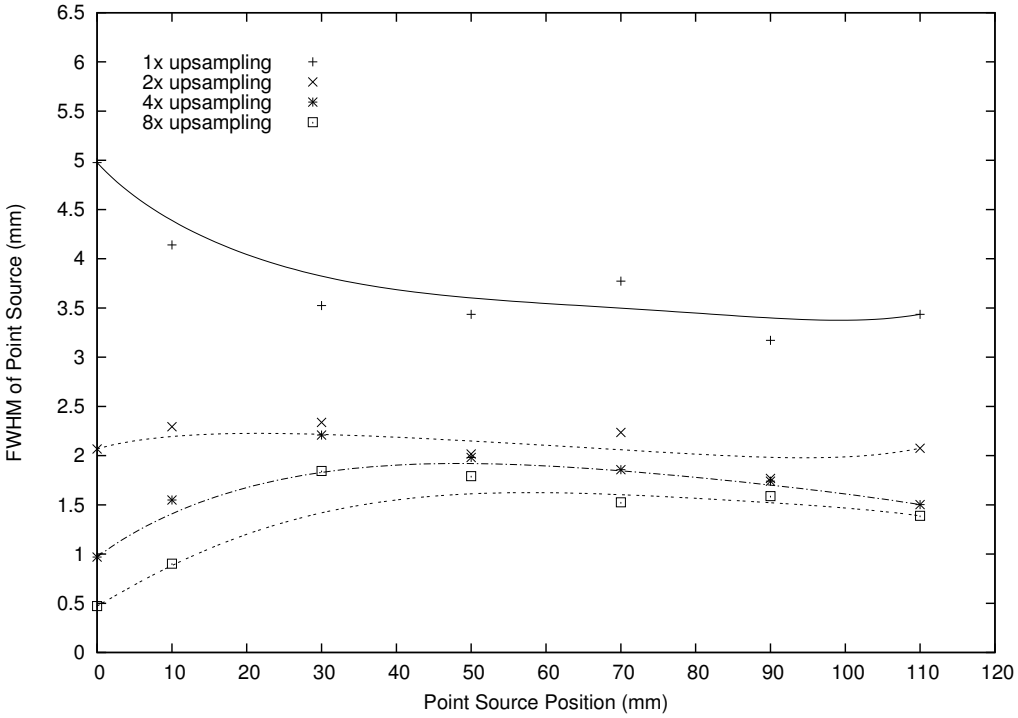


Figure 6.2: The effect of upsampling on the resolution of sources across FOV for an 8 layered scanner

to the data using the gnuplot graphing package. The smooth beziers pass directly through both the first and final data point while drawing a smooth curve between those points.

An upsampling factor of 4 provides relatively uniform PSF results across the FOV which is a suitable compromise between improvement in the resolution and minimisation of image reconstruction artefacts. An upsampling factor of 8 improves the resolution by approximately 25% but results in significant reconstruction artefacts at the centre of FOV (see Figure 6.3(d)). Therefore, an upsampling factor of 4 is considered optimal and all future sinograms processed in this study have utilised this upsampling factor.

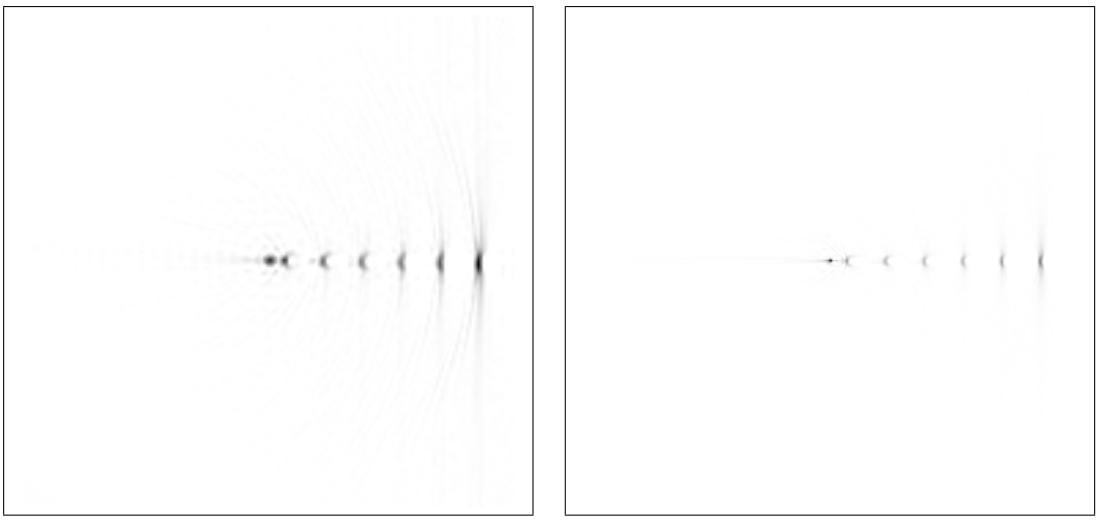

(a) 1 × upsampling

(b) 2 × upsampling

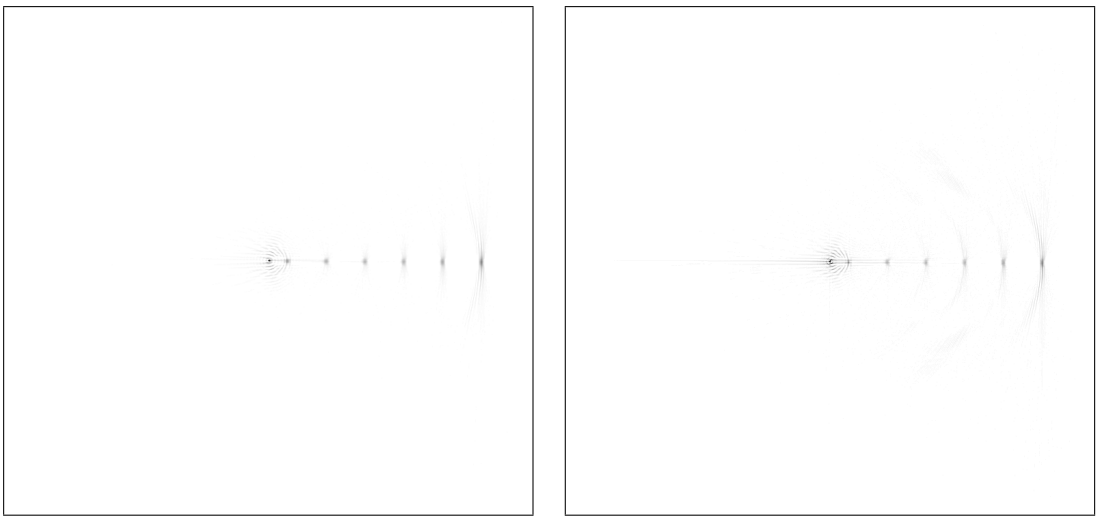

(c) 4 × upsampling

(d) 8 × upsampling

Figure 6.3: The effect of upsampling the sinogram in image reconstructions for a common data set

Binning a sinogram using the cartesian coordinate method, as discussed in Section 4.9.5, allows elimination of factors inherent to the scintillator crystal geometry and demonstrates the fundamental limits due to physical laws and the sinogram binning method. As the positron range and Compton scatter are identical for a given data set, changes in the resolution of the reconstructed point source can be attributed as a result of the binning method. Cartesian coordinate data was obtained from the same simulation as previously stated and Figure 6.4 shows the PSFs across the FOV for various upsampling factors. Selecting an upsampling factor of 8 results in the best performance as the greatest accuracy is retained for the lines of response. The PSF performance, however, does not continue to linearly improve with upsampling factor as the positron range and Compton scatter factors become prominent. In F-18 studies, the resolution limit for small animal PET investigations is currently below 1 mm, however the blurring due to the positron range results in a degradation in the resolution of between 0.1 and 0.2 mm full width half maximum (FWHM) [22] [21].

There is significant improvement in PSF at the centre of the FOV as the upsampling factor increases. However, this improvement is not noted as a result of the added DOI information gained by increasing the upsampling factor, rather, as a result of increasing the dimensions of the sinogram. As the sinogram dimensions increase, the physical space represented by each pixel becomes smaller. Using an upsampling factor of 1 results in each sinogram pixel representing a physical area of approximately $5mm^2$ in the transaxial plane whereas this decreases to 0.31 $mm^2$ for an upsampling factor of 8. Hence, for lower upsampling factors, regardless of the ability of the scanner to accurately measure LORs, the upsampling factor and sinogram dimensions appears as the limitation in resolution. Manual determination of the sinogram dimensions, independent of the upsampling factor is an improvement to the sinogram binning application considered in Section 7.1.14.

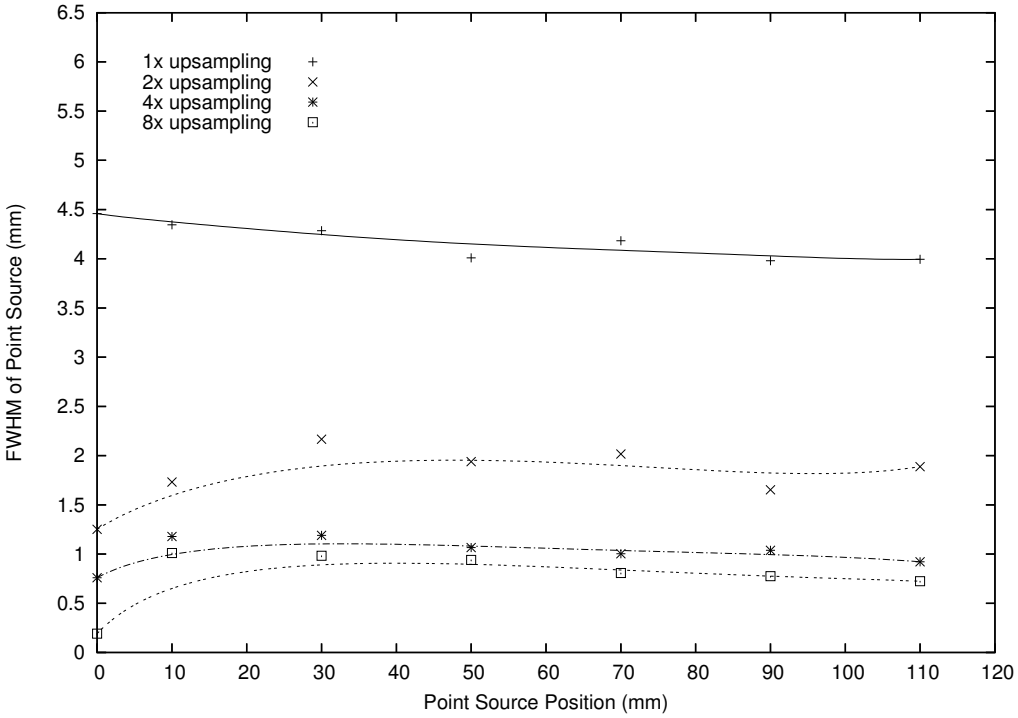


Figure 6.4: The effect of upsampling on the resolution of point sources across FOV using cartesian coordinate data

The cartesian coordinate binning process yields significantly improved performance to the detectorID method suggesting that having smaller crystals can allow a higher upsampling factor for the data, an area investigated in greater detail in Section 6.7.

## 6.3 Monlithic Crystal versus Segmented Crystal

Current PET scanners rely on long crystals in order to maintain high sensitivity within the detection system. A typical example is the module proposed by Casey et al. [27] utilising a $4 \times 8$ array of 30 mm deep BGO crystals. The newly proposed module with 8 crystal layer detector maintains high sensitivity by having a 24 mm crystal depth while providing the DOI information through the 8 layers of

segmented crystals. It is important to note that segmentation of the crystals does not automatically provide DOI, a method of identifying the crystal element in which the interaction takes place is required. Novel techniques which can be used to determine this and hence measure DOI have been presented in Section 2.9.

In order to quantify the improvement in spatial resolution from an 8 crystal layer detector compared to the more traditional monolithic crystal detector, point sources were placed at the same positions as in previous simulations with the PSFs analysed. The sinogram binning application utilised the same data set for both studies, however rebinned the data from the segmented crystal study into a monolithic crystal model as discussed in Section 4.9.2. Sinograms from the multiple layers of crystal and rebinned monolithic crystal studies are shown in Figure 6.5. As seen, having a single layer of DOI data results in the data towards the edge of field of view being "smeared", thus causing significant radial elongation. Figure 6.6 shows a reconstructed image using a monolithinc crystal detector with the radial elongation artefact clearly visible towards the edge of the field (the left most source is at the centre of FOV). Figure 6.7 shows a reconstruction using 8 layers of crystal for the same simulation demonstrating that DOI information assists in the reduction of the radial elongation artefact.

As the monolithic study data is simply the 8 layer data rebinned into a single layer, the number of counts for a given source is the same for both final image reconstructions shown in Figure 6.6 and Figure 6.7. As the radial elongation artefact "smears" the reconstructed point source over a larger area, there is a decrease in the brightness of this source that is clearly evident in the sources at the edge of FOV.

The sinogram binning application also rebinned the data in order to make the scanner appear to have 2 layers of crystal and 4 layers of crystal using the method described in Section 4.9.2. This was undertaken to illustrate the improvements that can be offered simply by increasing the DOI information available. The PSFs

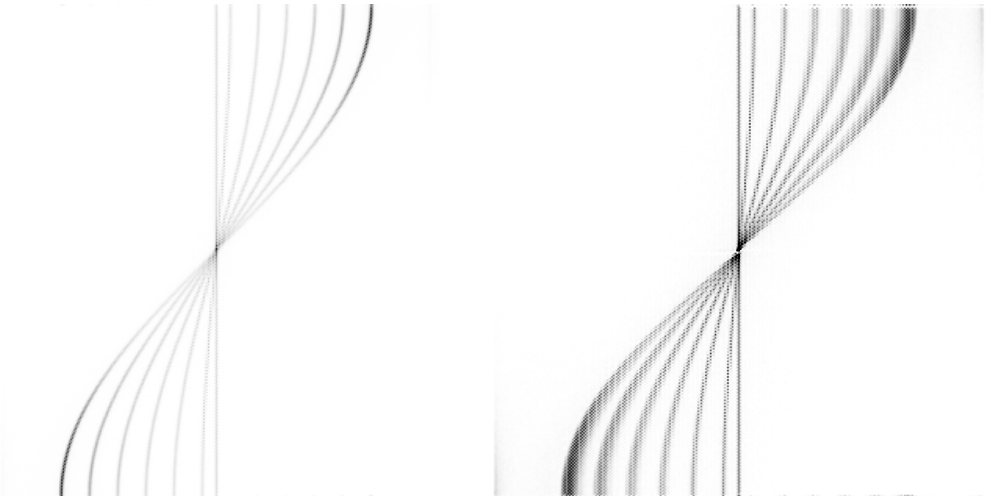

(a) 8 layers of DOI information

(b) 8 layer data rebinned into 1 layer of DOI information

Figure 6.5: A comparison of the 8 layers of DOI data versus the 8 layers rebinned into 1 layer of data. For the 8 layers of data rebinning into a single layer, the DOI uncertainty becomes evident in the sources moving away from the centre of the FOV. Significant blurring is observable in the traces within the sinogram with increasing effect away from the centre.

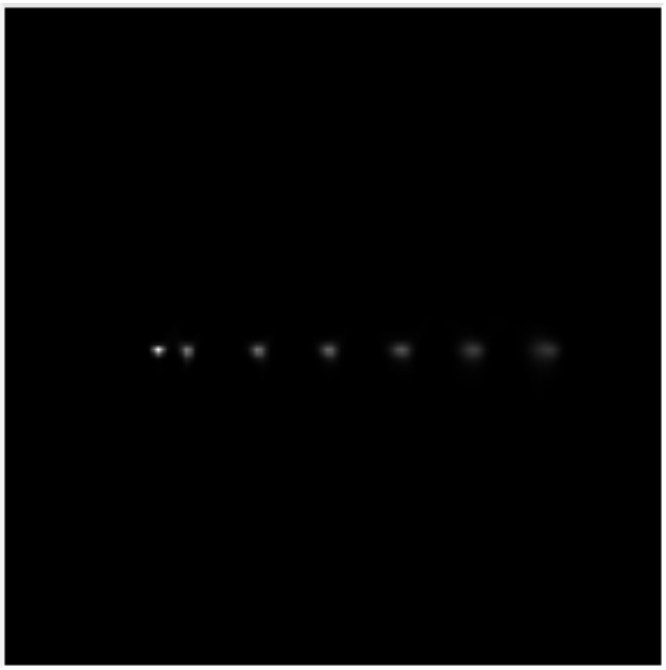

Figure 6.6: The radial elongation artefact seen in an image reconstruction for a detector system with a single layer of crystal

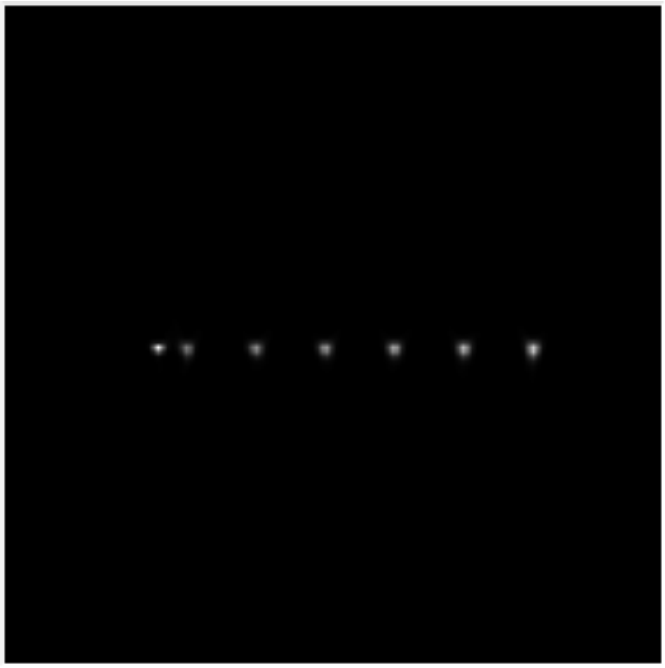

Figure 6.7: A reconstruction showing the lack of radial elongation when DOI information is available. The shape of the reconstructed sources appears approximately circular for the entire FOV and the elongation moving away from the centre of FOV seen in Figure 6.6 is not present

provided after varying the DOI information by adjusting the number of layers are shown in Figure 6.8. The cartesian coordinate reconstruction is also presented to show the limit of observability for the sinogram binning utilised with the data. At the centre of the FOV, there is very little difference between the reconstructions using the different number of DOI layers. This is as expected as there is no additional information gained by DOI for sources at the centre of FOV. As predicted, the radial elongation artefact degrades spatial resolution towards the edge of the FOV when DOI information is reduced. The 4 layer DOI system is comparable to the 8 layer system for approximately 140 mm of the 220 mm FOV. This suggests that for studies where the FOV required is 140 mm or less, a less electronically complex 4 layer detector module can be utilised. Where the FOV is smaller than 60 mm, each of the 1 layer, 2 layer, 4 layer and 8 layer systems demonstrate nearly identical performance. This result can be attributed mostly to the limitations in resolution

caused by the sinogram element size and the very small angle at which the incident photon creates with the normal face of the crystal (with the knowledge that the more normally incident the photon, the less significant the DOI information is). For a source which covers the central 60 mm, the most oblique direct photon from the source will strike the front face of the crystal with an angle of approximately 10°, an angle too small to fully utilise the DOI information available.

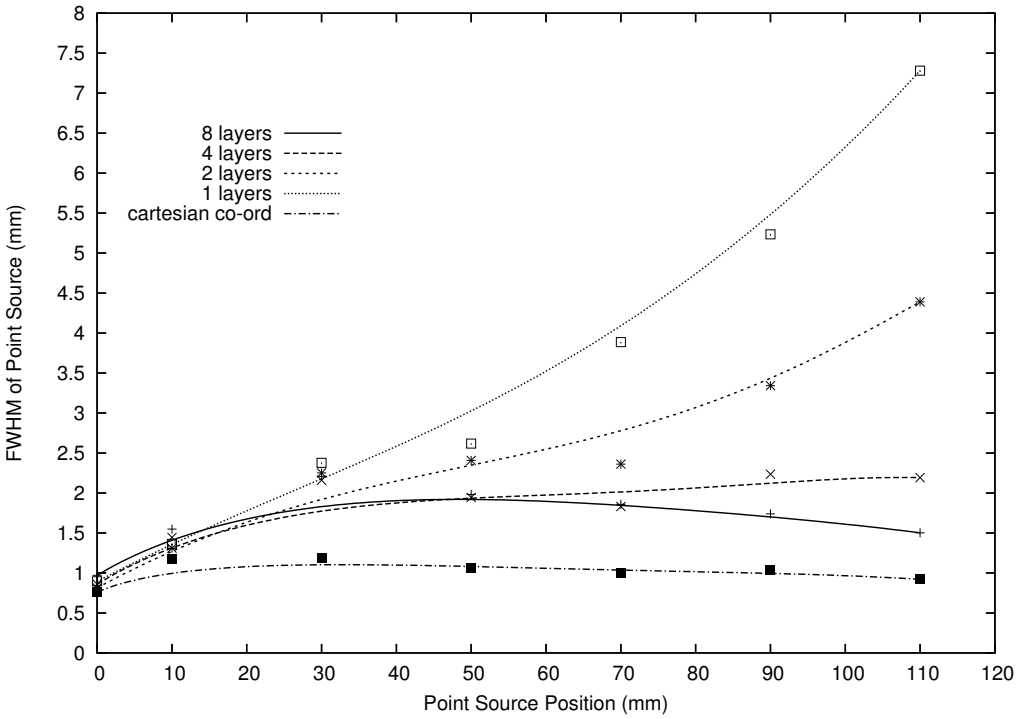


Figure 6.8: The FWHM of the point sources across the field of view for different numbers of DOI information layers

## 6.4 Simulation Efficiency

Transporting electrons and positrons in Monte Carlo studies can be very time consuming as these particles require numerous interactions in matter to deposit their

energy. Photons deposit their energy much faster and do not require as many interactions, resulting in significantly less computational time being required. GATE allows users to utilise approximations in order to decrease the simulation times, specifically in cases where the positron range is not of significance. Instead of a positron being emitted by the source and then travelling a finite distance before annihilation, the simulation directly creates two back-to-back annihilation photons from the source itself.

The suitability of this approximation is considered with a comparison of the PSFs across the FOV for studies using positron sources and back-to-back gamma sources placed in a water phantom shown in Figure 6.9. The lower level discriminator (LLD) and upper level discriminator (ULD) values were set to 350 keV and 650 keV respectively with a coincidence window of 10 ns. The data was binned into the sinogram using an upsampling factor of 8.

The positron range for Fluorine-18 creates a blurring of approximately 0.2 mm FWHM in the PSF, which is consistent with the data provided by Derenzo [56]. If the purpose of the Monte Carlo study is to verify characteristics of performance such as sensitivity or energy resolution, increased simulation speed can be achieved by using the back-to-back gamma sources. In instances where the positron range needs to be considered (eg. spatial resolution measurements), an additional blurring of 0.2 mm can be added to all spatial resolution measurements in order to eliminate the need redo the simulations with positron range included. If a more analytical approach to determining the effect of positron range is required, the positron range and the photon non-collinearity can be modelled within GATE for back-to-back gamma sources [11].

Furthermore, electron transport is not considered within any part of the work presented in this thesis further improving simulation speed. The above study was repeated with electron transport enabled with a range cutoff of 250 $\mu$m with the PSFs recorded being identical suggesting this approximation is suitable. The electron

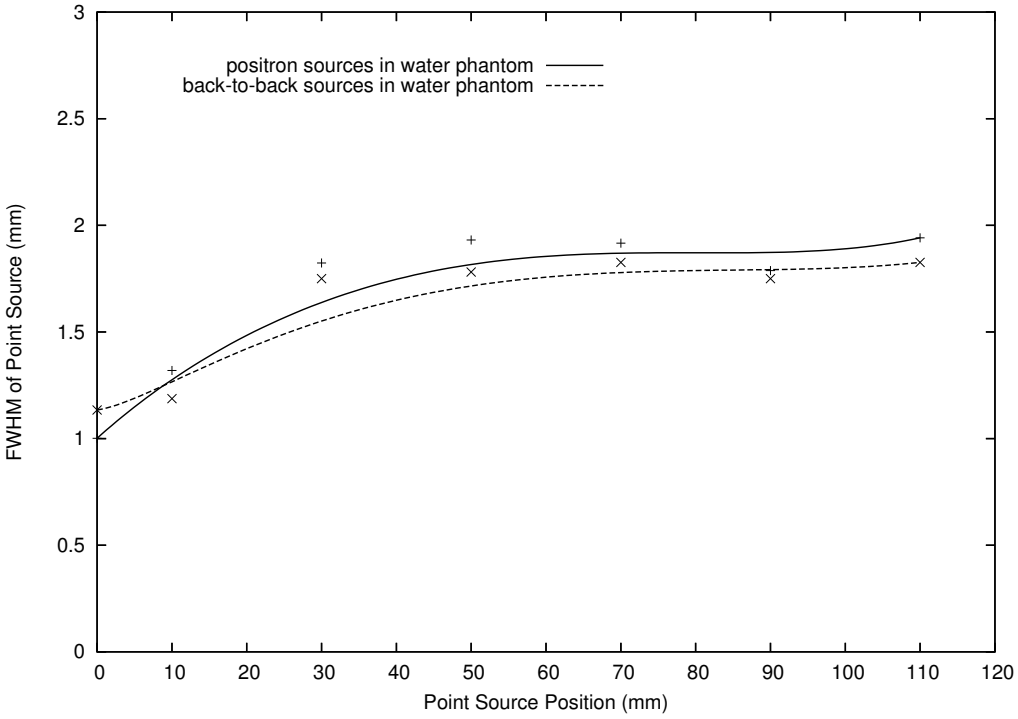


Figure 6.9: The FWHM of the point sources across FOV for positron and gamma sources

cutoff was selected based on the range in LYSO of a photoelectron with maximum energy from one of annihilation photons.

## 6.5 Effect of Phantom Scattering

As shown in Figure 2.5, photons often do not travel in a straight line from the source to the detector. Scattering within the body creates incorrect LORs and subsequently the wrong elements within the sinogram are incremented. The final result is noise which is present in the reconstructed image with a degradation in the PSFs of sources.

The effect of scatter originating from the phantom was investigated by placing identical back-to-back annihilation photon sources at the centre of FOV in both air and a 100 mm radius 100 mm long water phantom. Back-to-back photons have been used in this study for a number of reasons; firstly, the specified world volume in the GATE studies is a $50 \times 50 \times 50$ cm$^3$ air volume. As F-18 positrons have a mean range of approximately 1.8 m in air, they escape the world volume without annihilating resulting in faults within the Monte Carlo program and premature termination of the simulation. Secondly, only a comparison between the resolutions for simulations with the phantom, and without the phantom, is required, not the absolute spatial resolution results. Figure 6.10 shows the PSFs for sources placed in a water phantom and air. The LLD and ULD values were set to 350 keV and 650 keV respectively and an upsampling factor of 4 was used when binning the sinogram. As Figure 6.10 demonstrates, there is a significant improvement in the PSFs when the scatter component of the study is reduced. By reducing the scatter component, the contrast, as well as the resolution, can also be improved making lesion detection easier [57]. Numerous techniques have been developed, however a single accepted method which has demonstrated superior performance for all applications has yet to be produced and scatter correction remains an area of active research.

A total elimination from scatter analytically within a study is not possible due

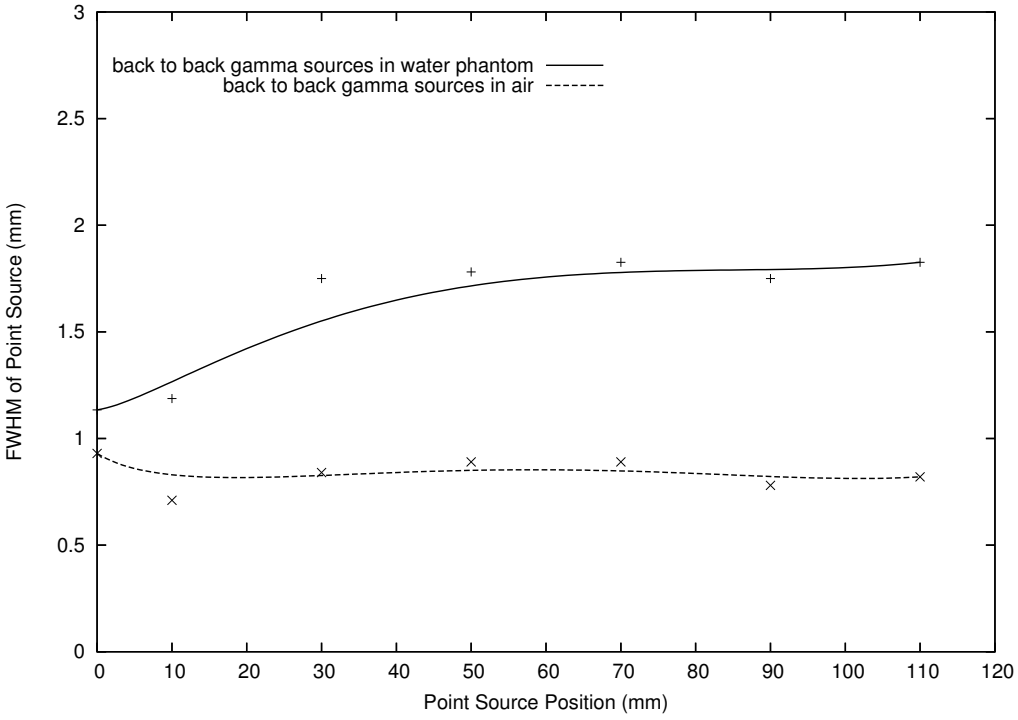


Figure 6.10: The spatial resolution across FOV for back-to-back gamma sources in a water phantom and air

to the random nature of scatter hence this study simply demonstrates the capability of the scanner in the best case scenario without scatter. However, the significance of scatter reduction has been demonstrated.

## 6.6 Changes in Sensitivity and Resolution Related to Changes in the Energy Window

The sensitivity of a PET scanner is a significant parameter when considering design optimisation. Three major factors are pertinent when considering the sensitivity; the solid angle that the detector rings represent to the sources within the FOV, the type and thickness of scintillator crystal in which $\gamma$-rays can interact and the energy window within which coincidences are allowed.

The solid angle of detector can be increased by having a large detector packing fraction and furthermore by increasing the number of detector rings in the axial direction. The scintillator crystal can be made thicker in order to detect more incoming photons however the lack of DOI becomes a limiting factor as does the cost of the added crystal. The type of scintillator crystal used determines the speed of the light pulse effects the amount of dead time due to the pile-up effect.

The ability to locate items of interest reduces significantly as the amount of scatter in a PET scan increases, the "haze" caused by scatter can mask low activity volumes within it. In order to reduce the amount of scatter contribution to the reconstructed image, the energy window in the data acquisition system is set commonly between 350 and 650 keV. The Compton edge for 511 keV annihilation photons is 340 keV suggesting most measured photons have not scattered within the body before being recorded. However, the energy resolution of the scanner is not infinite therefore uncertainty exists about the actual energy of the photon resulting in photons below the threshold being accepted. The CMRP has presented data on the energy resolution of a photodiode coupled to LYSO in a previously published study, showing an energy resolution of approximately 13% FWHM at 511 keV [58].

This percentage changes depending on the energy however at 340 keV, 13% represents approximately 45 keV suggesting photons with energies below 300 keV can get accepted.

Ideally, an energy window accepting only 511 keV photons could be used to reduce the amount of recorded scatter, however the reduction in the sensitivity of the scanner would make acquisitions prohibitively long. Conversely, fast acquisitions can be undertaken with larger energy windows with the LLD set to values less than 350 keV, at the expense of scatter acceptance.

In most clinical sensitivity studies, a point source (or approximate point source) of known activity is placed inside a small metallic sleeve at the centre of the FOV. The metallic sleeve is to ensure all positrons annihilate at the centre of the field of view. An acquisition is undertaken for a fixed period of time and by counting the number of measured coincidences versus the decay corrected source activity, the sensitivity of the scanner can be calculated. To maximise the speed of the sensitivity measuring simulation, a back-to-back gamma emitting isotropic source of activity 10 MBq was placed at the centre of the FOV. The percentage of coincidences measured by the scanner with respect to the number of emitted photon pairs by the source for varied LLD values and crystal sizes is shown in Figure 6.11.

As the LLD value is increased, a greater number of coincidences are rejected. These coincidences contain photons that are scattered within the body and do not have enough energy to be above the LLD, or contain photons which only partially deposit their energy within the scintillator, again falling below the LLD. Additionally, as the crystal size becomes smaller, scatter within a crystal becomes a more significant factor. Often, photons will scatter multiple times within a single crystal, creating multiple energy depositions before finally being photoelectrically absorbed. The scanner detects this very fast process as single deposition as the pulses of light originate from a single crystal with the timing resolution not allowing the observation of each energy deposition. As the crystal size is decreased, the scattered

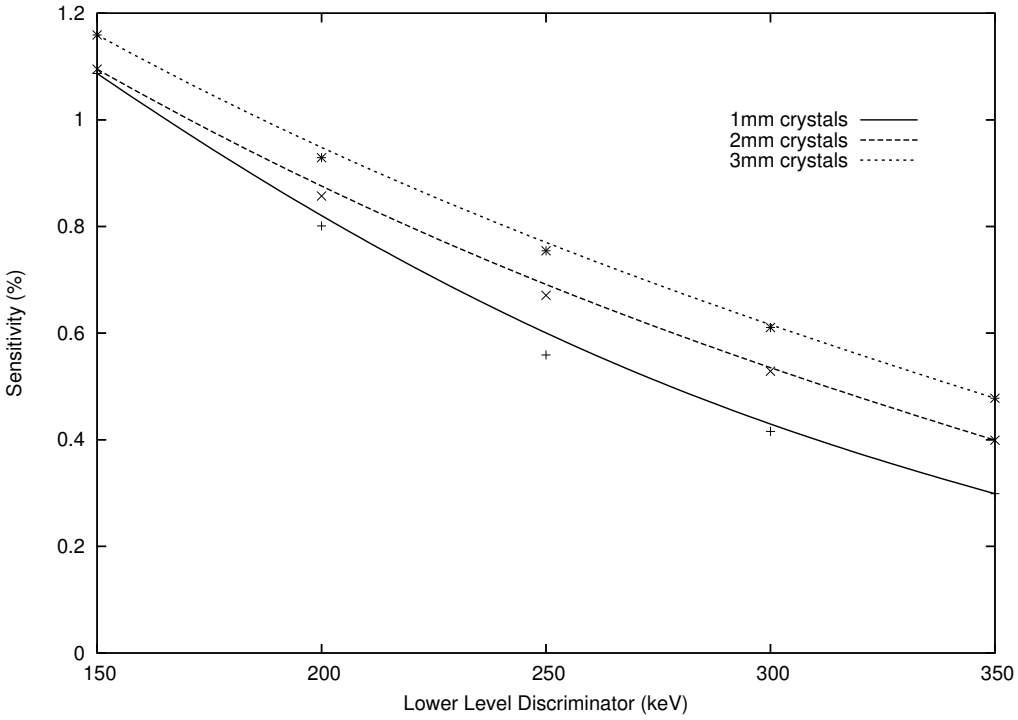


Figure 6.11: The sensitivity of the scanner for different LLD values and crystal sizes

photons start travelling out of the crystal and into adjacent crystals and modules. The scanner is programmed to reject counts from adjacent modules and furthermore, only accepts depositions above the LLD value and hence these photons are ignored. Subsequently, as the crystal size is decreased, the sensitivity of the scanner also decreases.

In order to investigate the effect of changing the LLD value on the PSFs, positron sources were placed in the FOV at the centre of FOV, 10 mm, 30 mm, 50 mm, 70 mm, 90 mm and 110 mm off centre, inside a 120 mm radius, 100 mm long cylindrical water phantom. The LLD was then varied from 150 keV to 250 keV and finally 350 keV. The PSFs of the reconstructed point sources across the FOV are shown in Figure 6.12. This result is contrary to what is expected; As the LLD value is reduced, the resolution of the reconstructed images appear to improve. The reason for this was not understood until the scatter contribution and the total number of counts fron the body was also studied. One of the advanced features of the sinogram binning application enables the percentage of scattered photons from the body to be determined with respect to the total number of photons. Furthermore, the total number of coincidences can also be counted. The amount of scatter from the body can be determined according to Equation (4.20) and is shown against the LLD in Figure 6.13.

As the LLD value decreases, there is an increase in the relative amount of scattered photons to true photons as measured by the scanner. At the same time, there is a significant increase in the number of counted coincidences as illustrated by Figure 6.14. Increasing the amount of data recorded by making the energy window larger results in an improvement in the resolution, not because of improved scanner performance but simply improved statistical certainty and an increase in the signal to noise ratio (SNR). The majority of the low energy photons recorded by the scanner in this study are not ones which have scattered within the phantom, rather they

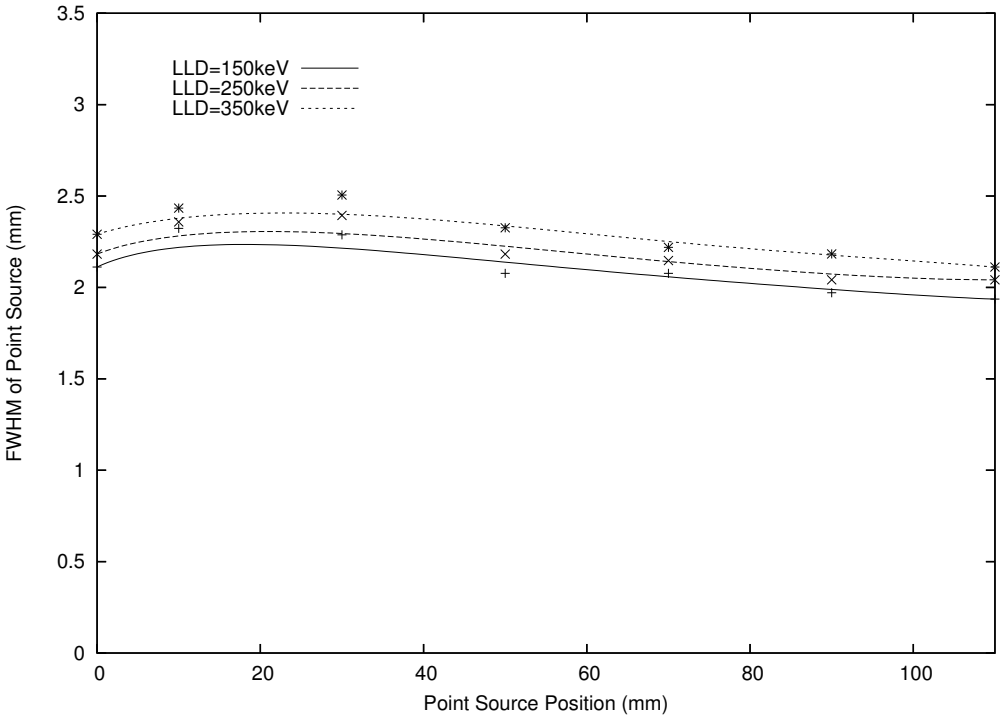


Figure 6.12: The PSFs across FOV for different LLD values

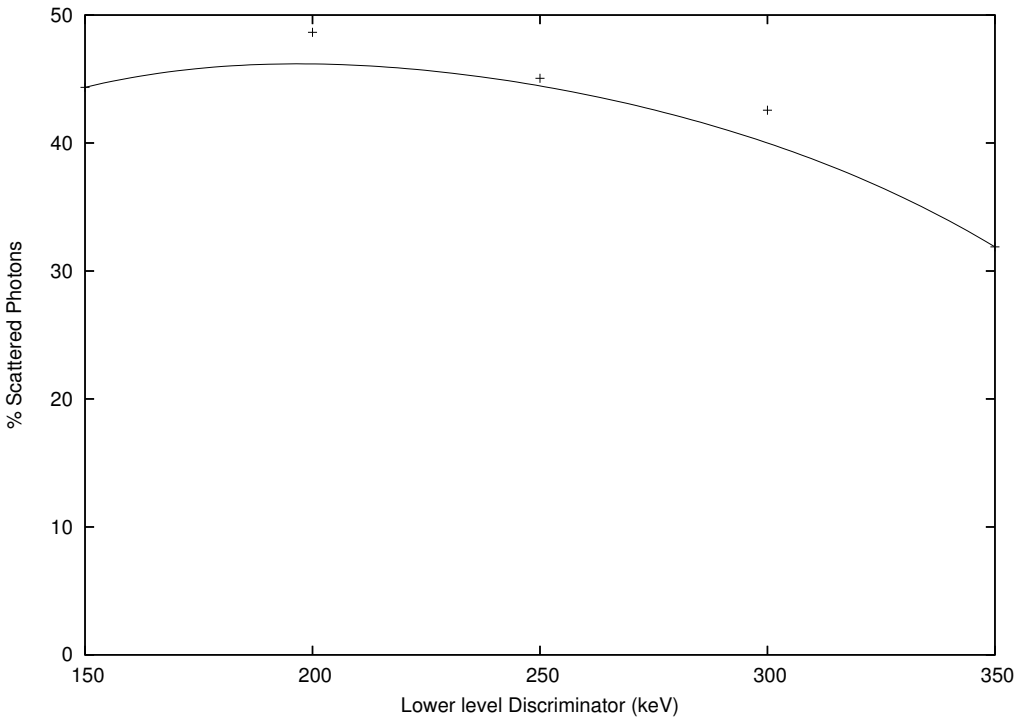


Figure 6.13: The percentage of photons which have been scattered within the phantom for different LLD values

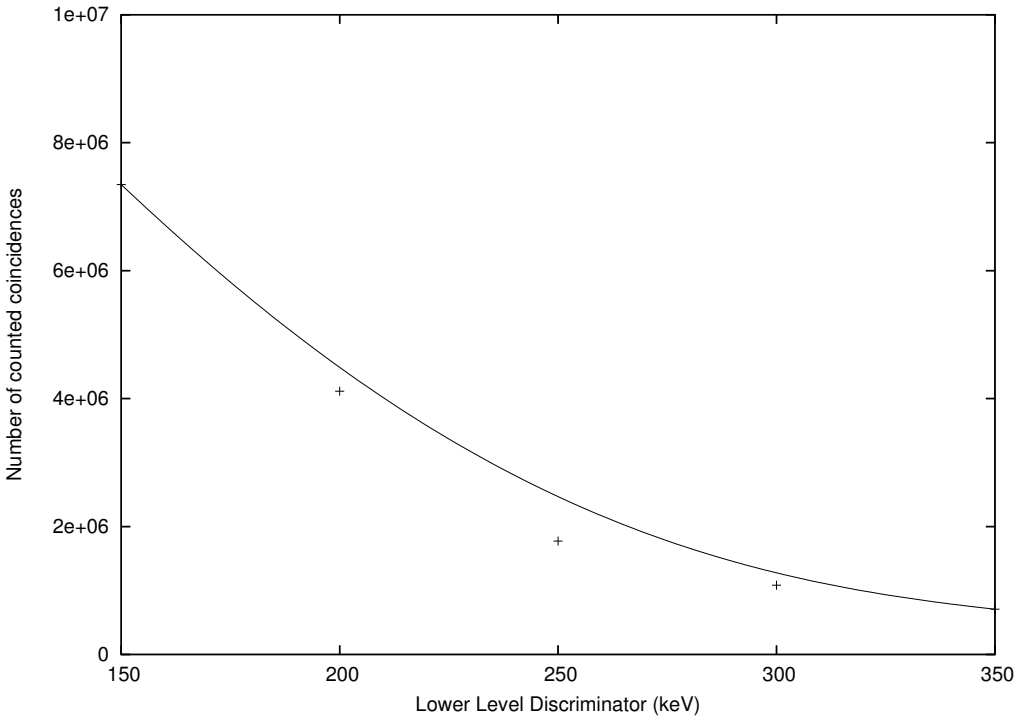


Figure 6.14: The total number of coincidences recorded for different LLD values

Compton scatter and deposit a small amount of energy within the scintillator crystal itself, hence the increase in the SNR. Any predicted decrease in the resolution due to increased scatter is offset by this improved SNR.

This study shows significant limitations with the representation of a real life system using GATE when powerful computing resources are not available. Nevertheless, optimising the energy windows for this detector geometry is an extremely important aspect that needs to be considered as an are for future investigation.

## 6.7 Sensitivity and the Crystal Cross Section

As mentioned in Section 2.8, the spatial resolution of a scanner can be theoretically improved by making each crystal element smaller. Limitations exist as decreasing crystal size results in increased complexity in the electronics, higher cost,

more dead space, relatively poor SNR per volume as well as the fundamental limits in PET resolution. Nevertheless, if the improvement offered by decreasing the crystal size is significant, it must be considered as an alternative.

Comparison between using $3 \times 3 \times 3$ mm$^3$, $2 \times 2 \times 2$ mm$^3$ and $1 \times 1 \times 1$ mm$^3$ crystal elements in the detector module was performed in GATE. The total radial depth of the crystals was retained at 24 mm in order not to affect the sensitivity of the scanner by having 12 layers of crystal for the $2 \times 2 \times 2$ mm$^3$ crystals and 24 layers for the $1 \times 1 \times 1$ mm$^3$ crystals. As the crystal size decreases, the width of the detector module also reduces and a greater number of detector modules can be placed around the ring; 314, 470 and 940 detector modules for the $3 \times 3 \times 3$ mm$^3$, $2 \times 2 \times 2$ mm$^3$ and $1 \times 1 \times 1$ mm$^3$ crystals respectively. An upsampling factor of 2 was selected for all three studies in order to minimise the effect of zero efficiency bins within the sinogram and furthermore to reduce the reconstruction time required. An upsampling factor of 4 when considering the 940 detector module scanner results in a sinogram with dimensions $1880 \times 1880$ pixels.

The PSFs for positron emitting point sources across the FOV for the different crystal sizes is shown in Figure 6.15. A greater number of detector modules around the detector ring provides a higher number of possible LORs resulting in improved resolution. However, as the crystals are further reduced in size from $2 \times 2 \times 2$ mm$^3$ to $1 \times 1 \times 1$ mm$^3$, the improvement is far more limited. This is due to the fundamental limit of resolution for the scanner, with factors such as the positron range becoming significant [22] [21]. Increasing the upsampling factor for this study does provide improved PSFs however at the expense of prohibitively long reconstruction times for the $1 \times 1 \times 1$ mm$^3$ crystal study.

Another factor which becomes significant with reduced crystal size is related to the separation between modules in which a coincidence can be recorded between. The GATE simulations allow a minimum module span between which coincidences are not recorded. This value has been set at 9 detector modules for all studies.

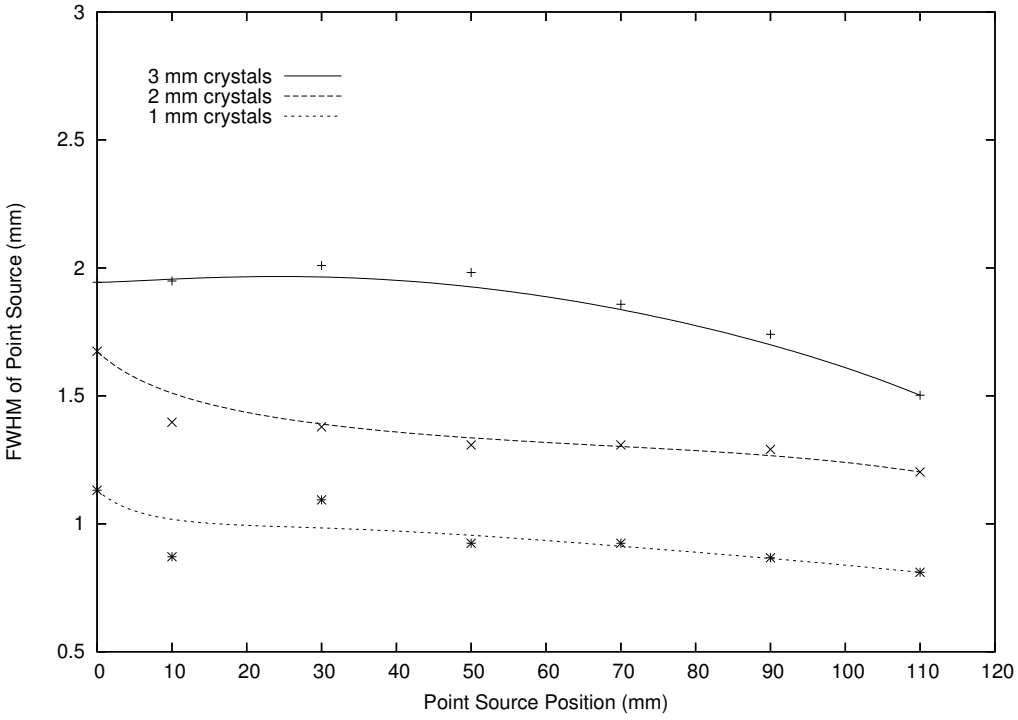


Figure 6.15: The spatial resolution across the FOV for $3 \times 3 \times 3$ mm$^3$, $2 \times 2 \times 2$ mm$^3$ and $1 \times 1 \times 1$ mm$^3$ crystal elements

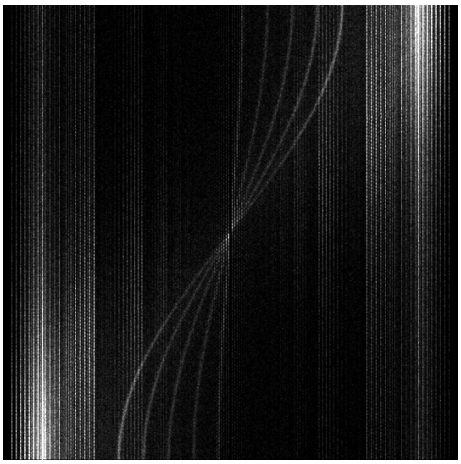

Figure 6.16: A sinogram showing inter module scatter

As the crystal size becomes smaller, the width of each module decreases as does the physical separation between 9 detector modules. This increased proximity can result in more scatter between adjacent modules as illustrated in Figure 6.16. Note the bright areas towards the edges of the sinogram which illustrate the coincidences recorded between adjacent detector modules. This sinogram is from a study with the LLD set to 150 keV.

## 6.8 Spatial Resolution with Different Isotopes

The radioisotope selected for clinical use is often dependent on the type of study required with approximately 90% of clinical PET studies currently using FDG. The remaining 10% consists of studies using other isotopes including oxygen-15 and carbon-11.

As mentioned previously in Section 2.7.3, the positron range is a significant limitation on the resolution of a PET scanner with each isotope creating positrons with unique emission energy spectra. An increased mean positron kinetic energy results in a larger positron range and hence a higher intrinsic spatial resolution limit for the scanner. If it is known that a scanner will be used exclusively with a specific isotope, it is possible to design the scanner in a way which takes the intrinsic limits

into consideration.

Commonly used PET isotopes, with their mean positron ranges, are shown in Table 2.1. The mean positron ranges of carbon-11 and oxygen-15 are 1.1 mm and 2.5 mm respectively, significantly higher than F-18 (0.6 mm). The F-18 sources were replaced with C-11 and O-15 sources in two separate studies. The sources were placed across the FOV in the same positions as all of the previous studies. The PSFs of the reconstructed images were investigated for three different detector geometries: 940 detector modules containing $1 \times 1 \times 1$ mm$^3$ crystals, 470 detector modules containing $2 \times 2 \times 3$ mm$^3$ crystals and 314 detector modules containing $3 \times 3 \times 3$ mm$^3$ crystals. The sinograms were binned with an upsampling factor of 2 to minimise the effect of zero efficiency bins and to provide parity between the different crystal sizes.

The reconstructed PSFs of the point sources across the FOV for C-11 and O-15 are shown in Figure 6.17 and 6.18 respectively. The positron range for each isotope is also shown. As the positron range increases, the intrinsic resolution of the scanner becomes poor and reduction of the crystal size does not further improve resolution. When compared to the F-18 studies with lower positron energies, the resolution of the scanner is significantly reduced.

## 6.9 Realistic Detector Module

Up to this point, all simulations have been carried out using an ideal detector geometry. That is, dead space within the detector modules has not been considered resulting in an increased detector packing fraction. The detector geometry can be modified to more accurately model the prototype modules being used in experimental characterisation.

The scintillator crystals are optically isolated from each other using optical paint and placed on a printed circuit board. The thickness of the paint and PCB, as well as the manner in which the way the crystals are mounted with 1-to-1 coupling with

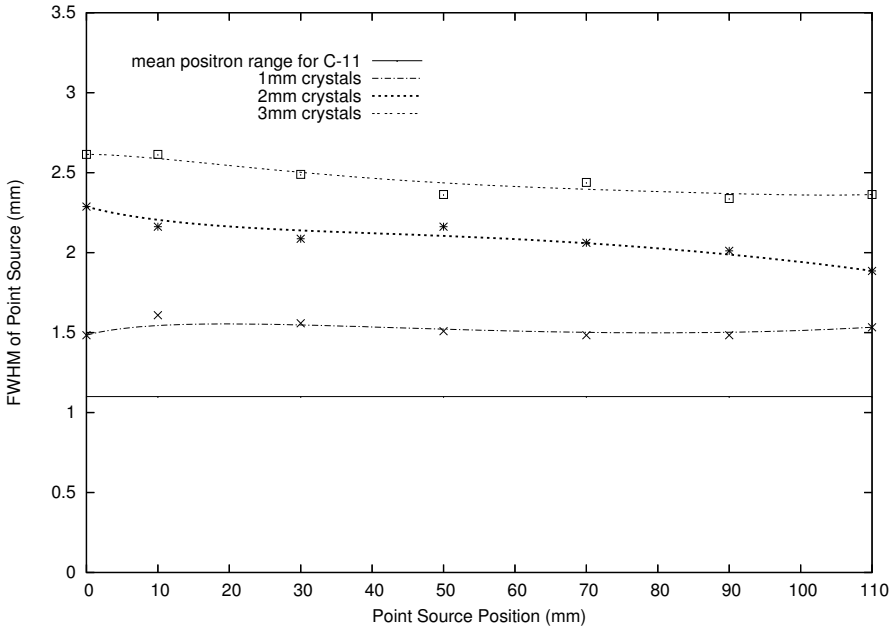


Figure 6.17: The spatial resolution across the FOV for carbon 11

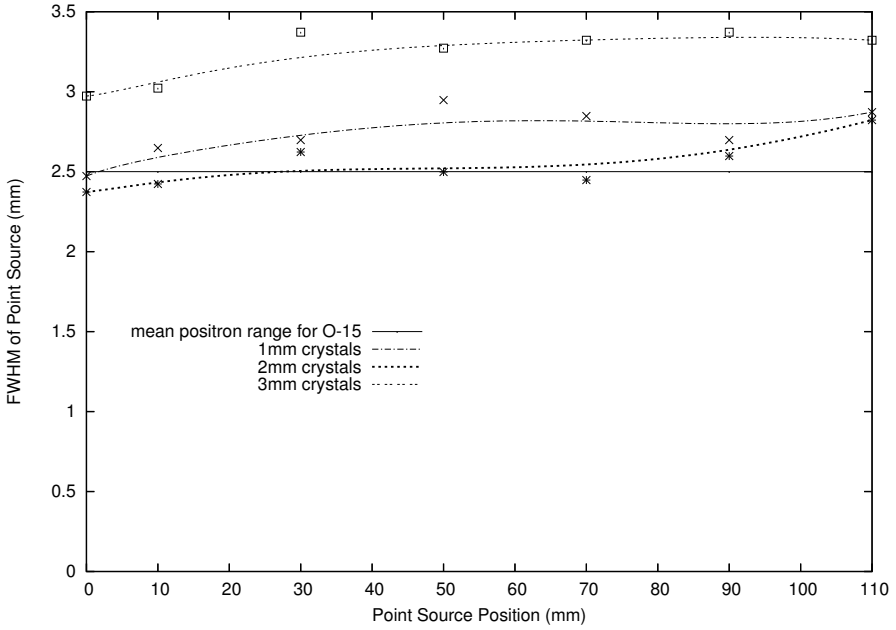


Figure 6.18: The spatial resolution across the FOV for oxygen 15

the photodetectors, causes the crystal pitch to increase from 3 mm to 3.5 mm. This is a relatively pessimistic value for the actual pitch and is used to show the performance with the least miniaturised electronics and packing. The carrier for the scintillator crystals and photodetector is modelled as a 0.5 mm thick plastic volume underneath the scintillator crystals. A single detector module within the GATE study is shown in Figure 6.19. The outline of each crystal is displayed in green while the crystal itself is shown blue and the carrier is shown in red. In a full study, 268 of the modules can be placed around the ring whereas 314 detector modules are possible if dead space is neglected as in the previous investigations.

The reduced number of detector modules leads to a decrease in the number of possible LORs which naturally results in reduced spatial resolution. A comparison between the 3 mm crystal pitch resolutions and the 3.5 mm pitch data as shown in Figure 6.20 for a data set acquired with an energy window of 350-650 keV and a coincidence windown of 10ns. The data was binned with an upsampling factor of 4. The decrease in the resolution is on average 14%, comparable to the 14.6% decrease in the number of detectors within the ring. Further investigation of the relationship between the number of detector modules in the ring and the resolution is considered in Chapter 7.

## 6.10 Resolving Power for Sources separated by 3 mm, 2 mm and 1 mm

The PSF of a reconstructed point source is one measure of spatial resolution in a clinical environment. In most clinical studies however, the areas of interest with high uptake are often surrounded by other radioactivity, or individual hotspots are separated by small distances. Significant importance is placed on being able to distinguish these small volumes independently of each other. In this study, a number of small sources were placed at the centre of the field and the ability to independently identify them was observed. Sources were placed at the centre of

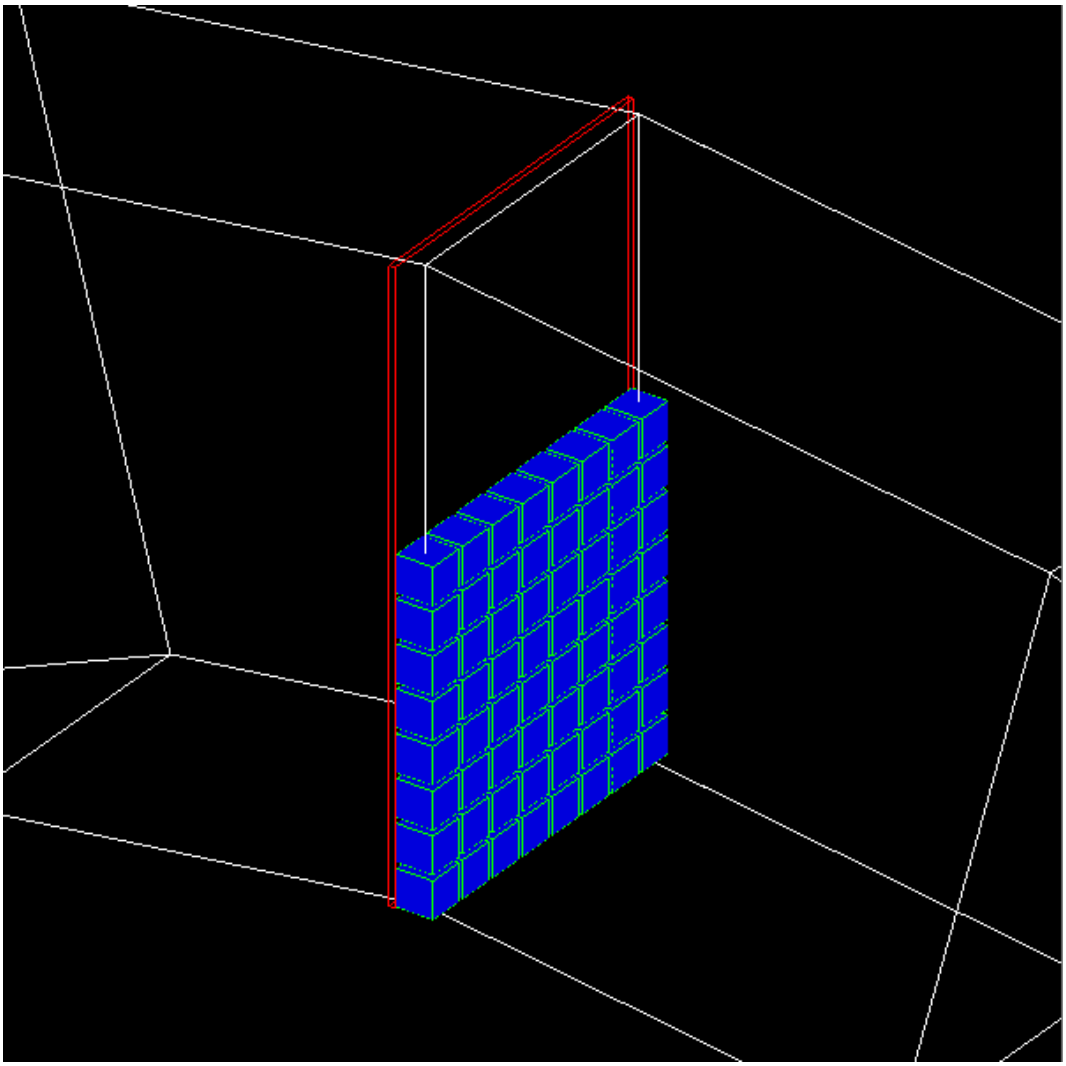

Figure 6.19: A realistic detector module in GATE showing the dead space between crystal elements

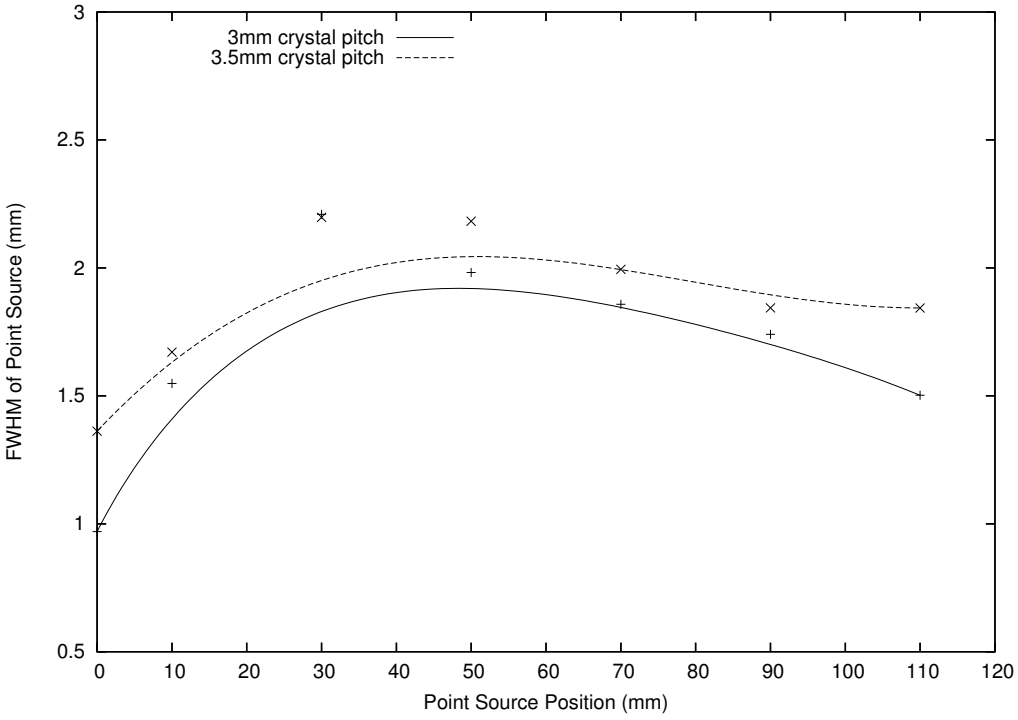


Figure 6.20: The spatial resolution across the FOV for crystals with 3 mm and 3.5 mm pitches

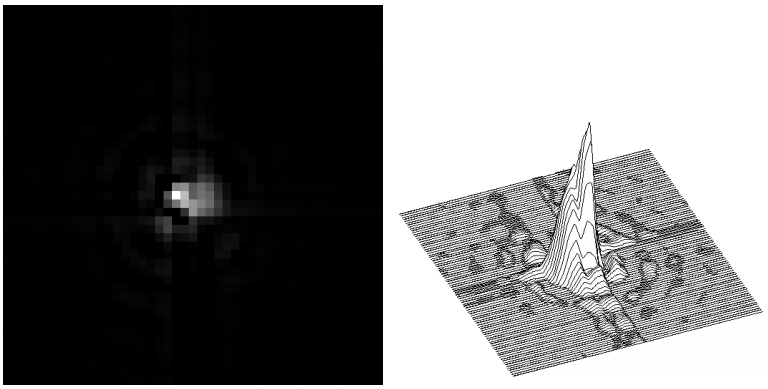

(a) Sources separated by 1 mm

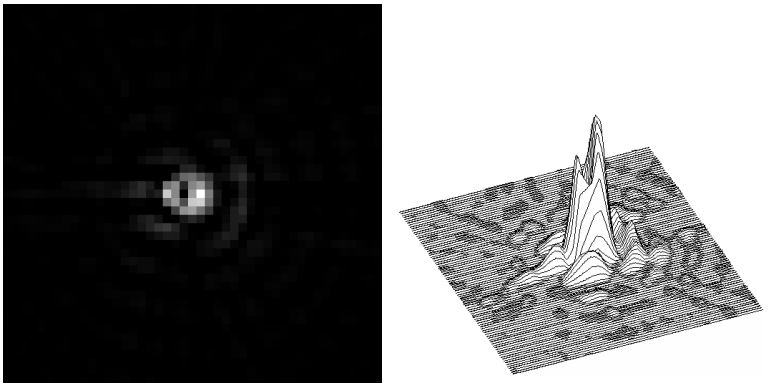

(b) Sources separated by 2 mm

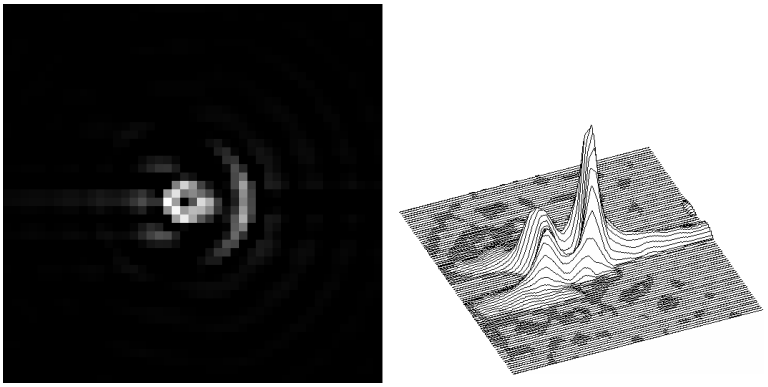

(c) Sources separated by 3 mm

Figure 6.21: Reconstructed images of two point sources separated by a small distance and the surface plots of each reconstruction illustrating the peaks

FOV (0,0,0 mm in the world volume) and also at (1,0,0), (2,0,0) and (3,0,0) mm in 3 separate studies.

Reconstructed images using the 8 layers of DOI data and 4× upsampling for the sources separated by 1 mm, 2 mm and 3 mm are shown in Figure 6.21.

Figure 6.22(a) indicates that sources separated by 1 mm cannot be resolved by this scanner. Figures 6.22(b) and 6.22(c) show independent sources, however image reconstruction artefacts due to oversampling are present as well, resulting in uncertainty in the identification of the sources. Use of an iterative reconstruction algorithm may enable these point sources to be better resolved without significant image artefacts.

This study was repeated for the sources placed off centre, 70 mm from the centre of the FOV with the reconstructed sources and the surface plots shown in Figure 6.22. These sources exhibit superior reconstructions with less artefact than the sources placed at the centre of FOV shown in Figure 6.21. The study with the 3 mm separation between sources clearly shows independent sources while the surface plot from the 2 mm separation study illustrates independent sources.

If cartesian coordinate sinogram binning is performed, a more accurate sinogram is built and the ability to resolve the two sources at the centre of the FOV is improved as shown in Figures 6.23(a), 6.23(b) and 6.23(c). For both the 2 mm and 3 mm separation, the two sources are distinctly identifiable, albeit slightly distorted.However, the sources separated by 1 mm are still not independently identifiable.

## 6.11 8×8×1 detector block vs 8×8×8 detector block

The arrangement of the detector modules within the ring can affect the detection sensitivity, resolution and electronic complexity of the scanner. The proposed module in this study contains 8 crystals in both the radial and axial directions and 1 in the tangential ($8 \times 8 \times 1$) resulting in an "edge on" orientation. A "face on" orientation is also possible resulting in a detector block which contains $8 \times 8 \times 8$ crystals per module. The edge on and face on orientations are shown in Figures 6.24 and 6.25 respectively.

Forty $8 \times 8 \times 8$ detector modules can be placed around the 300 mm diameter detector ring. The amount of dead space between detector modules for the

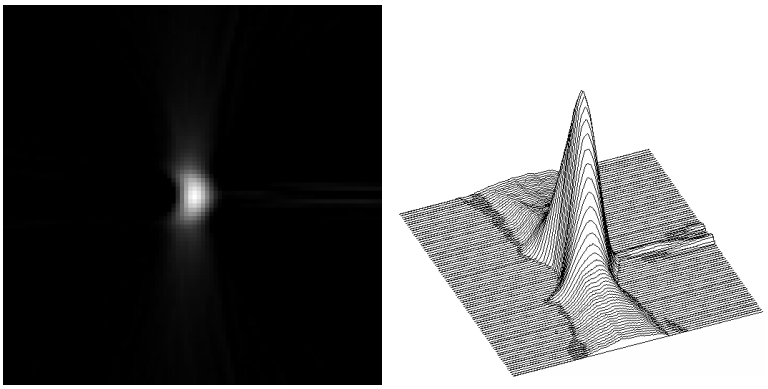

(a) Sources separated by 1 mm

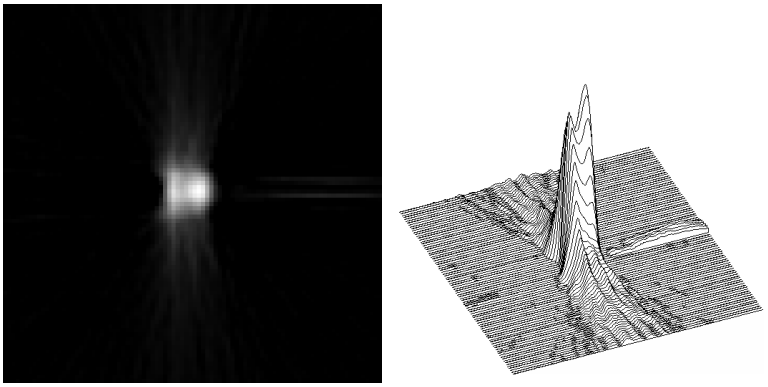

(b) Sources separated by 2 mm

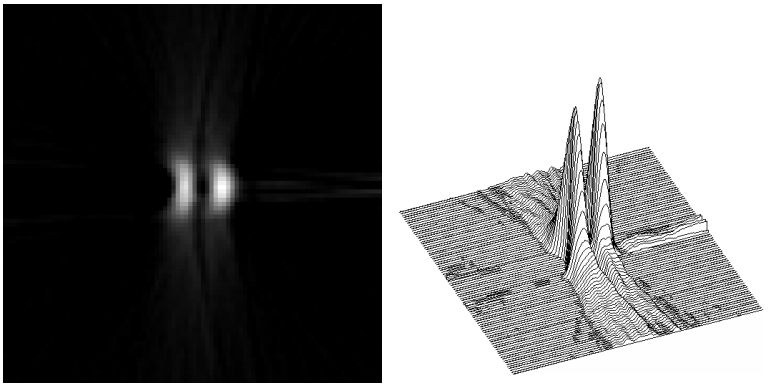

(c) Sources separated by 3 mm

Figure 6.22: Reconstructed images of two point sources separated by a small distance placed 70mm away from the centre of the FOV and the surface plots of each reconstruction illustrating the peaks

$8 \times 8 \times 1$ module is 7.4% and for the $8 \times 8 \times 8$ module 5.7%. If the detector electronics and dead space between crystals is considered, the amount of dead space for the $8 \times 8 \times 8$ module further increases to 21%.

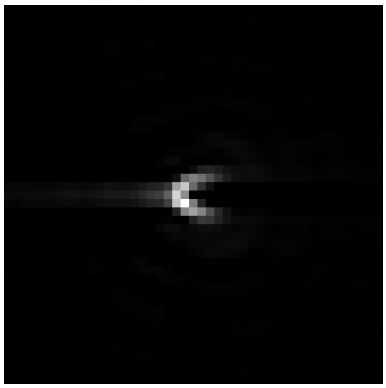

(a) Two sources separated by 1 mm

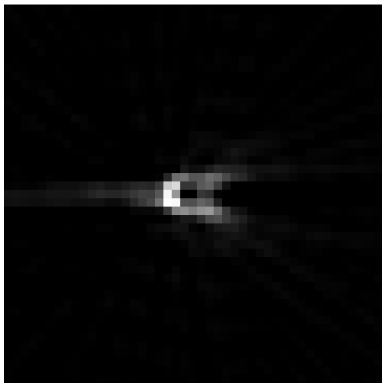

(b) Two sources separated by 2 mm

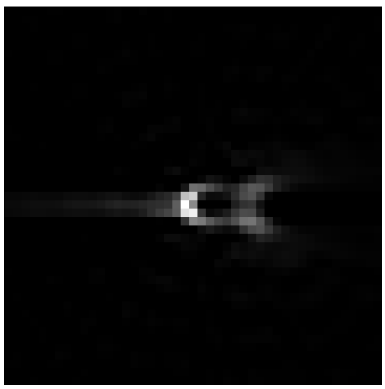

(c) Two sources separated by 3 mm

Figure 6.23: Reconstructed images of two point sources separated by a small distance using the cartesian coordinate data

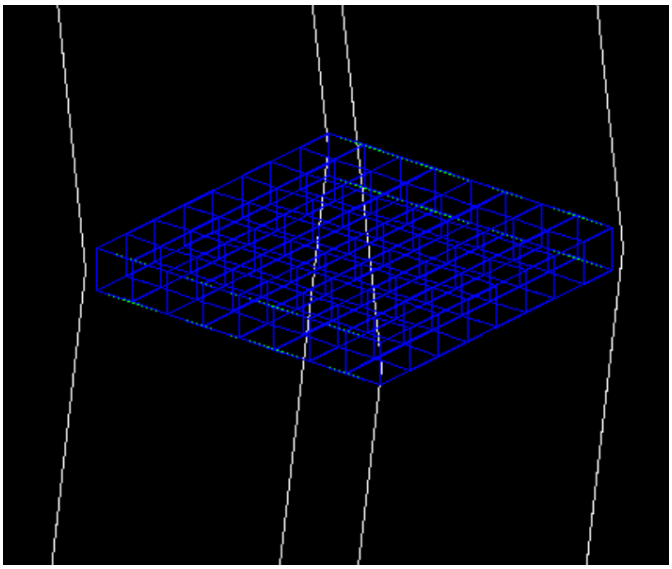

Figure 6.24: An 8 × 8 × 1 crystal detector module in "edge on" mode

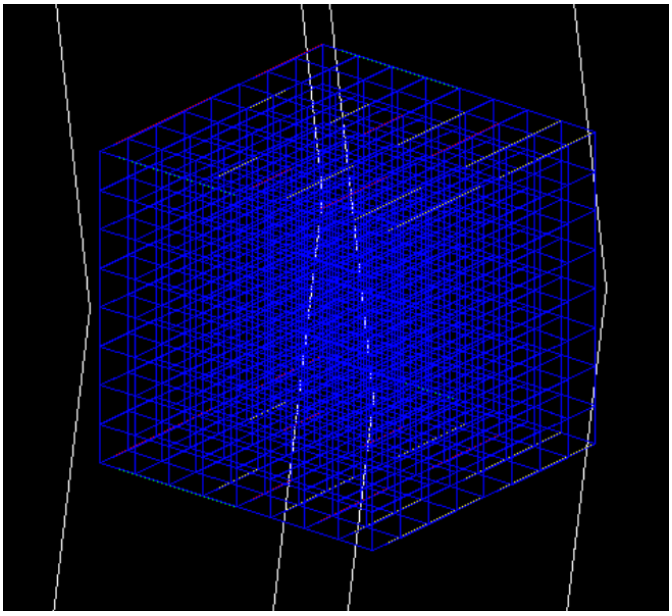

Figure 6.25: An 8 × 8 × 8 crystal detector module in "face on" mode

The PSFs across the field of view for both 3 mm and 3.5 mm pitch crystals are shown in Figure 6.26 for both crystal geometries.

The spatial resolution performance of the 3.5 mm wide detector modules appears to be reduced across the entire field of view when compared to the 3 mm wide module

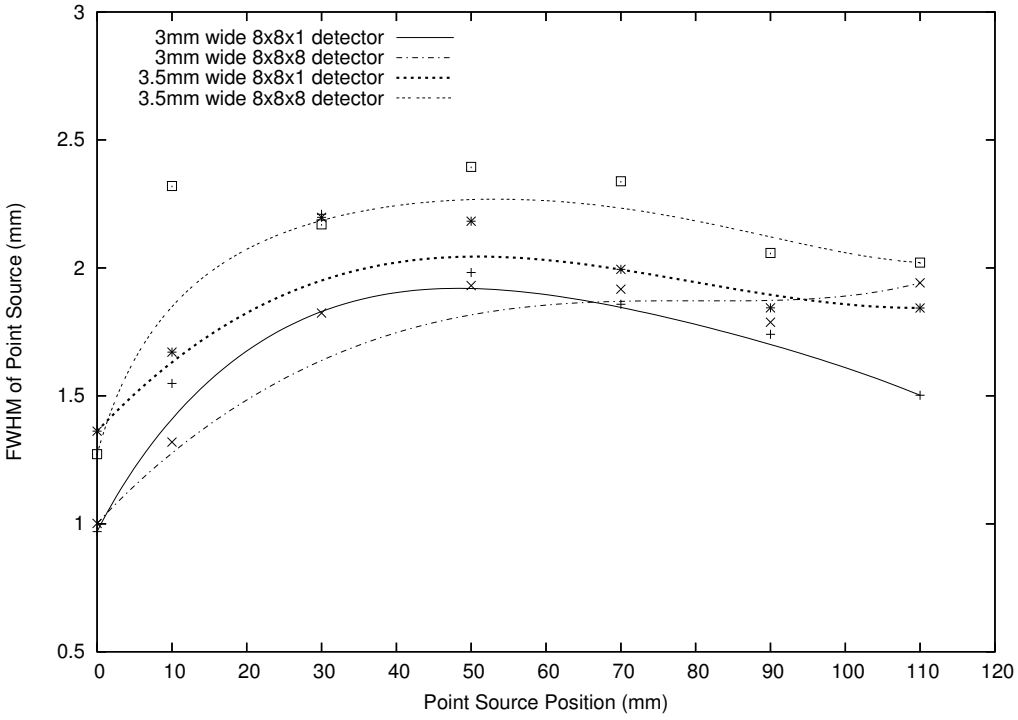


Figure 6.26: The spatial resolution across the FOV for 3 mm and 3.5 mm pitch detector modules in an $8 \times 8 \times 1$ and $8 \times 8 \times 8$ crystal arrangement

(see Section 6.9).

The $8 \times 8 \times 1$ detector module also appears to provides superior imaging to the $8 \times 8 \times 8$ detector module at the edges of field of view for a number of reasons. The system was modelled with a "Winner Takes All" method of scoring hits whereby following an interaction with multiple energy depositions, the point of interaction is located to the site of maximum energy deposition, as long as that deposition is above the LLD value. In the original $8 \times 8 \times 1$ crystal module, scattering between adjacent modules is rejected using the module span feature of GATE. However for the $8 \times 8 \times 8$ array, as the scattering is within the module itself, these counts are not rejected with the highest energy deposition position used, resulting in blurring of the position of interaction. Subsequently, using the $8 \times 8 \times 8$ detector block increases the sensitivity of the system as fewer "coincidences" are rejected at the expense of decreased spatial resolution. Further modification of the data acquisition and digitisation parameters in GATE may provide a method of alleviating problems associated to internal scatter within the module.

## 6.12 Multiple Modules Placed Axially

Small animal PET scanners can take in the order of tens of minutes to acquire sufficient data from a study as the detection sensitivity to the annihilation photons is very low. This is predominantly due to the solid angle represented by the scanner being very small in the $4\pi$ world geometry. For example, the 300 mm diameter ring with eight 3 mm wide rings constitutes only 8% of the $4\pi$ geometry seen by the photons. Hence, any increase in the number of detectors axially present in the scanner will result in improved sensitivity, at the expense of the complexity of the electronics and increased cost. Up to this point, all studies have involved a single detector module in the axial direction resulting in 8 rings of data. Each ring provides an image which represents a 3 mm thick slice through the subject (further improvements in reducing the slice thickness are discussed in Chapter 7).

In any realistic scanner design, more axial modules are required in order to maximise sensitivity. This section investigates the effect of 4 modules in the axial direction producing 32 rings with 32 slices and hence 32 sinograms for reconstruction.

As mentioned in Section 4.9.6, there can be a certain amount of "electronic collimation" of the data performed by rejecting coincidences involving interactions separated by more than a certain number of rings. Theoretically, by reducing the ring span, it is possible to reduce the amount of scatter, at the expense of sensitivity. Figure 6.27 shows the acceptance of coincidences for a ring span of 24.

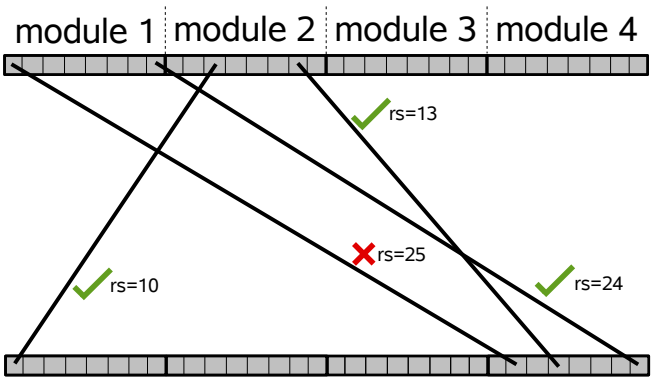


Figure 6.27: The acceptance or rejection of coincidences in the axial direction based on a ring span (rs) of 24

At present, the ring span specifications in the sinogram binning application are inaccurate; discrimination of coincidences is based simply on the axial detector module in which the coincidences take place, and not the axial ring. That is, the ring span in this instance is simply defined as the module span, and while it is somewhat similar in operation to the ring span discrimination, enhancements that must be made to provide greater accuracy in the ring span values are discussed further in Section 7.1.10. Nevertheless, the module span calculations are suitable for use in preliminary investigations of the relationship between scatter, energy window and sensitivity. A module span of 0 indicates that only coincidences occuring within a certain axial module ring are accepted, while a module span of 3 accepts coincidences

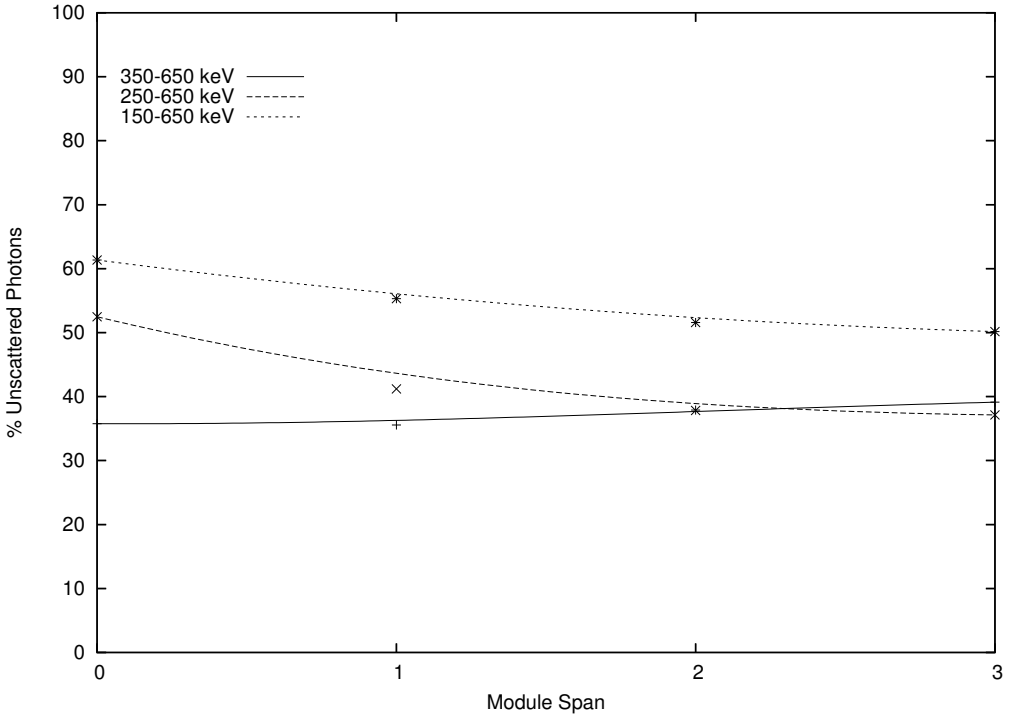


Figure 6.28: The percentage of true unscattered photons vs module span for various energy windows

across all 4 axial module rings.

A 180 mm diameter water cylinder of length 50 mm was placed at the centre of the field and a number of 0.5 mm diameter, 50 mm long line sources placed along the z-axis inside the cylinder at the centre of FOV and 10 mm, 30 mm, 50 mm and 70 mm off centre. Using the data output from the Monte Carlo simulations showing the information about the number of Compton scatter events each photon has undergone within the phantom, the percentage of unscattered photons measured with varying module span is calculated and shown in Figure 6.28 for three different energy windows: 150-650 keV, 250-650 keV, 350-650 keV.

When the module span is increased, the percentage of true unscattered photons decreases in the 150-650 keV and 250-650 keV energy windows. That is, the amount

of scatter increases. When the energy windows are large, a greater proportion of the scatter is detected and increasing the ring span simply reduces the electronic collimation allowing more of the scatter to be measured. The 350-650 keV energy window however displays the converse; as the module span is increased, the amount of unscattered photons increases. As mentioned previously, the Compton edge for a 511 keV photon exists at approximately 340 keV meaning that it is impossible for a Compton scattered photon to have an energy above 340 keV and be recorded by the system (assuming the system has infinitely good energy resolution). In the ideal case, almost all photons measured when the LLD is set to 350keV are in fact unscattered photons.

By limiting the module span, a proportion of the isotropic emissions from the source are rejected. Increasing the module span sees a larger fraction of these photons being measured resulting in an increase in the sensitivity.

The true counts within a specified module span and energy window for a given data set containing 17952668 coincidences (the data from a single small simulation) is shown in Figure 6.29.

By increasing the module span and also the energy window, more coincidences are recorded. However, the quality of the acquired data reduces significantly and scatter within the crystals becomes a significant issue. Figure 6.30 shows the central slice sinogram for the 150-650 keV, 250-650 keV and 350-650 keV energy windows with a module span of 3. For the 150-650 keV energy window, note the artefacts towards the edge of FOV arising as a result of scatter between adjacent detector modules. Also evident is the decrease in the amount of counted coincidences as the energy window becomes narrower. As these results indicate, in any study utilising a number of axial modules, it is possible to increase the sensitivity of the scanner while retaining spatial resolution by accepting data from axially spaced modules. However, use of complex inhomogenous phantoms may demonstrate otherwise.

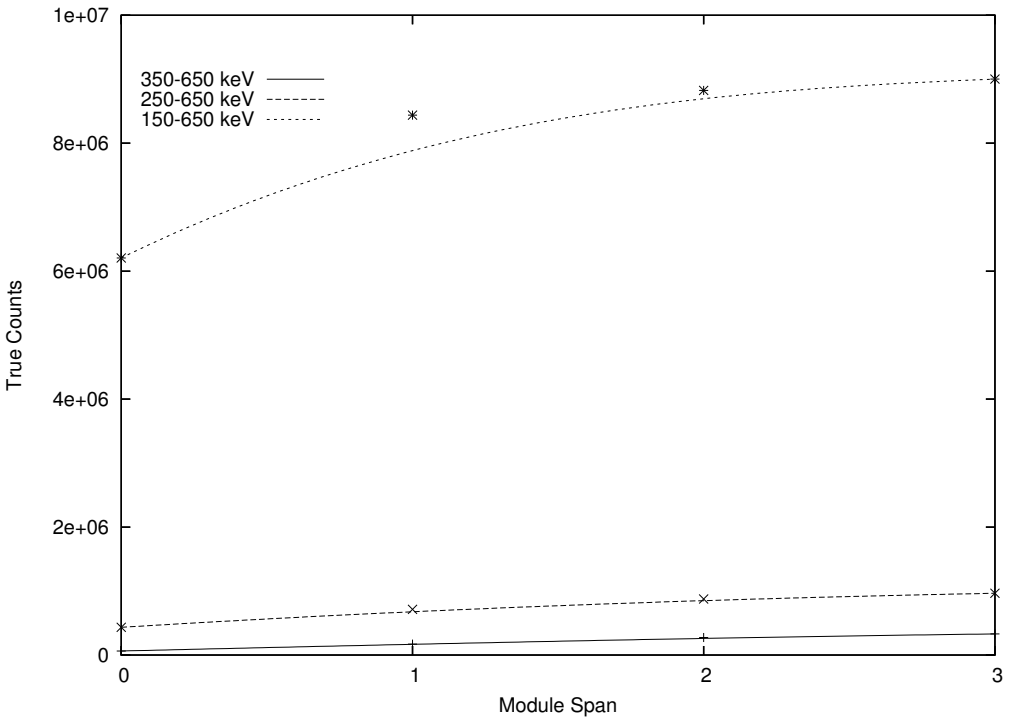


Figure 6.29: The total number of true photons versus module span for various energy windows

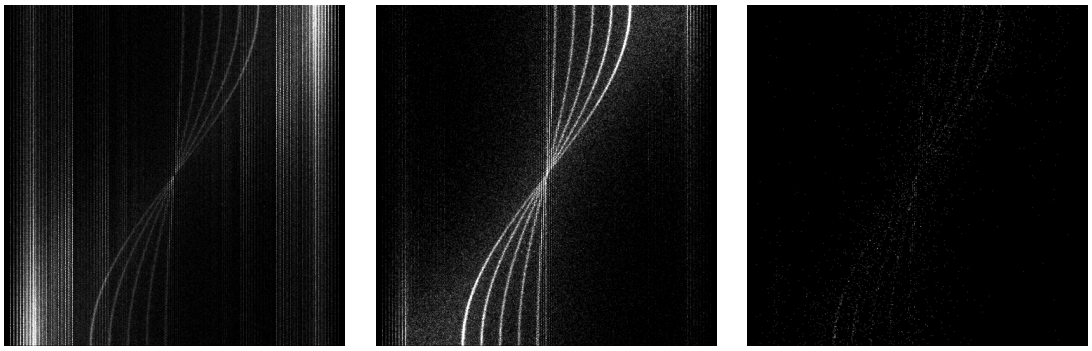

(a) 150-650 keV (b) 250-650 keV (c) 350-650 keV

Figure 6.30: The acquired sinograms for energy windows from (a) 150-650 keV, (b) 250-650 keV and (c) 350-650 keV

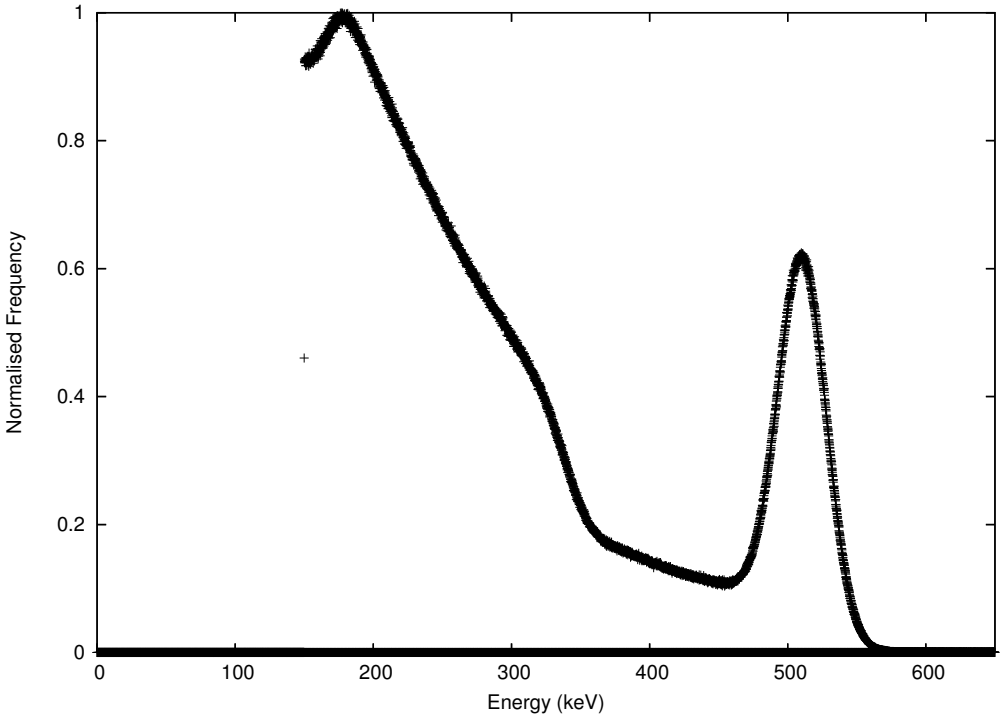


Figure 6.31: Energy Spectrum of positron sources within a water phantom

## 6.13 Energy Spectrum

Recording the energy spectrum of the detected interactions is one of the advanced troubleshooting features of the sinogram binning program. It can be used for verifying that the source energy spectrum is as expected, as well as assisting in the selection of the energy window. Figure 6.31 shows a normalised spectrum obtained from a study with positron emitting sources placed inside a water phantom. The photopeak for this study is significantly large enough to select an energy window from 350-650 keV. The FWHM of the photopeak corresponds to the blurring of the energy deposition set within the digitizer module of GATE as discussed in Section 3.3.8.

# CHAPTER 7

# RECOMMENDATIONS FOR FUTURE WORK AND CONCLUSIONS

## 7.1 Recommendations for Future Work

As stated previously, the bulk of the work presented in this thesis covers developmental work which provides a platform for future use. Hence, it is seen that there are numerous additions and refinements that can be made to the sinogram binning application, as well as the Monte Carlo simulations. This section provides a brief outline of the proposed future work.

### 7.1.1 GATE simulations

The geometry of the proposed detector modules as well as the desired sources and phantoms have been appropriately developed within the context of the Monte Carlo studies. However, the method of processing the pulses provided by the detectors is still in an extremely primitive and simplified form and requires further modification to model the processes within the actual detector module. Modification of this process can assist in the detection and rejection of scatter and will provide improvements to the dead time of the scanner in high activity studies.

### 7.1.2 Annihilation Photon Non-Collinearity

Annihilation photons conserve the momentum of the positron-electron pair which they are created by. For the annihilation photons to travel at $180^o$ to each other, the momentum of positron-electron pair must be zero at the point of annihilation. However, this is often not the case as there is residual momentum and the photons

are emitted at an angle slightly less than $180^o$ apart from each other. It is approximated that the annihilation photon non-collinearity contributes a 0.3mm FWHM blur into the final reconstructed image (for a 15cm diameter scanner) [22]. When using positron sources in GATE, the non-collinearity is modelled with the mean value of the angle distribution $\simeq 0.5^o$ [11]. The non-collinearity is not automatically modelled when using the back-to-back photons and the effect on the final reconstructed image needs to be determined.

### 7.1.3 Optimising the Sector Difference

The energy window selected in a study significantly affects the sensitivity of a scanner as illustrated by Figure 6.11. Nevertheless, increasing the energy window also causes a greater proportion of the scatter from the phantom and within the crystals to be measured. If the lower level discriminator is set to 150 keV, an annihilation photon can reach the detector without scattering in the body and then Compton scatter within the crystal depositing above 150 keV. The scattered photon can then travel to another detector module and Compton scatter again depositing above the 150 keV as illustrated in Figure 7.1. As these two pulses of light will occur almost simultaneously, the scanner determines these two events as part of a coincidence if the other annihilation photon is absorbed within the body. It is possible to reduce the effect of this by setting a minimum sector difference, a measure of the number of detector modules between allowed coincidences. Furthermore, additional modifications to the "digitiser" module of GATE can allow additional functionality and data processing capabilities. This is beneficial in studies where the $8 \times 8 \times 8$ crystal detector modules are considered.

The trade off between detector sensitivity and sector difference can be studied in order to maximise the amount of useful data being recorded.

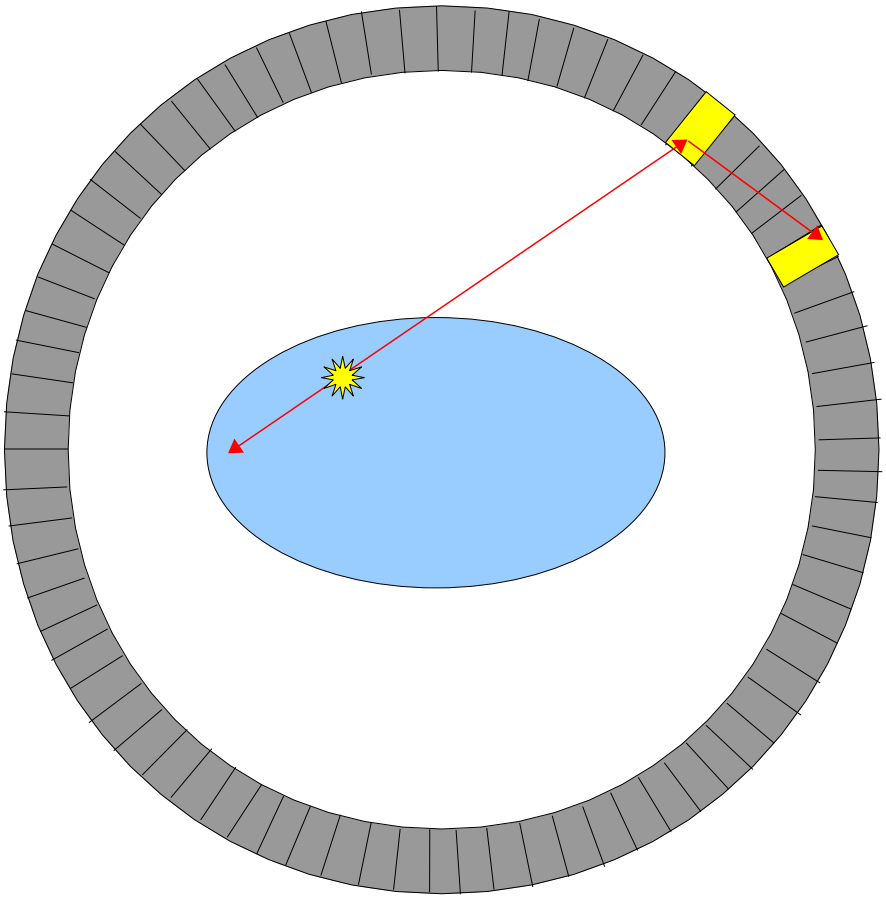

Figure 7.1: Inter-crystal scattering shown for one of the annihilation photons

### 7.1.4 Axial Resolution Tests

The spatial resolution results presented in this thesis were limited to the transaxial plane. While the sinogram binning application provides multiple slices, only a single slice of this data was reconstructed in order to measure resolution. A major limitation was the computing power available for reconstruction, each slice taking up to 2 minutes to process for higher upsampling factors. A fast method of undertaking a full 3D reconstruction, including visualisation is a recommendation for further spatial resolution measurements along the axis of the scanner.

IDL [42] is a high level programming language which has easy to use visualisation tools. Early image reconstructions for this project were undertaken using a simple OSEM algorithm written in IDL suggesting that the FBP reconstruction can also be simply written using the same software. It may also be possible to provide all of the slices as input into this program with the output being a fully 3D image data set.

Visualisation of the 3D data set, as well as further analysis, can be undertaken using a package similar to AMIDE (A Medical Imaging Data Examiner) [59]. This package can be used for "viewing, analysing, and registering volumetric medical imaging data sets" in greater detail than currently possible in ImageJ.

### 7.1.5 Coincidence Window

The coincidence window selected for a PET scanner can often be highly dependent on the timing resolution of the scanner. Furthermore, the scintillator crystal used in the detector modules as well as the predicted activity emitted by the subject are significant when selecting the optimal coincidence window. At high count rates, having long coincidence windows can result in significantly high percentage of dead times as a result of the pile up effect and an increase in the number of random coincidences without a comparable increase in the true coincidences. Conversely, having short coincidence windows which are comparable to the timing resolution

of the scanner can result in too many real coincidences being rejected. The effect of changing the coincidence window with various count rates (related to the source activity) must be undertaken for a number of energy windows. The end point of this study is to ensure that high count rates can be maintained without significant reduction in the spatial resolution.

### 7.1.6 Module Reduction

The number of detector modules in the detector ring has clearly demonstrated a causal relationship to the resolution of the final reconstructed image. By increasing the number of detector modules, an improvement in the resolution is observed and vice versa. The development of a mathematical relationship between the number of detector modules and the measured resolution for this scanner, if existing, must be given due consideration. This is of significance, as a reduction of the number of detector modules significantly simplifies the complexity of the electronics and the amount of scintillator crystal required leading to a reduction in the cost.

### 7.1.7 Voxelised Phantom

The studies undertaken so far have considered a very simple cylindrical water phantom, a very unrealistic scenario. A homogenous phantom such as this one does not provide realistic scatter as in a clinical environment. Hence, in order to investigate the resolution of the scanner operating in a more realistic environment, a voxelised phantom can be used. GATE has a feature which enables it to import voxelised phantom data which can then have a number of small active sources placed inside to measure observability and the resolution.

### 7.1.8 Cubic Crystal Limitation

At present, the sinogram binning application can only process data from Monte Carlo PET scanners containing small cubic crystals (these crystals can however

be arranged into non-cubic blocks). The LOR calculation requires the cartesian coordinates of the two positions of the coincidence. These position calculations utilise the user input provided on the physical parameters of the scanner which remains reliant on crystals being uniformly sized in all directions. Introducing 3 new variables for the axial, radial and tangential size of the crystal and rewriting of the position calculation section of the application can enable non-cubic geometries to be considered. As stated in Section 5.2, the MicroPET Focus 220 containing $1.5 \times 1.5 \times 10$ mm$^3$ crystals was simulated, however required the crystal to be split into 6 separate $1.5 \times 1.5 \times 1.5$ mm$^3$ blocks.

### 7.1.9 Axial Binning

#### 7.1.9.1 Michelograms

The method of utilising Michelograms to represent 3D PET data as presented in Section 2.11.3 is a far superior method to the one developed in this study as Michelograms present a method of efficient data storage and improving axial sampling. Further developments of the sinogram binning application must incorporate a method of retaining the integrity of the true 3D PET data which is acquired.

#### 7.1.9.2 Increased Axial Sampling

The number of axial slices in the sinogram binning application is currently equal to the number of axial crystals. That is, for a ring containing only a single detector module in the axial direction, there are 8 axial crystal modules and hence 8 independent slices and sinograms as illustrated in Figure 7.2(a). One of the major limitations of this method is the inability to position accurately coincidences which have occurred within adjacent detector rings as the SSRB determines the axial position of the LOR's origin to be at the boundary between the two slices. Hence, it is recommended that the number of axial slices be increased to $2N - 1$ slices where N represents the number of axial crystals as shown in Figure 7.2(b). This

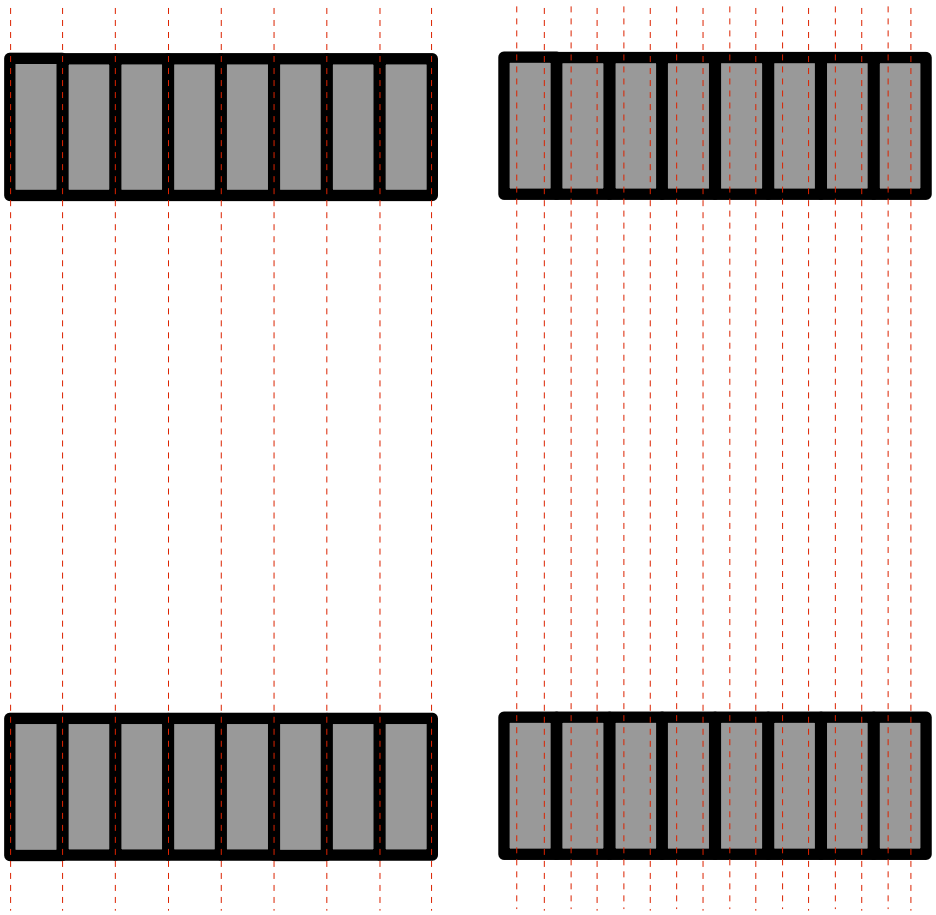

(a) 8 axial slices (b) 15 axial slices

Figure 7.2: Axial upsampling

ensures that coincidences between adjacent modules can be placed into the appropriate sinogram. The main limitation of increasing the axial sampling is the inverse relationship between the axial sampling factor and the number of counts recorded for the sinogram of each slice. Investigation of the optimal axial upsampling factor for numerous studies with varied data sets is necessary.

The transaxial resolution is heavily dependent on the number of detector modules present in the ring. Likewise, the axial resolution is significantly affected by the crystal width. Furthermore, the method of axial binning is of significance. This study utilises the crudest, yet simplest and computationally cheapest solution, the SSRB (outlined in Section 2.11.3). This method has significant limitations and

alternatives are available, albeit at slightly greater computational complexity.

The Multi-Slice Rebinning algorithm increments elements of multiple sinograms [60] as it determines the slices that the LOR traverses axially. Starting from one axial extremity of this LOR, small steps are taken along the LOR up to the other axial extremity. The slice that each step position falls into along with the appropriate transaxial position are then used to increment the sinogram for that individual slice. Hence, a large number of slices are incremented for a single LOR. The more oblique the angle of the LOR to the axial direction, the smaller the contribution to the sinogram from that LOR as less steps occur within the slice width. For a normally incident LOR, all of the incrementation would occur within a single slice. Figure 7.3 illustrates the steps and the slices which contain sinograms that are incremented. Upon completion of the binning, the image reconstruction is carried out similarly to the SSRB with each slice independently reconstructed.

The addition of the multi-slice rebinning algorithm is a relatively simple improvement to make to the sinogram binning.

### 7.1.10 Ring Span

The method utilised by the sinogram binning application to determine the ring difference between the 2 photons in a coincidence is severely limited. The ring span is simply determined by calculating the difference between the ring number of the first photon and the second photon according to:

$$\begin{aligned} ring\ number1 &= rsectorID1 \ \mathbf{mod}\ number\ of\ rings \\ ring\ number2 &= rsectorID2 \ \mathbf{mod}\ number\ of\ rings \\ ring\ span &= abs(ring\ number1 - ring\ number2) \end{aligned} \tag{7.1}$$

At present, the ring number is not calculated, only the detector module in which the interaction takes place. Hence, specifying a maximum ring difference value

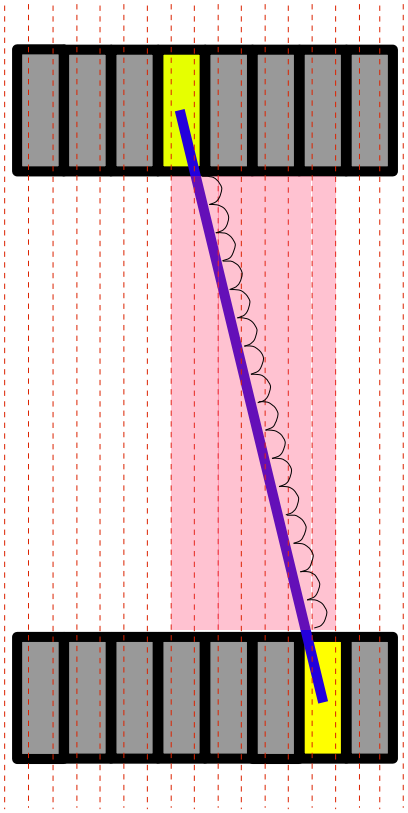

Figure 7.3: Multi-slice rebinning showing the step length and the slices in which all of the steps occur

simply sets the maximum axial module difference. Using the rsectorID and the crystalID, a simple modification to the sinogram binning application will allow determination of the actual ring number and an improved method of specifying the maximum ring difference.

### 7.1.11 Attenuation Correction

Most PET studies require attenuation correction to be undertaken on a data set before reconstruction. The attenuation map is acquired by using a transmission source on one side of the object being imaged and rotated around to acquire tomographic data, similar to a CT scan. The transmission sinogram acquired from this study is incorporated into the emission sinogram to account for the attenuation within the study. Future versions of the sinogram binning application must incorporate a method of utilising transmission data with the emission data in order to produce more accurate reconstructions.

### 7.1.12 Object Oriented Code

Early versions of the sinogram binning application were entirely procedural, that is, the data from the program is separate to the operations that manipulate the data. This is not a truly efficient method of data manipulation and hence object oriented (OO) programming is recommended as a more suitable method. Object oriented programming has both the data and the operations that manipulate the data encapsulated as a single "object". It also enables data to be passed to functions as opposed to continuous chunks of code within the main function.

There are numerous functions already present in the sinogram binning application, however further optimisation can be achieved by a thorough rewriting of the entire application. At present, the sinogram binning application can parse approximately 9MB of raw Monte Carlo data per second, resulting in significant processing time when binning large data sets which are typically of the order 15 GB or greater.

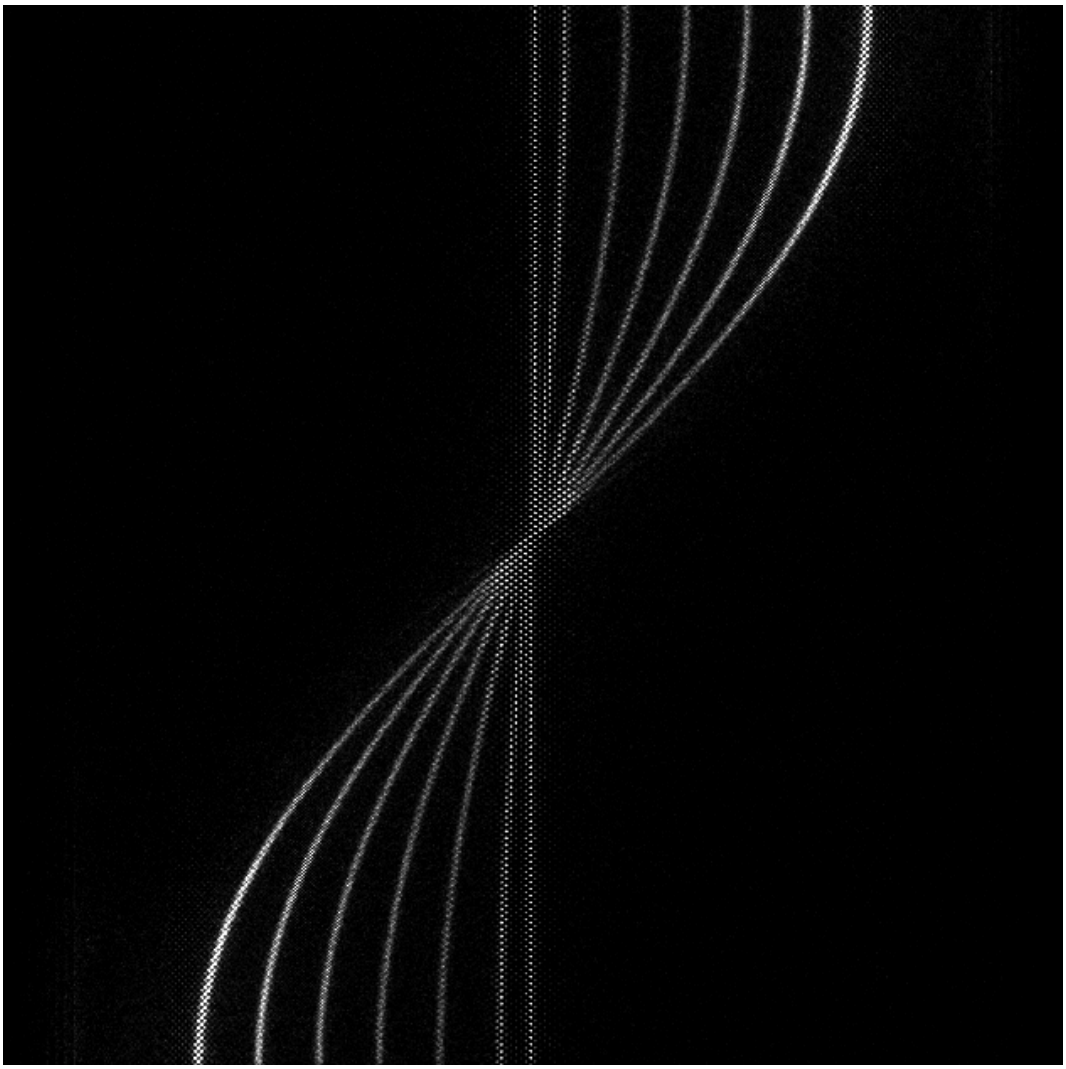

Figure 7.4: An oversampled sinogram showing "zero efficiency" bins

It is anticipated that efficient rewriting of the application by making it OO can provide an improvement in data processing performance.

### 7.1.13 Non-Linear Sinogram Binning

One of the main advantages of the sinogram binning application is its ability to upsample the Monte Carlo data enabling a wider range of LORs. However, certain LORs are not possible at the centre of the FOV resulting in "zero efficiency bins" in the sinogram illustrated in Figure 7.4. The zero efficiency bins cause significant artefacts in the final image reconstruction.

A non linear method of binning the data is required, changing the upsampling factor across the image in order to represent all the present LORs while not causing oversampling and hence reconstruction artefacts. A suitable method of implementing this scheme is outlined in Virador et al. [51]. This method of non-linear binning, or another novel technique, can be incorporated into the sinogram binning application in future versions.

### 7.1.14 Manual Definition of Sinogram Dimensions

At present, the dimensions of the sinogram created by the sinogram binning application are defined by half the number of detector pairs multiplied by the upsampling factor. This construct was initially defined for detector modules which were relatively small in the tangential direction and contained DOI information. However, in the case of larger detector blocks such as the microPET scanner which contains a 12 $\times$ 12 array of 1.5 $\times$ 1.5 $\times$ 10 mm$^3$ crystal elements, this technique does not work as the number of actual detector modules in the ring is insufficient to produce a suitably sized sinogram. It is therefore important to be able to specify the sinogram dimensions manually.

A simple work-around has been implemented for this study by selecting a high upsampling factor such as 16 or 32. While the microPET does not provide any DOI information, a high upsampling factor is required to construct a sinogram which is large enough to accurately represent the data from the scanner. Had a lower upsampling factor of 4 (as in all DOI studies presented) was used, the sinogram dimensions for the microPET scanner would be 84 $\times$ 84 (42 $\div$ 2 $\times$ 4), too small to be able to provide the required resolution. In future versions of the code, a manual sinogram dimension definition must be made available for detector modules that have multiple elements in the tangential direction to alleviate the need for this work-around.

## 7.2 Conclusions

This thesis has presented some preliminary performance data of a novel PET module design proposed by the Centre for Medical Radiation Physics. The results from the Monte Carlo studies indicate that the novel design can provide significant improvement in the spatial resolution of a small animal PET scanner at the edges of field, with a significant reduction in the radial elongation artefact. The depth of interaction information provided by this scanner enables this superior performance. At the centre of FOV, the 8 layer detector module provides a resolution of approximately 1 mm extending to 1.5 mm at the edge of FOV, 110mm from the centre.

One of the most important findings from the Monte Carlo studies undertaken involves the results comparing scanners monolithic crystal detector modules to ones with segmented crystals (as outlined in Section 6.3). As expected, having a higher number of crystals to measure the DOI results in superior resolution across the field of view. However, the performance of a detector module containing a monolithic crystal was comparable to an 8 layer module if only the central 60 mm of the FOV is considered. Similarly, for the central 140 mm of the FOV, a 4 layer detector module performs identically to the 8 layer module. Hence, it is possible to reduce the complexity of the electronics if the specific purpose of the scanner is known beforehand.

The crystal size of the sensitive detector volumes is a significant factor when measuring the intrinsic resolution of the scanner. Using smaller crystals than the originally proposed $3 \times 3 \times 3$ mm$^3$ crystals improves the resolution of the scanner, however the improvements are limited depending on the choice of the radioisotope. When the positron range of the isotope is comparable or larger than the crystal size, the improvement offered by reducing the crystal size is not as pronounced. This is demonstrated in the spatial resolution studies using Carbon-11 and Oxygen-15 sources with mean positron ranges of 1.1 mm and 2.5 mm respectively compared to

the Fluorine-18 studies with a 0.6 mm mean positron range.

While the resolution of the scanner is improved when using smaller crystal elements, the sensitivity also decreases. Many photons often scatter numerous times within a single crystal before photoelectric absorption. As the crystal size is decreased, there is less volume for the scattering to occur within and the photons escape into adjacent crystals and modules whereby the scanner is programmed to reject them.

One of the main goals at the commencement of this study was to illustrate whether the initially proposed $8 \times 8 \times 1$ crystal "edge on" detector module would provide better results than a $8 \times 8 \times 8$ "face on" detector module. Studies modelling both the ideal $3 \times 3 \times 3$ mm$^3$ and the dead-space considering $3.5 \times 3.5 \times 3.5$ mm$^3$ crystals indicate that the $8 \times 8 \times 1$ module appears to provides superior resolution. It is anticipated that this discrepancy is as a result of the $8 \times 8 \times 8$ block being more susceptible to intra-module scatter than the $8 \times 8 \times 1$ module. Further improvement within the electronic pulse processing may provide parity between the two proposed module geometries and requires further investigation.

A newly developed sinogram binning application for processing Monte Carlo PET data has been described. This application is flexible and is able to adapt to the geometric properties of many different types of scanners. The sinogram binning application reads in data from the Monte Carlo studies, determines the positions of the coincidence within the world volume, determines the LOR and increments the appropriate sinogram represented by this LOR.

The sinogram binning application can "upsample" the data in order to fully utilise the information from the depth of interaction. Upsampling the data enables the sinogram dimensions to be increased with a greater range of LORs becoming possible. These LORs exist with angles and radial distances between the LORs available from a single monolithic crystal detector. Increasing the upsampling factor results in a superior sinogram which has reduced radial elongation artefacts. There

is, however, some significant discretisation artefacts observed at the centre of the field of view due to oversampling. That is, certain LORs simply are not possible due to the module and crystal size of the scanner resulting in "zero efficiency bins". The zero efficiency bins are only a significant issue at the centre of FOV and the effect reduces significantly when moving away from the centre. It is anticipated however that a non-linear binning method can resolve this issue, whereby the upsampling factor is varied across the FOV to higher values towards the edges of FOV where a greater range of LORs are possible than at the centre.

Much of the work presented in this thesis focused on the development of the sinogram binning application and the Monte Carlo simulations. At present, this area of research is poised for future development including further optimisation of the novel detector module and the sinogram binning application.

# APPENDIX A
# SINOGRAM BINNING APPLICATION SOURCE CODE

This Appendix contains the sinogram binning application source code. A full version can be found on the attached CD-ROM and documentation of function is discussed in Chapter 4

```
001
002 //
003 // A program which determines the LORs from the coincidence data files
004 // from a GATE simulation and creates a sinogram output
005 //
006
007
008 //  Lakshal Perera
009 //  CMRP, University of Wollongong, NSW
010 //  lp20@uow.edu.au
011 //  31/7/2008
012
013
014
015 #include <iostream>
016 #include <fstream>
017 #include <iomanip>
018 #include <string>
019 #include <sstream>
020 #include <math.h>
021
022 using namespace std;
023
024
025 void initialise_sino_matrix(int,int);  //redundant, used if sinogram code reads in an old sinogram before processing new data
026 void read_in_options(int,int,int);
027 void read_in_from_data_file(string);
028 void write_out_sinogram(int,int,int,long int[]);
029 int bin_sinogram(float,float);
030
031 int calculate_slice(int,int,float,float);
032 int round(const float &number, const int num_digits);
033 int yint_pos_neg(float y_int);
034 int grad_pos_neg(float gradient);
035 bool sign(float n);
036 void energy_histogram_fn(float energy_1, float energy_2);
037 int calculate_position(int,int,long int[]);
038
039
040 char inputfile[20];
```

```
041
042 double time1,time2;
043 float x_1,y_1,z_1,x_2,y_2,z_2;
044 int rsector1, rsector2, crystal1, crystal2;
045 float energy_1,energy_2;
046 float blank; //to read in the detector IDs which aren't of any use to us. eg. layerID, subModuleID;
047 float annihilation1, annihilation2;
048 float gantry_angular_position;
049
050 float photon_from_source=0;
051 float photon_from_background=0;
052
053
054 float rad_pix_size;
055 float angle_pix_size;
056
057 float gradient;
058 float angle;
059 float r;
060 float ring_radius;
061
062 long int i;
063 float x,y, y_int, x_int;
064
065 int id_or_coord;
066 int multi_or_single_layer;
067 int scaling_factor;
068 int energy_yes_or_no;
069 int multiple_rings_yes_or_no;
070 int num_rings;
071 int allow_multiRing_coinci;
072 int ring_span;
073 int ring_difference;
074 int rotating_gantry;
075 int annihilation_pos_yes_or_no;
076
077 int compton_scatter;
078 int compton_scatter_weighting;
079 float compton_phantom1, compton_phantom2;
080 float compton_detector1, compton_detector2;
```

```
081 float phantom_scatter, phantom_real;
082 float detector_scatter, detector_real;
083 float compton_phantom_counter=0,real_counter=0;
084
085 float E_lower=0.35; //default value
086 float E_upper=0.65; //default value
087
088 float num_rsectors;//314 or 470
089 int layers_per_sector;
090 int upsampling_factor;
091 int rebinned_num_layers;
092 int ring_number1;
093 int ring_number2;
094 int interRing_coincidence;
095
096
097 int crystals_in_z_direction;
098 float depth_in_radial_direction;
099 int crystals_in_tangential_direction;
100 float crystal_size; //size of crystals in z direction (always fixed)
101
102 float radial_distance1;
103 float radial_distance2;
104 float rsector_angle1;
105 float rsector_angle2;
106 float tangential_correction1;
107 float axial_correction1;
108 float radial_correction1;
109 float angular_correction1;
110 float tangential_correction2;
111 float axial_correction2;
112 float radial_correction2;
113 float angular_correction2;
114
115
116 float r_pix;
117 float angle_pix;
118 int y_pos_neg;
119 int sino_midpoint;
120
```

```
121 //8 variables defining the positions of the vertices of the sinogram binning kernel
122 float x_pix_upperLeft;
123 float x_pix_upperRight;
124 float x_pix_lowerLeft;
125 float x_pix_lowerRight;
126 float y_pix_upperLeft;
127 float y_pix_upperRight;
128 float y_pix_lowerLeft;
129 float y_pix_lowerRight;
130
131 //areas of intersection of binning kernel and actual sinogram pixels
132 float A_pix_upperLeft;
133 float A_pix_upperRight;
134 float A_pix_lowerLeft;
135 float A_pix_lowerRight;
136
137 //defines which output file LOR goes into depending on it's
138 int axial_layer_number;
139 float average_z;
140 int slice;
141
142
143 double sinogram[1500][1500][32];
144 long int coincidence_counts_total=0;
145 long int coincidence_counts_inside_window=0;
146
147
148 const int num_energy_bins = 10000;
149 long int energy_histogram[num_energy_bins];
150 int energy_histogram_yes_or_no;
151 float E_histo_step;
152
153 int q=0;
154 int line_counter=0;
155
156 int num_data_files;
157 string data_filename;
158
159 int r_pix_array_temp[2000];
160 int angle_pix_array_temp[2000];
```

```
161
162 ifstream fin;
163
164
165
166
167 int array[300];
168 //have to hardcore this because if i declare it inside the read in options file, it can't get passed to the read_in_data function.
169 long int layer_histogram[20];
170
171 int main()
172 {
173
174   cout<<"What is the ring radius? (mm)"<<endl;
175   cin>>ring_radius;
176
177   cout<<"How many rsectors in the detector?"<<endl;
178   cin>>num_rsectors;
179
180   cout<<"What size are the crystals? (mm)"<<endl;
181   cin>>crystal_size;
182
183   cout<<"How many crystals in the axial direction?"<<endl;
184   cin>>crystals_in_z_direction;
185
186   cout<<"How deep is detector in radial direction? (mm)"<<endl;
187   cin>>depth_in_radial_direction;
188   layers_per_sector=int(ceil(depth_in_radial_direction/crystal_size));
189
190   int axial_samples = crystals_in_z_direction;
191
192   //cout<<"Crystals are "<<crystal_size<<"x"<<crystal_size<<"x"<< crystal_size<<endl<<endl;
193
194
195   cout<<"Is there annihilation position information? (1: yes, 0:no)"<<endl;
196   cin>>annihilation_pos_yes_or_no;
197
198   cout<<"Are there multiple rings? (1: yes, 0: no)"<<endl;
199   cin>>multiple_rings_yes_or_no;
200   if (multiple_rings_yes_or_no==1)
```

```
    {
    cout<<"How many axial detector rings?"<<endl;
    cin>>num_rings;
    cout<<"Allow coincidences from separate rings? (1: yes, 0: no)"<<endl;
    cin>>allow_multiRing_coinci;
    if (allow_multiRing_coinci==1)
      {
      cout<<"What is the maximum ring difference allowed? (must be less than "<<num_rings-1<<"). Coincidences in the same ring have a ring difference = 0"<<endl;
      cin>>ring_span;
      }
    axial_samples = axial_samples*num_rings;
    }
  else
    {
    num_rings=1;
    }


  cout<<"Is it a rotating gantry? (1: yes, 0: no)"<<endl;
  cin>>rotating_gantry;

  cout<<"Is there Compton Scatter info? (1: yes, 0: no)"<<endl;
  cin>>compton_scatter;
  if (compton_scatter ==1)
  {
    cout<<"Scatter weighting factor (1 = no additional weighting)"<<endl;
    cin>>compton_scatter_weighting;
  }


  cout<<"Upsampling factor? (1,2,4,8)"<<endl;
  cin>>upsampling_factor;

  long sino_radial=long (upsampling_factor*num_rsectors/2)+1;//471 or 315 depending on crystal size
  long sino_angles=long (upsampling_factor*num_rsectors/2)+1;//471 or 315 depending on crystal size

  cout<<"Use use co-ords from data(0) or detector ID's for x,y,z positioning (1)?"<<endl;
  cin>>id_or_coord;


```

```
240   if (id_or_coord==1)
241   {
242       cout<<"Is the scintillator made up of Single Crystal (0) or Multiple Layers (1)?"<<endl;
243             cin>>multi_or_single_layer;
244
245       if (multi_or_single_layer==1)
246       {
247     cout<<"How many crystals in the radial direction?"<<endl;
248     cin>>rebinned_num_layers;
249
250       }
251
252
253   }
254
255   cout<<"How many crystals in the tangential direction?"<<endl;
256   cin>>crystals_in_tangential_direction;
257
258   read_in_options(sino_radial, sino_angles, axial_samples);
259
260   return 1;
261 }
262
263
264
265 void read_in_options(int sino_radial, int sino_angles, int axial_samples)
266 {
267
268
269   rad_pix_size=(ring_radius*2 + 2*depth_in_radial_direction + 10)/float(sino_radial);
270
271   angle_pix_size=180/float(sino_angles);//180/float(sino_angles); //180
272
273   char rebin_flag;
274
275 //  long int layer_histogram[rebinned_num_layers];
276
277   for (int q=0;q<rebinned_num_layers;q++)
278     layer_histogram[q]=0;
279
```

```
280   //cout<<"What folder is the data stored in?"<<endl;
281   //cin>>data_filename;
282
283
284   //data_filename="/media/IOMEGA_HDD/GATE_data/gamma_sources/gamma_30cm_3x3x3_backgroundwaterphantom10%/data";
285
286   //data_filename="/media/IOMEGA_HDD/GATE_data/gamma_sources/gamma_30cm_3x3x3_nophantom/data";
287   //data_filename="/media/IOMEGA_HDD/GATE_data/positron_sources/positron_30cm_3x3x3_backgroundwaterphantom50%/data";
288   //data_filename="/media/IOMEGA_HDD/GATE_data/positron_sources/positron_10cm_3x3x3_backgroundwaterphantom50%/data";
289   //data_filename="/media/IOMEGA_HDD/GATE_data/positron_sources/positron_30cm_3x3x3_backgroundwaterphantom50%/data";
290   //data_filename="/media/IOMEGA_HDD/GATE_data/positron_sources/positron_30cm_3x3x3_backgroundwaterphantom_SmallSeparationPointSources_1mm/data";
291   //data_filename="/media/IOMEGA_HDD/GATE_data/positron_sources/positron_30cm_3x3x3_backgroundwaterphantom_SmallSeparationPointSources_2mm/data";
292   //data_filename="/media/IOMEGA_HDD/GATE_data/positron_sources/positron_30cm_3x3x3_backgroundwaterphantom_SmallSeparationPointSources_3mm/data";
293
294 //DO NEXT!!!!!!
295   //data_filename="/media/IOMEGA_HDD/GATE_data/positron_sources/positron_30cm_3x3x3_1MBqWaterPhantom_4rings/data";
296
297
298
299   //data_filename="/media/IOMEGA_HDD/GATE_data/positron_sources/positron_30cm_3x3x3_1MBqWaterPhantom_RotatingGantry/data_offset_starting";
300   //data_filename="/media/IOMEGA_HDD/GATE_data/positron_sources/positron_30cm_3x3x3_1MBqWaterPhantom_RotatingGantry/data_faster_spinning";
301 //  data_filename="/media/IOMEGA_HDD/GATE_data/positron_sources/positron_30cm_2x2x2_1MBqWaterPhantom_RotatingGantry_ComptonInfo/data";
302   //data_filename="/home/lucky/geant4/gateSims/post_hawaii_conference/8x8x8block_detector";
303 //  data_filename="/media/IOMEGA_HDD/GATE_data/positron_sources/positron_30cm_3x3x3_1MBqWaterPhantom_RotatingGantry_ComptonInfo_8x8x8block";
304   //data_filename="/media/IOMEGA_HDD/GATE_data/positron_sources/positron_30cm_3x3x3_CylindricalPhantom/data";
305   //data_filename="/home/lucky/geant4/gateSims/post_hawaii_conference/scatter_studies";
306   //data_filename="/media/IOMEGA_HDD/GATE_data/positron_sources/positron_30cm_3x3x3_CylindricalPhantom/data";
307 //  data_filename="/media/IOMEGA_HDD/GATE_data/positron_sources/positron_30cm_3x3x3_1MBqWaterPhantom_ScatterStudies/data";
308   //data_filename="/home/lucky/geant4/gateSims/post_hawaii_conference/background_concentration_variations";
309
310   //data_filename="/media/IOMEGA_HDD/GATE_data/positron_sources/positron_30cm_3x3x3_ScatterStudies/b250MBq_s1MBq/data";
311   //data_filename="/home/lucky/geant4/gateSims/post_hawaii_conference/source_to_background_ratio_determination";
312   //data_filename="/media/IOMEGA_HDD/GATE_data/positron_sources/positron_30cm_3x3x3_ScatterStudies/b250MBq_s1MBq/data";
313   //data_filename="/media/IOMEGA_HDD/GATE_data/positron_sources/positron_30cm_3x3x3_ScatterStudies/b100MBq_s1MBq/data";
314 //  data_filename="/media/IOMEGA_HDD/GATE_data/positron_sources/positron_30cm_3x3x3_ScatterStudies/b25MBq_s1MBq/data";
315   //data_filename="/media/IOMEGA_HDD/GATE_data/positron_sources/microPET/data";
316   //data_filename="/home/lucky/geant4/gateSims/post_hawaii_conference/4_rings";
317   //data_filename="/home/lucky/geant4/gateSims/post_hawaii_conference/realistic_scanner";
318   //data_filename="/media/IOMEGA_HDD/GATE_data/positron_sources/positron_30cm_3x3x3_1MBqWaterPhantom_RotatingGantry/data";
319   //data_filename="/media/IOMEGA_HDD/GATE_data/positron_sources/realistic_scanner/data";
```

```
320
321 //  data_filename="/media/IOMEGA_HDD/GATE_data/positron_sources/positron_30cm_3.5x3.5x3.5_RotatingGantry_ComptonInfo_8x8x8block/data";
322   //data_filename="/media/IOMEGA_HDD/GATE_data/positron_sources/positron_30cm_3.5x3.5x3.5_LargeCylindricalSource/data";
323   //data_filename="/media/IOMEGA_HDD/GATE_data/positron_sources/positron_30cm_3.5x3.5x3.5_1MBqWaterPhantom_4rings/data";
324   //data_filename="/media/IOMEGA_HDD/GATE_data/positron_sources/positron_30cm_1x1x1_1MBqWaterPhantom_RotatingGantry_ComptonInfo/data";
325   //data_filename="/media/IOMEGA_HDD/GATE_data/positron_sources/positron_30cm_3x3x3_SmallSeparationStudies/positron_30cm_3x3x3_SmallSeparation3mm/data";
326 //  data_filename="/media/IOMEGA_HDD/GATE_data/positron_sources/microPET_v2/data";
327 //  data_filename="/media/IOMEGA_HDD/GATE_data/positron_sources/30cm_crystalsize_VS_sensitivity/gamma/3mm";
328   //data_filename="/media/IOMEGA_HDD/GATE_data/positron_sources/30cm_crystalsize_VS_sensitivity_VERSION2/no_electrons/3mm";
329 //   data_filename="media/IOMEGA_HDD/GATE_data/positron_sources/30cm_crystalsize_VS_sensitivity_VERSION2/1mm";
330   data_filename="/media/IOMEGA_HDD/GATE_data/positron_sources/positron_30cm_3x3x3_SmallSeparationStudies/positron_30cm_3x3x3_SmallSeparation3mm_offCentre/data";
331 //  data_filename="/media/IOMEGA_HDD/GATE_data/positron_sources/positron_30cm_IsotopePositronRange_VS_CrystalSize/carbon-11/3mm/data";
332
333
334
335
336   cout<<"How many data files?"<<endl;
337   cin>>num_data_files;
338
339   cout<<"Data is coming from "<<data_filename<<endl;
340
341   cout<<"Is there energy data in the files? (0: no, 1: yes)"<<endl;
342   cin>>energy_yes_or_no;
343   if (energy_yes_or_no==1)
344     {
345     cout<<"What is the lower level discriminator (MeV)?"<<endl;
346     cin>>E_lower;
347     cout<<"What is the upper level discriminator (MeV)?"<<endl;
348     cin>>E_upper;
349
350
351     cout<<"Provide an energy histogram at the end? (0: no, 1:yes)"<<endl;
352     cin>>energy_histogram_yes_or_no;
353     if (energy_histogram_yes_or_no==1)
354       {
355       E_histo_step = 0.65/num_energy_bins;
356       }
357     }
358
359   string gateCoincidences="/gateCoincidences_";
```

```
360   string dat= ".dat";
361   string this_filename;
362
363   //read in the multiple data files
364   for (int q=1;q<num_data_files+1;q++)
365     {
366     line_counter=0;
367     std::stringstream ss;
368     std::string str;
369     ss << q;
370     ss >> str;
371
372     this_filename= data_filename + gateCoincidences +str + dat;
373     cout<<"Opened and processing "<<this_filename<<endl;
374     //cout << "Progress  ";
375     cout << "0------100"<<endl;
376
377     //open file for reading
378
379     fin.open(this_filename.c_str(),ios::in);
380
381     if (fin.fail())
382     {
383       cout<<"This file does not exist anywhere in the universe"<<endl;
384       write_out_sinogram(sino_radial,sino_angles,axial_samples,layer_histogram);
385       return;
386     }
387
388     //make sure we read in all lines in each data file
389     //for (i=1;i<10;i++)
390     while (!fin.eof())
391
392     //while ((compton_phantom_counter + real_counter) <5000)
393       {
394       read_in_from_data_file(this_filename);
395       //calculate_position(sino_radial,sino_angles,layer_histogram)==1;
396
397
398       //create fake randoms if they're required.
399       if (compton_scatter==1 && compton_scatter_weighting >1 && (compton_detector1==1||compton_detector2==1) && calculate_position(sino_radial,sino_angles,layer_histogram)==1)
```

```
400         {
401         for (int i=0;i<compton_scatter_weighting;i++)
402           {
403           r_pix = (sino_radial/2-1) * float(rand()%1000*0.001) * pow(-1,rand()%2);
404           angle_pix = (sino_angles/2-1) * float(rand() %1000 *0.001) * pow(-1,rand()%2);
405           compton_phantom_counter++;
406           bin_sinogram(r_pix,angle_pix);
407
408
409           if (annihilation_pos_yes_or_no==1)
410             {
411             if (annihilation1 ==7 && annihilation2 ==7)
412               photon_from_background++;
413             else
413               photon_from_source++;
414             }
415           }
416         }
417       else
417         {
418         calculate_position(sino_radial,sino_angles,layer_histogram)==1;
419         }
420
421       }
422
423
424     //close data file which we are reading from
425     fin.close();
426
427     cout<<endl<<endl;//<< "finished file "<<this_filename<<endl<<endl;
428     }
429
430   write_out_sinogram(sino_radial,sino_angles,axial_samples,layer_histogram);
431 //for (int q=0;q<sino_angles*upsampling_factor;q++)
432 //  cout<<q<<"  "<<array[q]<<endl;
433
434 }
435
436
437
```

```
438
439
440 void read_in_from_data_file(string this_filename)
441 {
442
443
444   line_counter++;
445
446   if (line_counter%50000==0)
447     {
448     cout<<"*"<<flush;
449     }
450
451   coincidence_counts_total++;
452   //read in all lines of data from input file
453
454 //1st photon
455   if (annihilation_pos_yes_or_no==1)
456     {
457     fin>>annihilation1;
458     }
459
460
461   fin>>time1;
462   if (energy_yes_or_no!=0)
463     fin>>energy_1;
464   fin>>x_1;
465   fin>>y_1;
466   fin>>z_1;
467   fin>>blank;
468   fin>>rsector1;
469   fin>>blank;
470   fin>>blank;
471   fin>>crystal1;
472   fin>>blank;
473
474   if (compton_scatter!=0)
475     {
476     fin>>compton_phantom1;
477     fin>>compton_detector1;
```

```
478     }
479
480   if (rotating_gantry!=0)
481     fin>>gantry_angular_position;
482   else
482     gantry_angular_position=0;
483
484
485 //2nd photon
486   if (annihilation_pos_yes_or_no==1)
487     {
488     fin>>annihilation2;
489     }
490
491   fin>>time2;
492   if (energy_yes_or_no!=0)
493     fin>>energy_2;
494   fin>>x_2;
495   fin>>y_2;
496   fin>>z_2;
497   fin>>blank;
498   fin>>rsector2;
499   fin>>blank;
500   fin>>blank;
501   fin>>crystal2;
502   fin>>blank;
503   if (compton_scatter!=0)
504     {
505     fin>>compton_phantom2;
506     fin>>compton_detector2;
507     }
508
509   if (rotating_gantry==1)
510     fin>>blank; //we don't care about this angular position because it will be the same as angular position for photon 1 in the coincidence.
511   //         cout<<endl;
512   //energy distribution histogram
513
514
515
516
```

```
517   if (annihilation_pos_yes_or_no==1)
518   {
519     if (annihilation1 ==7 && annihilation2 ==7)
520       photon_from_background++;
521     else
521       photon_from_source++;
522   }
523 }
524
525
526
527
528
529
530
531
532
533
534
535
536 int calculate_position(int sino_radial,int sino_angles,long int layer_histogram[])
537 {
538
539
540
541
542       if (id_or_coord==1 && multiple_rings_yes_or_no==1)
543         {
544         ring_number1=rsector1%num_rings;
545         ring_number2=rsector2%num_rings;
546
547         if (ring_number1!=ring_number2)
548           {
549           //find out if interactions are from separate rings
550           interRing_coincidence=1;
551           ring_difference = abs(ring_number1-ring_number2);
552           }
553         else
554           {
555           ring_difference=0;
```

```
556           }
557         }
558       else if (id_or_coord==0 && multiple_rings_yes_or_no==1)
559         {
560         ring_number1=1;
561         ring_number2=1;
562         interRing_coincidence=0;
563 
564         ring_difference = abs(int((z_1-z_2)/(crystals_in_z_direction * crystal_size)));
565         }
566       else
566         {
567         ring_number1=0;
568         ring_number2=0;
569         ring_difference = 0;
570         }
571 
572       if (energy_histogram_yes_or_no!=0)
573         {
574         energy_histogram_fn(energy_1, energy_2);
575         }
576 
577       if ((multiple_rings_yes_or_no==1 && ring_difference<=ring_span) || multiple_rings_yes_or_no==0)
578         {
579 
580         if ((energy_yes_or_no!=0 && (energy_1>E_lower && energy_1<E_upper) && (energy_2>E_lower && energy_2<E_upper))|| (energy_yes_or_no==0))
581           {
582 
583           if (compton_phantom1>0 || compton_phantom2>0)
584             compton_phantom_counter++;
585           else
585             real_counter++;
586 
587 //cout<<"actual data  "<<x_1<<"  "<<y_1<<"  "<<z_1<<", "<<z_2<<endl;
588 // cout<<"rebinned layers  "<<rebinned_num_layers<<"  "<<layers_per_sector<<endl;
589 
590 
591 
592           coincidence_counts_inside_window++;
593           if (id_or_coord==1)
```

```
594             {
595             //convert detectorID to x,y,z co-ordinates
596               if (multi_or_single_layer==0)
597               {
598                 //assuming that crystal is a single scintillator block
599
600                 //anglular position of rsector in the ring in radians
601                 rsector_angle1 = ((rsector1/num_rings)-(floor(rsector1/num_rsectors)*num_rsectors))/(num_rsectors) * 3.1415 * 2 + gantry_angular_position/180*3.1415;
602
603
604
605
606                 if (crystals_in_tangential_direction>1)
607                   {
608
609                   //cout<<crystal1<<endl;
610                   tangential_correction1 = -1*(crystals_in_tangential_direction)/2*crystal_size + floor(crystal1%(crystals_in_tangential_direction* layers_per_sector)/layers_per_sector)*crystal_size +
crystal_size/2;
611
612                   radial_distance1 = ring_radius + depth_in_radial_direction/2;
613                   angular_correction1 = atan(tangential_correction1/radial_distance1);
614                   rsector_angle1 = rsector_angle1 + angular_correction1;
615
616                   }
617                 else
617                   radial_distance1 = ring_radius + depth_in_radial_direction/2;
618
619
620
621                 x_1 = radial_distance1 * cos(rsector_angle1);
622                 y_1 = radial_distance1 * sin(rsector_angle1);
623                 z_1 = abs(crystal1/crystals_in_z_direction)* crystal_size - crystals_in_z_direction/2 * crystal_size + crystal_size/2;
624
625                 rsector_angle2 = ((rsector2/num_rings)-(floor(rsector1/num_rsectors)*num_rsectors))/(num_rsectors) * 2 * 3.1415 + gantry_angular_position/180*3.1415;
626
627                 if (crystals_in_tangential_direction>1)
628                   {
629
630                   //cout<<crystal1<<endl;
631                   tangential_correction2 = -1*(crystals_in_tangential_direction)/2*crystal_size + floor(crystal2%(crystals_in_tangential_direction* layers_per_sector)/layers_per_sector)*crystal_size +
```

```
crystal_size/2;
632                   radial_distance2 = ring_radius+ depth_in_radial_direction/2;
633                   angular_correction2 = atan(tangential_correction2/radial_distance2);
634                   rsector_angle2 = rsector_angle2 + angular_correction2;
635
636                   }
637                 else
637                   radial_distance2 = ring_radius+ depth_in_radial_direction/2;
638
639
640
641                 x_2 = radial_distance2 * cos(rsector_angle2);
642                 y_2 = radial_distance2 * sin(rsector_angle2);
643                 z_2 = abs(crystal2/crystals_in_z_direction)* crystal_size - crystals_in_z_direction/2 * crystal_size + crystal_size/2;
644
645                 //it doesn't matter which ring number we send in, they're both the same
646                 calculate_slice(ring_number1, ring_number2, z_1, z_2);
647
648               }
649               else
649               {
650                 //assuming crystal is in multiple layers
651                 //anglular position of rsector in the ring in radians
652
653                 //for the first photon in the coincidence
654                 rsector_angle1 = ((rsector1/num_rings)/(num_rsectors)) * 3.1415 * 2 + gantry_angular_position/180*3.1415;
655 //cout<<rsector1<<"  "<<crystal1<<endl;
656
657                 if (crystals_in_tangential_direction>1)
658                   {
659                   //tangential_correction1 = -1*(crystals_in_tangential_direction)/2*crystal_size + floor(crystal1%(crystals_in_tangential_direction* layers_per_sector)/layers_per_sector)*crystal_size +
crystal_size/2;
660                   tangential_correction1 = -1*(crystals_in_tangential_direction)/2*crystal_size + floor(crystal1%(crystals_in_tangential_direction* layers_per_sector)/layers_per_sector)*crystal_size +
crystal_size/2;
661
662
663 radial_correction1 = (floor( ((crystal1%(layers_per_sector*crystals_in_tangential_direction))%layers_per_sector) / (layers_per_sector/rebinned_num_layers)) + 1/2) *
crystal_size*(layers_per_sector/rebinned_num_layers);
664 //cout<<"crystalID  "<<crystal1<<"  radial correction        "<<radial_correction1<<endl;
665
```

```
666                   radial_distance1 = ring_radius + radial_correction1;
667                   angular_correction1 = atan(tangential_correction1/radial_distance1);
668
669                   rsector_angle1 = rsector_angle1 + angular_correction1;
670                   radial_distance1 = sqrt(pow(radial_distance1,2) + pow(radial_correction1,2));
671
672
673 // cout<<crystal1<<"  "<<tangential_correction1<<"  "<<radial_correction1<<endl;
674                   }
675                 else
675                   {
676                   radial_distance1 = ring_radius + ((crystal1/(layers_per_sector/rebinned_num_layers))%rebinned_num_layers)*(layers_per_sector*crystal_size/rebinned_num_layers) +
(layers_per_sector*crystal_size/rebinned_num_layers)/2;
677
678
679                   }
680 // cout<<"radial_distance1  "<<radial_distance1<<"  angle1  "<<rsector_angle1<<endl<<endl;
681 //
682
683                 layer_histogram[(crystal1)%rebinned_num_layers]++;
684                 //layer_histogram[(crystal1%(crystals_in_z_direction))%rebinned_num_layers]++;
685
686
687                 x_1 = radial_distance1 * cos(rsector_angle1);
688                 y_1 = radial_distance1 * sin(rsector_angle1);
689
690                 if (crystals_in_tangential_direction>1)
691                   {
692                   //z_1 = abs(int(floor(crystal1/(crystals_in_tangential_direction*rebinned_num_layers))) /crystals_in_z_direction ) * crystal_size - crystals_in_z_direction/2 * crystal_size + crystal_size/2;
693                   z_1 = -1*((float(crystals_in_z_direction)-1)/2*crystal_size) + floor(crystal1/(crystals_in_tangential_direction*layers_per_sector))*crystal_size;
694
695                   }
696                 else
696                   {
697                   z_1 = abs(crystal1/crystals_in_z_direction) * crystal_size - crystals_in_z_direction/2 * crystal_size + crystal_size/2;
698                   }
699
700
701
702                 //for the second photon coincidence
```

```
703                 rsector_angle2 = ((rsector2/num_rings)/(num_rsectors)) * 2 * 3.1415 + gantry_angular_position/180*3.1415;
704
705
706                 if (crystals_in_tangential_direction>1)
707                   {
708
709                   //tangential_correction1 = -1*(crystals_in_tangential_direction)/2*crystal_size + floor(crystal1%(crystals_in_tangential_direction* layers_per_sector)/layers_per_sector)*crystal_size +
crystal_size/2;
710                   tangential_correction2 = -1*(crystals_in_tangential_direction)/2*crystal_size + floor(crystal2%(crystals_in_tangential_direction* layers_per_sector)/layers_per_sector)*crystal_size +
crystal_size/2;
711
712
713 radial_correction2 = (floor( ((crystal2%(layers_per_sector*crystals_in_tangential_direction))%layers_per_sector) / (layers_per_sector/rebinned_num_layers)) + 1/2) *
crystal_size*(layers_per_sector/rebinned_num_layers);
714
715                   radial_distance2 = ring_radius + radial_correction2;
716                   angular_correction2 = atan(tangential_correction2/radial_distance2);
717
718                   rsector_angle2 = rsector_angle2 + angular_correction2;
719                   radial_distance2 = sqrt(pow(radial_distance2,2) + pow(radial_correction2,2));
720
721                   }
722                 else
722                   {
723                   radial_distance2 = ring_radius + ((crystal2/(layers_per_sector/rebinned_num_layers))%rebinned_num_layers)*(layers_per_sector*crystal_size/rebinned_num_layers) +
(layers_per_sector*crystal_size/rebinned_num_layers)/2;
724                   }
725
726                 layer_histogram[(crystal2)%rebinned_num_layers]++;
727               //  layer_histogram[(crystal2%(crystals_in_z_direction))%rebinned_num_layers]++;
728
729                 x_2 = radial_distance2 * cos(rsector_angle2);
730                 y_2 = radial_distance2 * sin(rsector_angle2);
731
732
733                 if (crystals_in_tangential_direction>1)
734                   {
735                   //z_1 = abs(int(floor(crystal1/(crystals_in_tangential_direction*rebinned_num_layers))) /crystals_in_z_direction ) * crystal_size - crystals_in_z_direction/2 * crystal_size + crystal_size/2;
736                   z_2 = -1*((float(crystals_in_z_direction)-1)/2*crystal_size) + floor(crystal2/(crystals_in_tangential_direction*layers_per_sector))*crystal_size;
737
```

```
738                 }
739               else
739                 {
740                 z_2 = abs(crystal2/crystals_in_z_direction) * crystal_size - crystals_in_z_direction/2 * crystal_size + crystal_size/2;
741                 }
742
743               slice = calculate_slice(ring_number1, ring_number2, z_1, z_2);
744
745             }
746           }
747         else
747           {
748           slice = calculate_slice(0, 0, z_1, z_2);
749           }
750   //cout<<"**"<<endl;
751
752
753         //calculate radial distance from origin and angle of LOR
754         if (x_2 != x_1)
755         gradient = (y_2-y_1)/(x_2-x_1);
756         //else
757         //gradient = 100000000;
758
759
760         angle = atan(gradient)/3.141592654*180;
761         //if (angle<0)
762         //  angle = 180 + angle;
763
764         y_int = y_1 - x_1*(y_2-y_1)/(x_2-x_1);
765         x_int = (-1*y_int)/gradient;
766
767         //abs() function doesn't seem to work. therefore, square and then square root
768         r=sqrt(pow(y_int*cos(angle/180*3.141592654),2));
769
770         //convert the radial distance into pixels
771         r_pix = r/rad_pix_size;
772
773         //convert angular position value into sinogram pixels
774         angle_pix = angle/angle_pix_size;
775
```

```
776 /*
777 if (x_int<2 && x_int)
778 {
779 cout<<x_1<<"  "<<y_1<<"  "<<x_2<<"  "<<y_2<<endl;
780 cout<<"gradient :"<<gradient<<endl;
781 cout<<"angle :"<<angle<<endl;
782 cout<<x_int<<"  "<<y_int<<"  "<<r<<"  "<<r_pix<<"  "<<angle_pix<<endl;
783
784 //cout<<x_1<<"  "<<y_1<<"  "<<z_1<<"  "<<z_2<<"  "<<average_z<<endl;
785 cout<<"=================="<<endl;
786 }*/
787
788
789
790
791           //finds the middle column and row of the sinogram
792           sino_midpoint = (sino_radial-1)/2;
793
794           //if an angle is slightly larger than 90 or -90, it gets shifted back to the other polarity
795           int angle_pix_rounded;
796           if (angle_pix>sino_midpoint)
797             {
798             angle_pix = -1*float(sino_midpoint);
799             angle_pix_rounded = round(angle_pix,0);
800             y_int = y_int * -1;
801             }
802           else if (angle_pix<-1*sino_midpoint)
803             {
804             angle_pix = float(sino_midpoint);
805             angle_pix_rounded = round(angle_pix,0);
806             y_int = y_int * -1;
807             }
808           else
808             {
809             angle_pix_rounded = round(angle_pix,0);
810             }
811
812
813 //  cout<<"calculated  "<<x_1<<"  "<<y_1<<"  "<<((-1*(num_rings * (crystals_in_z_direction * crystal_size)/2) + (crystals_in_z_direction * crystal_size)/2)+ring_number1*(crystals_in_z_direction *
crystal_size) + z_1)<<"  "<<(-1*(num_rings * (crystals_in_z_direction * crystal_size)/2) + (crystals_in_z_direction * crystal_size)/2)+ring_number2*(crystals_in_z_direction * crystal_size) + z_2<<endl<<endl;
```

```
814
815
816
817
818          //this fudge needed to be made to ensure that the central column of the sinogram wasn't empty. if it wasn't made, the lowest r_pix_rounded would ever be is 1.
819
820
821          y_pos_neg = int(pow(-1,double(sign(y_int))-1));
822
823          bin_sinogram(r_pix,angle_pix);
824          return 1;
825          }
826        }
827
828 return 0;
829 }
830
831
832 int bin_sinogram(float r_pix,float angle_pix)
833 {
834   //---------------------
835   //Sinogram binning stage
836   //This code uses the position of each line of response and its angle to bin it into the sinogram
837   //----------------------
838
839   x_pix_upperLeft= r_pix - 0.5;
840   x_pix_upperRight= r_pix + 0.5;
841   x_pix_lowerLeft= r_pix - 0.5;
842   x_pix_lowerRight= r_pix + 0.5;
843
844   y_pix_upperLeft= angle_pix - 0.5;
845   y_pix_upperRight= angle_pix - 0.5;
846   y_pix_lowerLeft= angle_pix + 0.5;
847   y_pix_lowerRight= angle_pix + 0.5;
848
849   A_pix_upperLeft = (ceil(x_pix_upperLeft)-x_pix_upperLeft)*(ceil(y_pix_upperLeft)-y_pix_upperLeft);
850   A_pix_upperRight = (x_pix_upperRight-floor(x_pix_upperRight))*(ceil(y_pix_upperRight)-y_pix_upperRight);
851   A_pix_lowerLeft = (ceil(x_pix_lowerLeft)-x_pix_lowerLeft)*(y_pix_lowerLeft-floor(y_pix_lowerLeft));
852   A_pix_lowerRight = (x_pix_lowerRight - floor(x_pix_lowerRight))*(y_pix_lowerRight - floor (y_pix_lowerRight));
853
```

```
854
855   sinogram[sino_midpoint+y_pos_neg*int(floor(x_pix_upperLeft))][sino_midpoint+int(floor(y_pix_upperLeft))][slice] =
sinogram[sino_midpoint+y_pos_neg*int(floor(x_pix_upperLeft))][sino_midpoint+int(floor(y_pix_upperLeft))][slice] + A_pix_upperLeft;
856
857   sinogram[sino_midpoint+y_pos_neg*int(floor(x_pix_upperRight))][sino_midpoint+int(floor(y_pix_upperRight))][slice] =
sinogram[sino_midpoint+y_pos_neg*int(floor(x_pix_upperRight))][sino_midpoint+int(floor(y_pix_upperRight))][slice] + A_pix_upperRight;
858
859   sinogram[sino_midpoint+y_pos_neg*int(floor(x_pix_lowerLeft))][sino_midpoint+int(floor(y_pix_lowerLeft))][slice] =
sinogram[sino_midpoint+y_pos_neg*int(floor(x_pix_lowerLeft))][sino_midpoint+int(floor(y_pix_lowerLeft))][slice] + A_pix_lowerLeft;
860
861   sinogram[sino_midpoint+y_pos_neg*int(floor(x_pix_lowerRight))][sino_midpoint+int(floor(y_pix_lowerRight))][slice] =
sinogram[sino_midpoint+y_pos_neg*int(floor(x_pix_lowerRight))][sino_midpoint+int(floor(y_pix_lowerRight))][slice] + A_pix_lowerRight;
862
863
864 return 1;
865 }
866
867
868
869
870
871
872
873
874
875 int calculate_slice(int ring_number1, int ring_number2, float z_1, float z_2)
876 {
877
878   //average_z=((-24+ring_number*24+z_1)+(-24+ring_number*8+z_2))/2;
879   //cout<<z_1<<"  "<<z_2<<endl;
880 //  cout<<ring_number1<<"  "<<ring_number2<<endl;
881 //  cout<<"crystal  "<<crystal1<<"  "<<crystal2<<endl;
882 //  cout<<"calculate z inside the ring"<<z_1<<"  "<<z_2<<endl;
883 //  cout<<-36+ring_number1*24+z_1<<"  "<<-36+ring_number2*24+z_2<<endl<<endl;
884   //cout<<ring_number<<"  "<<average_z<<endl;
885   //slice= int(-1*(num_rings*8)+ (ring_number*24) + average_z);
886 //cout<<average_z<<"  "<<ring_number<<"  "<<slice<<endl;
887
888   if (id_or_coord==1 && multiple_rings_yes_or_no==1)
889     {
```

```
890     average_z=(((-1*(num_rings * (crystals_in_z_direction * crystal_size)/2) + (crystals_in_z_direction * crystal_size)/2)+ring_number1*(crystals_in_z_direction * crystal_size) + z_1)+((-1*(num_rings *
(crystals_in_z_direction * crystal_size)/2) + (crystals_in_z_direction * crystal_size)/2)+ring_number2*(crystals_in_z_direction * crystal_size) + z_2))/2;
891
892
893
894
895     }
896   else
896     {
897     average_z= (z_1 + z_2)/2;
898     }
899
900   slice = int((average_z + (crystal_size/2))/crystal_size)+num_rings*crystals_in_z_direction/2;
901
902 //cout<<"calculated positions: "<<endl;
903 //cout<<x_1<<"    "<<y_1<<"    "<<average_z<<endl<<endl;
904 //cout<<"photon2: "<<x_2<<"    "<<y_2<<"    "<<average_z<<endl;
905 //cout<<"----------------"<<endl;
906
907
908   return slice;
909 }
910
911
912
913
914
915
916
917
918
919
920
921
922
923
924
925
926
927
```

```
928
929
930
931 void write_out_sinogram(int sino_radial, int sino_angles, int axial_samples, long int layer_histogram[])
932 {
933
934         int l;
935
936   string this_output_filename;
937   string this_output_filename_info;
938
939   cout<<"-----------------------------"<<endl;
940   cout<<"Writing Sinogram Output Files"<<endl;
941   cout<<"-----------------------------"<<endl;
942
943   for (int l=1;l<(axial_samples)+1;l++)
944   {
945
946   std::stringstream ss;
947   std::string str;
948   ss << l;
949   ss >> str;
950
951
952   std::stringstream ss2;
953   std::string str2;
954   ss2 << rebinned_num_layers;
955   if (multi_or_single_layer==0)
956     ss2 << 1;
957   ss2 >> str2;
958
959
960   std::stringstream ss3;
961   std::string str3;
962   ss3 << E_lower;
963   ss3 >> str3;
964
965   std::stringstream ss4;
966   std::string str4;
967   ss4 << E_upper;
```

```
968   ss4 >> str4;
969
970   std::stringstream ss5;
971   std::string str5;
972   ss5 << crystal_size;
973   ss5 >> str5;
974
975   if (id_or_coord==1)
976     {
977     if (energy_yes_or_no==1)
978       {
979       if (multi_or_single_layer==0)
980         {
981         this_output_filename= "sino_" + str5 + "x" +str5 + "x" + str5 + "crystals_1radiallayers_axialslice" + str + "_energywindow" + str3 + "-" + str4 + ".dat";
982         this_output_filename_info= "sino_" + str5 + "x" +str5 + "x" + str5 + "crystals_1radiallayers_energywindow" + str3 + "-" + str4 + ".info";
983         }
984       else
984         this_output_filename= "sino_" + str5 + "x" +str5 + "x" + str5 + "crystals_"+ str2 + "radiallayers_axialslice" + str + "_energywindow" + str3 + "-" + str4 + ".dat";
985         this_output_filename_info= "sino_" + str5 + "x" +str5 + "x" + str5 + "crystals_"+ str2 + "radiallayers_energywindow" + str3 + "-" + str4 + ".info";
986       }
987     else
987       {
988       this_output_filename= "sino_" + str5 + "x" +str5 + "x" + str5 + "crystals_"+ str2 + "radiallayers_axialslice" + str + "_default_energy_window.dat";
989       this_output_filename_info= "sino_" + str5 + "x" +str5 + "x" + str5 + "crystals_"+ str2 + "radiallayers_default_energy_window.info";
990       }
991     }
992
993   else
993     {
994     this_output_filename= "sino_" + str5 + "x" +str5 + "x" + str5 + "crystals_XYZ_axialslice" + str + "_energywindow" + str3 + "-" + str4 + ".dat";
995     this_output_filename_info= "sino_" + str5 + "x" +str5 + "x" + str5 + "crystals_XYZ_energywindow" + str3 + "-" + str4 + ".info";
996     }
997
998   cout<<this_output_filename<<endl;
999
1000
1001   //write sinogram data to output file
1002   ofstream fout;
1003   fout.open(this_output_filename.c_str(),ios::out);
1004
```

```
for (int k=0;k<sino_angles;k++)
    {
  for (int n=0;n<sino_radial;n++)
  {
      fout<<setprecision(3)<<fixed<<float(sinogram[n][k][l])<<" \t";
  }
  fout<<endl;
    }
fout.close();
}


ofstream fout_info;
fout_info.open(this_output_filename_info.c_str(),ios::out);
fout_info<<"Ring Radius = "<<ring_radius<<endl;

fout_info<<"Data source = "<<data_filename<<endl;
fout_info<<"Number of files = "<<num_data_files<<endl;
fout_info<<"Total number of coincidences recorded = "<<coincidence_counts_total<<endl;
fout_info<<"Number of coincidences within Energy Window = "<<coincidence_counts_inside_window<<endl;

fout_info<<"Upsampling factor ="<<upsampling_factor<<endl;
fout_info<<"Sino Radial = "<<sino_radial<<endl;
fout_info<<"Sino Angles = "<<sino_angles<<endl;
fout_info<<"Reconstructed from volume ID or XYZ co-ordinates = ";
if (id_or_coord==1)
  {
  fout_info<<"volume_ID"<<endl;
  if (multi_or_single_layer==1)
    {
    fout_info<<"Multiple Layers of crystal = Yes"<<endl;
    fout_info<<"Number of layers considered = "<<rebinned_num_layers<<endl;
    }
  else
    {
    fout_info<<"Multiple Layers of crystal = No"<<endl;
    }

  }
else
```

```
1043     fout_info<<"XYZ coordinates"<<endl;
1044
1045   fout_info<<"Energy Window = ";
1046   if (energy_yes_or_no==1)
1047     {
1048     fout_info<<E_lower*1000<<" - "<<E_upper*1000<<" keV"<<endl;
1049     }
1050   else
1050     {
1051     fout_info<<"350 - 650 keV"<<endl;
1052     }
1053
1054
1055
1056
1057   cout<<"-----------------------------"<<endl<<endl;
1058   cout<< "There were "<< coincidence_counts_inside_window << " coincidences inside the coincidence window from a total of "<< coincidence_counts_total <<" coincidences"<<endl<<endl;
1059   cout<<"-----------------------------"<<endl<<endl;
1060
1061
1062   if (id_or_coord==1)
1063     {
1064
1065     cout<<"Layer interaction distribution"<<endl<<endl;
1066     for (int k=0; k<rebinned_num_layers;k++)
1067       {
1068       cout<<"Layer "<<k<<": "<<layer_histogram[k]<<endl;
1069       }
1070     cout<<endl<<endl;
1071     }
1072
1073
1074   if (energy_histogram_yes_or_no!=0)
1075     {
1076     //write energy histogram file
1077     string this_energy_histo_filename;
1078     std::stringstream ss6;
1079     std::string str6;
1080     ss6 << E_lower;
1081     ss6 >> str6;
```

```
1082
1083     std::stringstream ss7;
1084     std::string str7;
1085     ss7 << E_upper;
1086     ss7 >> str7;
1087
1088     std::stringstream ss8;
1089     std::string str8;
1090     ss8 << rebinned_num_layers;
1091     if (multi_or_single_layer==0)
1092       ss8 << 1;
1093     ss8 >> str8;
1094
1095     if (id_or_coord==1)
1096       {
1097       this_energy_histo_filename = "energy_histogram_" + this_output_filename.substr(5,14)+ str8 + "radiallayers_energywindow" + str6 + "-" + str7 + ".dat";
1098       }
1099     else
1099       {
1100       this_energy_histo_filename = "energy_histogram_" + this_output_filename.substr(5,14)+ "XYZ_energywindow" + str6 + "-" + str7 + ".dat";
1101       }
1102
1103     if (energy_histogram_yes_or_no!=0)
1104       {
1105
1106       ofstream fout;
1107       fout.open(this_energy_histo_filename.c_str(),ios::out);
1108       fout<<"Energy (keV)  Counts"<<endl;
1109         for (int k=0;k<num_energy_bins;k++)
1110           {
1111           fout<<setprecision(5)<<(k*E_histo_step)*1000<<"  "<<energy_histogram[k]<<endl;
1112           }
1113       fout.close();
1114
1115       cout<<endl<<"Energy histogram written into "<<this_energy_histo_filename<<endl<<endl;
1116       }
1117     }
1118
1119
1120 cout<<"Percentage of unscattered photons from phantom: "<<real_counter/(compton_phantom_counter+real_counter)*100<<"%"<<endl<<endl<<endl;
```

```
1121
1122 cout<<"Photons from source: "<<photon_from_source<<"  Photons from background: "<<photon_from_background<<endl;
1123 cout<<"Percentage of photons from source vs photons from background: "<<(photon_from_source/(photon_from_source+photon_from_background))*100<<"%"<<endl<<endl;
1124
1125 }
1126
1127
1128
1129 void energy_histogram_fn(float energy_1, float energy_2)
1130 {
1131 if (energy_1>0.49 && energy_1<0.53)
1132   {
1133   //cout<<energy_1<<"      "<<round((energy_1)/E_histo_step, 1)<<endl;
1134   q++;
1135   }
1136
1137 energy_histogram[round((energy_1)/E_histo_step, 1)]++;
1138 energy_histogram[round((energy_2)/E_histo_step, 1)]++;
1139 //cout<<energy_1<<"       "<<E_histo_step<<"       "<<round((energy_1/E_histo_step), 1)<<endl;
1140
1141
1142
1143
1144 }
1145
1146
1147
1148
1149
1150
1151
1152
1153
1154
1155
1156
1157
1158
1159
1160
```

```

int round(const float &number, const int num_digits)
{
    float doComplete5i, doComplete5(number * powf(10.0f, (float) (num_digits + 1)));

    if(number < 0.0f)
        doComplete5 -= 5.0f;
    else
        doComplete5 += 5.0f;

    doComplete5 /= 10.0f;
    modff(doComplete5, &doComplete5i);

    return int(doComplete5i / powf(10.0f, (float) num_digits));
}

int grad_pos_neg(float gradient)
{
  if (gradient>0)
    return 1;
  else
    return (-1);
}


int yint_pos_neg(float y_int)
{
  if (y_int>0)
    return 1;
  else
    return (-1);
}



bool sign(float n)
{
return n >= 0;
}

```

1200

# APPENDIX B
# IMAGE RECONSTRUCTION INSTRUCTIONS

## B.1 Introduction

The output of the sinogram binning application is a large text file with X rows and Y columns where X represents the number of radial bins in the sinogram and Y represents the number of angular bins. Each value is stored as a 32 bit value. The Radon Transform plug-in [53] shown in Figure B.1 requires an 8-bit sinogram in TIFF format to reconstruct. The following process is utilised to view and edit a sinogram into a format suitable for reconstruction.

### B.1.1 Opening a Sinogram

As the sinogram is not in an image format, it is necessary to import it as a "text image".

`File` → `Import` → `Text Image`

Find the sinogram that must be reconstructed and open it. Once this image is

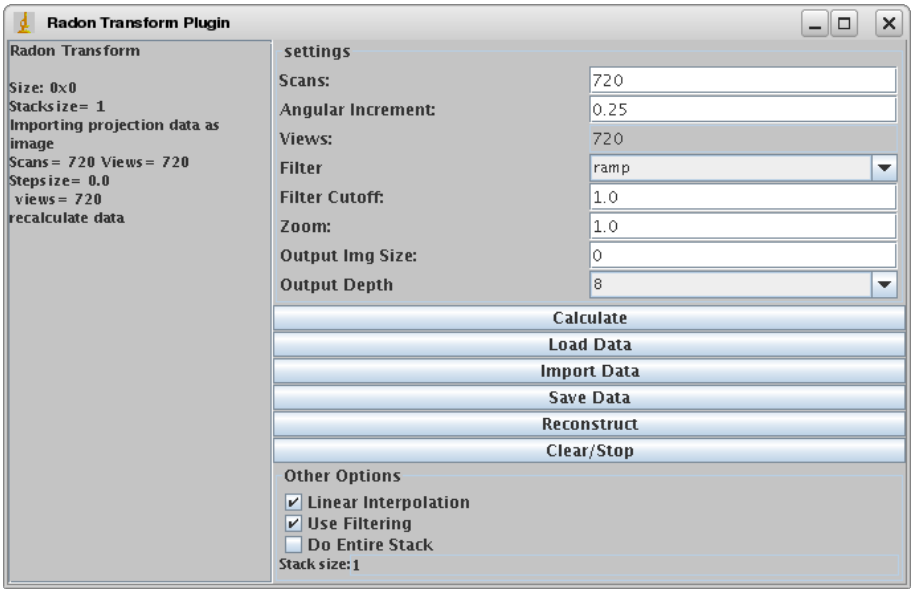


Figure B.1: The Radon Transform Plugin

open, it will look similar to Figure B.2.

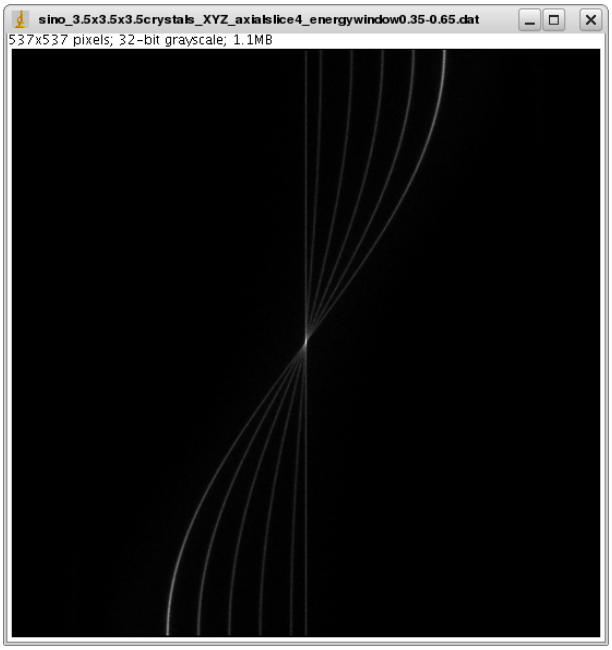


Figure B.2: ImageJ displaying a sinogram

### B.1.2 Downsampling to 8-bit

The sinogram must be converted into an 8-bit image meaning pixel values must be reduced down from 32-bit values, a lossy process.

`Image` → `Type` → `8-bit`

This new 8-bit image must be saved as a TIFF in order for the Radon Transform plugin to be able to process it.

`File` → `Save As` → `Tiff`

### B.1.3 Image Transformation

The sinogram used by the Radon Transform plugin requires the x-axis to contain angular data and the y-axis to be radial distance data, the opposite of the output of the sinogram binning application. Furthermore, the angular data is not from -90$^o$ to +90$^o$. The transformation shown in Figure B.3 must be made using an image editing package such as The Gimp [61].

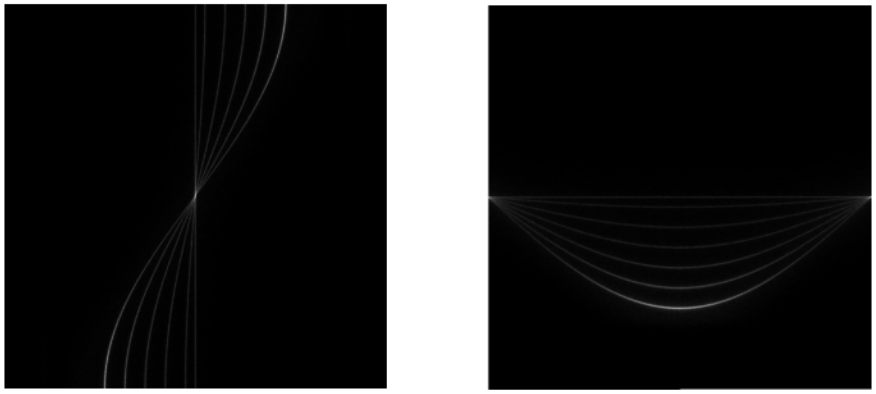

Figure B.3: The starting sinogram and following the transformation

The top half of the original sinogram is selected and pasted as a new layer and flipped horizontally. The bottom half of the image is moved to the top and the pasted original top half aligned with the original bottom half. The combined image is then rotated anti-clockwise 90$^o$. The Radon Transform requires the image size

to either 90, 180, 360, 720, 1440 pixels along both edges. Resize the image to the nearest of these values.

### B.1.4 Image Reconstruction

Using ImageJ, the Radon Transform Plugin can be used to reconstruct the data stored in the sinogram.

`Plugins` → `Radon Transform`

Import the sinogram data into the Radon Transform Plugin by selecting `Import Data` in the Radon Transform interface. Import the data as "columns".

The "Scans" value is equal to the dimensions of the sinogram and the angular increment must be selected to make the number views equal to "Scans" and can be determined by:

$$angular\ increment = \frac{180}{Scans}$$

The other parameters can be selected by the user, however the following parameters were used in this study:

- Filter: ramp
- Filter Cutoff: 1.0
- Zoom: 1
- Output Img Size: the same as the sinogram size
- Output Depth: 8

Finally, select `Reconstruct` and the image will be reconstructed based on the selected parameters. This image can then be saved in ImageJ as a TIFF image for further analysis.

## REFERENCES

[1] Jens Langner. Development of a Parallel Computing Optimized Head Movement Correction Model in Positron Emission Tomography. Master's thesis.

[2] http://physics.nist.gov.

[3] H. Liu, T. Omura, M. Watanabe, and T. Yamashita. Development of a Depth of Interaction Detector for Gamma-Rays. page 182, 2001.

[4] J. S. Huber, W. W. Moses, M. S. Andreaco, and O. Petterson. An LSO Scintillator Array for a PET Detector Module with Depth of Interaction Measurement. *IEEE Trans. Nuc. Sci.*, 48:684, 2001.

[5] H. Murayama, H. Ishibashi, H. Uchida, T. Omura, and T. Yamashita. Depth Encoding Multicrystal Detectors for PET. *IEEE Trans. Nuc. Sci.*, 45:1152, 1998.

[6] T. Tsuda, H. Murayama, K. Kitamura, N. Inadama, T. Yamaya, E. Yoshida,

F. Nishikido, M. Hamamoto, H. Kawai, and Y. Ono. Performance evaluation of a subset of a four-layer LSO detector for a small animal DOI PET scanner: jPET-RD. *Nuclear Science, IEEE Transactions on*, 53(1):35–39, Feb. 2006.

[7] Frederic H. Fahey. Data Acquistions in PET Imaging. *JNM*, 2002.

[8] Mustafa E. Kamasak. EXACT HR+ Scanner Information. Technical report, Purdue University, 2005.

[9] http://www.owlnet.rice.edu/ elec431/projects96/DSP/filters.html.

[10] Mark T. Madsen. Recent Advances in SPECT imaging. *Journal of Nuclear Medicine*, 48(4):661–673, 2007.

[11] *GATE Users Guide*.

[12] M.M. Ter-Pogossian, M.E. Phelps, E.J. Hoffman, and N.A. Mullani. Positron-emission transaxial tomograph for nuclear imaging (PETT). *Radiology*, 114(1):89–98, 1975.

[13] Phelps ME, Hoffman EJ, Mullani NA, and Ter-Pogossian MM. Application of annihilation coincidence detection to transaxial reconstruction tomography. *JNM*, 16(3):210–224, 1975.

[14] M. Partridge, A. Spinelli, W. Ryder, and C. Hindorf. The effect of b+ energy on performance of a small animal PET camera. *Nuclear Instruments and Methods in Physics Research A*, 568:933–936, 2006.

[15] M. Dahlbom, L.R. MacDonals, L. Eriksson, M. Paulus, M. Andreaco, M.E. Casey, and C. Moyers. Performance of a YSO/LSO Phoswitch Detector for use in a PET/SPECT System. *IEEE Trans. Nuc. Sci.*, 44:1114, 1998.

[16] University of Central Florida and Crystal Photonics, September 2003. US

patent 6 624 420.

[17] R.A. Yotter and D.M. Wilson. A review of photodetectors for sensing light-emitting reporters in biological systems. *Sensors Journal, IEEE*, 3(3):288–303, June 2003.

[18] 3D PET using a conventional multislice tomograph without septa. *J Comput Assist Tomogr*.

[19] D.C. Kocher. Radioactive decay data tables, Report DOE/TIC-11026. Technical report, US DoE, 1981.

[20] R.R. Raylman, B.E. Hammer, and N.L. Christensen. Combined MRI-PET scanner: a Monte Carlo evaluation of the improvements in PET resolution due to the effects of a static homogeneous magnetic field. *Nuclear Science, IEEE Transactions on*, 43(4):2406–2412, Aug 1996.

[21] Craig S Levin and Edward J Hoffman. Calculation of positron range and its effect on the fundamental limit of positron emission tomography system spatial resolution. *Physics in Medicine and Biology*, 44(3):781–799, 1999.

[22] Arion F. Chatziioannou. Molecular imaging of small animals with dedicated PET tomographs. *European Journal of Nuclear Medicine*, 29:98–114, 2002.

[23] Michael E. Phelps. *PET:Physics, Instrumentation and Scanners*. Springer, illustrated edition, 2006.

[24] S.C. Huang et al M.E. Phelps, E.J. Hoffman. A New Computerized Tomographic Imaging System for Positron-Emitting Radiopharmaceuticals. *J. Nuc. Med*, 19:635, 1978.

[25] J.T. Hood .S. Higgins D.C. Ficke M. Ter-Poggossian, N.A. Mullani. Design Considerations for a Positron Emission Tomograph (PETT-V) for Imaging of

Brain. *J. Comput. Assist. Tomogr.*, 2:539, 1978.

[26] G. DiChiro W.S. Friauf S.B. Leighton R.A. Brooks, U.J. Sank. Design of High Resolution Positron Emission Tomograph: The neuro-PET. *J. Comput. Assist. Tomogr.*, 4:5, 1980.

[27] M.E. Casey and R. Nutt. A Multicrystal Two Dimensional BGO Detector System. *IEEE Trans. Nuc. Sci.*, page 460, 1986.

[28] H.O Anger. Scintillation camera. *Rev. Sci. Instr.*, 29:619–629, 1958.

[29] S.R. Cherry, Y. Shao, M.P. Tornai, S. Siegel, A.R. Ricci, and M.E. Phelps. Collection of Scintillation Light from Small BGO Crystals. *IEEE Trans. Nuc. Sci.*, 42(3):1058, 1995.

[30] J. Seidel, J. Vaquero, S. Siegel, W. R. Gandler, and M. V. Green. Depth Identication Accuracy of a Three-Layer Phoswich PET Detector Module. *IEEE Trans. Nuc. Sci.*, 46:485, 1999.

[31] U. Heinrichs, U. Pietrzyk, and K. Ziomons. Design Optimization of the PMT-ClearPET Prototypes Based on Simulation Studes with GEANT3. *IEEE Trans. Nuc. Sci.*, 50:1428, 2003.

[32] N. Zhang, C. J. Thompson, D. Togane, F. Cayouette, K. Q. Nguyen, and M. L. Camborde. Anode Position and Last Dynode Timing Circuits for Dual-Layer BGO Scintillator with PS-PMT Based Modular PET Detectors. *IEEE Trans. Nuc. Sci.*, 49:2203, 2002.

[33] W. W. Moses and S. E. Derenzo. Design Studies for a PET Detector Module using a PIN Photodiode to Measure Depth of Interaction. *IEEE Trans. Nuc. Sci.*, 41:1441, 1994.

[34] M. Watanabe, T. Omura, H. Kyushima, Y. Hasegawa, and T. Yamashita. A

compact position-sensitive detector for PET. *Nuclear Science, IEEE Transactions on*, 42(4):1090–1094, Aug 1995.

[35] S. Nagai, M. Watanabe, H. Shimoi, H. Liu, and Y. Yoshizawa. A new compact position-sensitive PMT for scintillation detectors. *Nuclear Science, IEEE Transactions on*, 46(3):354–358, Jun 1999.

[36] S. Agostinelli, J. Allison, K. Amako, J. Apostolakis, H. Araujo, P. Arce, M. Asai, D. Axen, S. Banerjee, G. Barrand, F. Behner, L. Bellagamba, J. Boudreau, L. Broglia, A. Brunengo, H. Burkhardt, S. Chauvie, J. Chuma, R. Chytracek, G. Cooperman, G. Cosmo, P. Degtyarenko, A. Dell'Acqua, G. Depaola, D. Dietrich, R. Enami, A. Feliciello, C. Ferguson, H. Fesefeldt, G. Folger, F. Foppiano, A. Forti, S. Garelli, S. Giani, R. Giannitrapani, D. Gibin, J. J. Gomez Cadenas, I. Gonzalez, G. Gracia Abril, G. Greeniaus, W. Greiner, V. Grichine, A. Grossheim, S. Guatelli, P. Gumplinger, R. Hamatsu, K. Hashimoto, H. Hasui, A. Heikkinen, A. Howard, V. Ivanchenko, A. Johnson, F. W. Jones, J. Kallenbach, N. Kanaya, M. Kawabata, Y. Kawabata, M. Kawaguti, S. Kelner, P. Kent, A. Kimura, T. Kodama, R. Kokoulin, M. Kossov, H. Kurashige, E. Lamanna, T. Lampen, V. Lara, V. Lefebure, F. Lei, M. Liendl, W. Lockman, F. Longo, S. Magni, M. Maire, E. Medernach, K. Minamimoto, P. Mora de Freitas, Y. Morita, K. Murakami, M. Nagamatu, R. Nartallo, P. Nieminen, T. Nishimura, K. Ohtsubo, M. Okamura, S. O'Neale, Y. Oohata, K. Paech, J. Perl, A. Pfeiffer, M. G. Pia, F. Ranjard, A. Rybin, S. Sadilov, E. Di Salvo, G. Santin, T. Sasaki, N. Savvas, Y. Sawada, S. Scherer, S. Sei, V. Sirotenko, D. Smith, N. Starkov, H. Stoecker, J. Sulkimo, M. Takahata, S. Tanaka, E. Tcherniaev, E. Safai Tehrani, M. Tropeano, P. Truscott, H. Uno, L. Urban, P. Urban, M. Verderi, A. Walkden, W. Wander, H. Weber, J. P. Wellisch, T. Wenaus, D. C. Williams, D. Wright, T. Yamada, H. Yoshida, and D. Zschiesche. Geant4-a simulation toolkit. *Nucl Instrum Meth A*, 506(3):250, 2003.

[37] A. J. Reader, S. Ally, F. Bakatselosm, R. Manavaki, R. J. Walledge, A. P. Jeavons, P. J. Julyan, S. Zhao, D. L. Hastings, , and J. Zweit. One-pass list-mode EM algorithm for high resolution 3-D PET image reconstruction into large arrays. *IEEETNS*, 49:69399, June 2002.

[38] J. Walledge, A. J. Reader, E. O. Aboagye, T. J. Spinks, M. Honer, J. Missimer, and A. P. Jeavons. "4-D PET with the quad-HIDAC: Development of dynamic list-mode image reconstruction". In *Proc. IEEE NSS-MIC*, page 17161720, 2002.

[39] M.E. Daube-Witherspoon and Gerd Muehllehner. Treatment of Axial Data in Three Dimensional PET. *JNM*, 28:1717–1724, 1987.

[40] K Erlandsson, P D Esserz, S-E Strandt, and R L van Heertun. 3D reconstruction for a multi-ring PET scanner by single-slice rebinning and axial deconvolution. *PMB*, 39:619–629, 1994.

[41] H.M. Hudson and R.S. Larkin. Accelerated image reconstruction using ordered subsets of projection data. *Medical Imaging, IEEE Transactions on*, 13(4):601–609, Dec 1994.

[42] http://www.ittvis.com/idl/.

[43] Jan Chan Steve Meikle. OSEM Reconstruction Algorithm, Personal Correspondence.

[44] Daube-Witherspoon ME, Karp JS, Casey ME, DiFilippo FP, Hines H, Muehllehner G, Simcic V, Stearns CW, Adam LE, Kohlmyer S, and Sossi V. PET performance measurements using the NEMA NU 2-2001 standard. *JNM*, 43(10):1398–1409, Oct. 2002.

[45] Brian F Hutton. An Introduction to Iterative Reconstruction. *Alasbimn Journal*, 5(AJ18-6):661–673, 2002.

[46] T. Kimble, M. Chou, and B.H.T. Chai. Scintillation properties of LYSO crystals. *Nuclear Science Symposium Conference Record, 2002 IEEE*, 3:1434–1437 vol.3, 10-16 Nov. 2002.

[47] M. Safavi-Naeini, M.L.F. Lerch, M. Petasecca, G.U. Pignatel, M. Reinhard, and A.B. Rosenfeld. Evaluation of pixellated, back-sided planar photodetectors for high-resolution imaging instrumentation. *Nuclear Instruments and Methods in Physics Research Section A: Accelerators, Spectrometers, Detectors and Associated Equipment*, 589(2):Pages 259–267, 1 May 2008.

[48] http://depts.washington.edu/simset/html/news/newsindex.html.

[49] http://www.irs.inms.nrc.ca/papers/historyandoverviewofEGS4.pdf.

[50] http://mcnp-green.lanl.gov/publication/pdf/LA-UR-02-3935.pdf.

[51] P.R.G. Virador, W.W. Moses, and R.H. Huesman. Reconstruction in PET cameras with irregular sampling and depth of interaction capability. *Nuclear Science, IEEE Transactions on*, 45(3):1225–1230, Jun 1998.

[52] A. Dagher and C. J. Thompson. Real-Time Data Rebinning in PET to Obtain Uniformly Sampled Projections. *Nuclear Science, IEEE Transactions on*, 32(1):811–817, Feb. 1985.

[53] http://rsbweb.nih.gov/ij/plugins/radon-transform.html.

[54] availabe online http://rsb.info.nih.gov/ij/.

[55] Yuan-Chuan Tai, Ananya Ruangma, Douglas Rowland, and Stefan Siegel et al.

Performance Evaluation of the microPET Focus: A Third-Generation microPET Scanner Dedicated to Animal Imaging. *The Journal of Nuclear Medicine*, 2005.

[56] S. Derenzo. *Positron Annihilation*, chapter Precision measurement of annihilation point spread distributions for medically important positron emitters, page 819823. The Japanese Institute of Metals, 1979.

[57] I. Buvat, H. Benali, A. Todd-Pokropek, and R. Di Paola. Scatter correction in scintigraphy: the state of the art. *European Journal of Nuclear Medicine and Molecular Imaging*, 21(7):675–694, 1994.

[58] M.L.F. Lerch, R. Ward, P.E. Simmonds, V.L. Pervertailo, S.R. Meikle, G.N. Taylor, and A.B. Rosenfeld. Readout of LYSO using a new silicon photodetector for positron emission tomography. *Nuclear Science Symposium Conference Record, 2003 IEEE*, 2:1408–1412 Vol.2, Oct. 2003.

[59] http://amide.sourceforge.net/.

[60] R M Lewitt, G Muehllehner, and J S Karp. Three-dimensional image reconstruction for PET by multi-slice rebinning and axial image filtering. *Physics in Medicine and Biology*, 39(3):321–339, 1994.

[61] http://www.gimp.org/.